Title

Modeling and Design of Radio Frequency Magnetic Devices Based on Equivalent Circuit Representation of Spin Dynamics

Author

Gao, Qian

Publication Date

2024

Peer reviewed|Thesis/dissertation

UNIVERSITY OF CALIFORNIA
Los Angeles

Modeling and Design of Radio Frequency Magnetic Devices Based on Equivalent Circuit Representation of Spin Dynamics

A dissertation submitted in partial satisfaction
of the requirements for the degree
Doctor of Philosophy in Electrical and Computer Engineering

by

Qian Gao

2024

ABSTRACT OF THE DISSERTATION

Modeling and Design of Radio Frequency Magnetic Devices
Based on Equivalent Circuit Representation of Spin Dynamics

by

Qian Gao
Doctor of Philosophy in Electrical and Computer Engineering
University of California, Los Angeles, 2024
Professor Yuanxun Wang, Chair

Magnetic materials offer a unique combination of properties such as non-reciprocity, high permeability, broad tunability, strong frequency dispersion, and nonlinearity. These characteristics made them uniquely valuable in various linear RF devices such as inductors, circulators, isolators, phase shifters, filters, and antennas. Nonlinear RF magnetic devices such as frequency selective limiters and signal-to-noise enhancers have also received significant attention lately. Leveraging on the recent advances in the fabrication of thin film and thick film magnetic materials, many traditional RF magnetic devices can now be integrated on-chip, which opens up ways to supply high-quality factor passives on-chip that are lacking in existing semiconductor-based integrated circuit (IC) process. This dissertation delves into the modeling and design of RF magnetic devices through equivalent circuit models derived from micromagnetic theory. These models provide concise and intuitive representations of the linear and nonlinear spin dynamics and spin wave propagations within RF magnetic materials.

The research demonstrates the efficacy of these equivalent circuit models by apply-

ing them to various RF devices, including ferrite-loaded strip lines, small antennas, and frequency-selective limiters (FSLs). These models have shown high accuracy in predicting device performance, aligning well with full-wave simulations and empirical data. A significant focus is placed on millimeter-wave resonators and filters using M-type barium hexagonal ferrite, with operational frequencies reaching up to 45 GHz. These devices are optimized for better energy coupling and exhibit promising potential for millimeter-wave applications. This dissertation significantly advances the understanding and application of RF magnetic devices, laying a robust foundation for future innovations.

The dissertation of Qian Gao is approved.

Aydin Babakhani

Robert N. Candler

Gregory P. Carman

Yuanxun Wang, Committee Chair

University of California, Los Angeles

2024

This dissertation is dedicated to my family for their love and support

TABLE OF CONTENTS

LIST OF FIGURES

LIST OF TABLES

VITA

2021–2024 Ph.D. candidate in Electrical and Computer Engineering,
University of California Los Angeles (UCLA), Los Angeles, U.S.A

2019–2021 M.S. in Electrical and Computer Engineering,
University of California Los Angeles (UCLA), Los Angeles, U.S.A

2015–2019 B.Eng. in Microelectronic Science and Engineering,
Nanjing University, Nanjing, China

PUBLICATIONS

The work presented in this dissertation is based on the following publications and conference presentations:

1. Q. Gao, M. E. Fordham, H. Cui and Y. E. Wang, "A Compact Circuit Model for Frequency-Selective Limiters With Strong Field Nonuniformity," in IEEE Transactions on Microwave Theory and Techniques, vol. 71, no. 12, pp. 5124-5134, Dec. 2023, doi: 10.1109/TMTT.2023.3285449.

2. Q. Gao, M. E. Fordham, W. Gu, H. Cui and Y. E. Wang, "Design RF Magnetic Devices With Linear and Nonlinear Equivalent Circuit Models: Demystify RF Magnetics With Equivalent Circuit Models," IEEE Microwave Magazine, vol. 23, no. 11, pp. 28-47, Nov. 2022, doi: 10.1109/MMM.2022.3196414.

3. Q. Gao and Y. E. Wang, "A Compact Circuit Model for Frequency-Selective Limiters with Strong Field Nonuniformity," 2023 IEEE Radio and Wireless Symposium (RWS), Las Vegas, NV, USA, 2023. pp. 73-75, doi: 10.1109/RWS55624.2023.10046293.

4. Qian Gao, Lap Yeung, Yuanxun Ethan Wang. "Miniaturized Millimeter Wave Resonators

with Self-Biased BaM Films", IEEE International Symposium on Antennas and Propagation and USNC-URSI Radio Science Meeting (AP-S/URSI), July 23–28, 2023, Portland, Oregon, USA.

5. Shih-Ming Huang, Qian Gao, Yuanxun Ethan Wang. "A Ferromagnetic-Resonance Based Electrically Small Antenna with Circular Polarization", IEEE International Symposium on Antennas and Propagation and USNC-URSI Radio Science Meeting (AP-S/URSI), July 23–28, 2023, Portland, Oregon, USA.

6. Qian Gao, Yuanxun Ethan Wang. "A Compact Circuit Model for Frequency Selective Limiters (FSLs) with Field Nonuniformities", 2022 TANMS Advanced Research Strategy Meeting (ARSM), Los Angeles, CA, USA, Feb. 15-17, 2022.

CHAPTER 1

Introduction

1.1 Background and Motivation

The significance of magnetic materials has been recognized by ancient civilizations for numerous centuries. By the 12th century, the Chinese already used lodestone, also known as magnetite (Fe_3O_4), in compasses for navigation. However, it wasn't until the 1930s that contemporary ferrites were thoroughly investigated for their magnetic, structural, and electronic properties [1]. Following that, the advancement in magnetic materials has been remarkable, with each new development quickly overtaking the previous.

Unlike most substances, ferrite materials are insulating magnetic oxides that exhibit both high permeability and moderate permittivity across a wide frequency range, from DC to millimeter waves. Their low eddy current losses render them unparalleled in electronic applications, particularly in power generation, conditioning, and conversion. These characteristics also make them uniquely valuable in microwave devices by virtue of their non-reciprocity, high permeability, broad tunability, strong frequency dispersion, and nonlinearity [2],[66] [67]. In contrast to dielectric material, where the permittivity constant is a scalar, the permeability of RF magnetic material is usually a tensor in its linear regime, expressed as an asymmetrical matrix. Yet, each entry in the matrix varies as a function of frequency and biasing field. At high RF power, the magnetic material can be easily driven into a nonlinear regime that exhibits increased dissipation, drifting of resonant frequency generation of harmonics, etc. At the microscale, electromagnetic waves in the magnetic material are often

coupled with spin waves supported by exchange coupling in quantum mechanics. This brings researchers' interests to both the modeling and application of the material.

1.1.1 RF Magnetic Devices

Due to the unique properties brought by magnetic materials, they have been employed for various linear RF devices such as inductors [3], circulators [4]-[7], isolators [8], phase shifters [24], filters [9]-[13],[70], and antennas [14]-[17],[69]. Nonlinear RF magnetic devices such as frequency selective limiters and signal-to-noise enhancers have also received significant attention lately [18]-[26]. Leveraging on the recent advances in the fabrication of thin film and thick film magnetic materials, many traditional RF magnetic devices can now be integrated on-chip, which opens up ways to supply high-quality factor passives on-chip that are lacking in existing semiconductor-based integrated circuit (IC) process [27].

1.1.1.1 Antennas

Ferrites can be loaded to small dipoles (small loops) to optimize the electrically-small antenna (ESA) design. In the early 1970s, leading antenna engineers such as Rumsey [28] and DeVore [29] began exploring electronically scanned arrays in the context of ferrite rod antennas. They independently derived formulas for the radiation efficiencies of electrically small, ferrite-loaded loop antennas using field analysis and circuit modeling, respectively. Their findings suggested that using low-loss ferrites with a small-loss tangent could lead to high efficiency in ESAs. However, the lack of suitable ferrites for radio frequencies (RF) at that time reduced interest in ferrite rod ESAs. More recently, it has been shown in studies [30] and [31] that ferrites, even those with a high loss tangent, can still achieve high radiation efficiency in ESAs. This efficiency results from the high permeability of the material, whether complex or real, which prevents energy from penetrating the interior of the antenna and thus lowers its radiation quality factor (Q). Currently, most ESAs that use permeable

materials are constructed from bulky, unbiased ferrites [31]-[34], which maintain roughly constant permeability across frequencies but typically have single-digit relative permeability at RF. Meanwhile, biased ferrites, known for their strong ferromagnetic resonance (FMR), have been widely used in RF circulators, isolators, filters, and tunable matching circuits. In some recent works [35]-[37], these biased ferrites have been employed in radiators, where the FMR of ferrite slabs or films is used to precisely adjust the matching frequencies of structurally resonant antennas like slots loops, and patches.

Specifically, the work referenced in [73] introduced an ESA design to achieve high radiation efficiency using a miniaturized and conformal antenna platform equipped with ferrite-thin films. When oriented perpendicularly, these films are biased in-plane to enhance the strong ferromagnetic resonance (FMR) behavior. Ferrite thin films differ from their bulk counterparts by offering high in-plane permeability and elevated FMR frequencies due to out-of-plane demagnetization effects, making them ideal for ESAs operating at radio frequencies (RF). Low-loss thin film magnetic materials such as Yttrium Iron Garnet (YIG) and Iron Gallium Boron (FeGaB) have demonstrated in-plane relative permeabilities ranging from several hundred to a thousand.

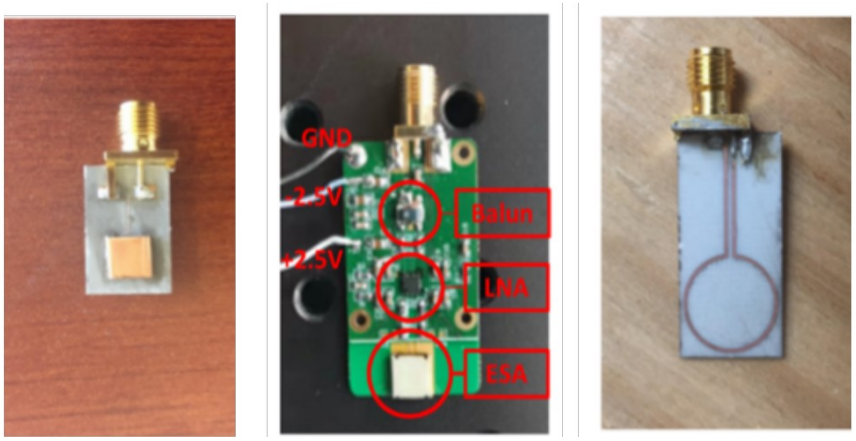

Figure 1.1: Prototypes of the thin-film ferrite loaded ESA: (a) the FMR enhanced ESA, (b) the FMR enhanced ESA with the LNA; (c) a standard small loop probe. Courtesy of [73].

The prototype of the aforementioned antenna is shown in Fig. 5.4. Compared with traditional ferrite-loaded antennas[31]-[34], it has several advantages. Firstly, the material's strong ferromagnetic resonance (FMR) predominantly dictates the antenna's resonant frequencies, making them largely independent of its structural dimensions. This characteristic allows simpler designs and smaller sizes in electronically scanned arrays (ESAs). Additionally, the resonant frequencies of ESAs can be widely adjusted by altering the DC biasing field. Secondly, the material's high permeability near the FMR point increases the input impedance of the ESA, aiding in impedance matching with other system components via the standard 50 Ohm interface without the need for extra matching circuits. Lastly, the ferrite material in the antenna enhances radiation efficiency by lowering the radiation Q, as it effectively prevents energy from being stored inside the antenna.

1.1.1.2 Filters

- **YIG Filters**

Microwave filters and oscillators that can be electronically tuned over a frequency range of a decade frequently utilize ferromagnetic resonance (FMR) in magnetic materials such as single crystals of Yttrium Iron Garnet (YIG). YIG-based devices are extensively used in testing equipment, radar, and electronic warfare (EW) systems due to their superior electronic tuning capabilities compared to other options like varactors, ferroelectrics, and microelectromechanical systems (MEMS). The narrow FMR linewidth of YIG, typically measured in Oersteds, facilitates high-quality resonators with an unloaded quality factor of 5000 at 10 GHz [38]. The FMR resonance frequency adjusts linearly with the magnetic field, following the relationship $f = \gamma H$, where γ is the gyromagnetic ratio (2.8 MHz/Oe). Research detailing magnetically tunable microwave bandpass and band-stop filters using single-crystal YIG resonators has been published in references [39] and [72], respectively, with a thorough discussion on YIG resonators and filters provided in [10].

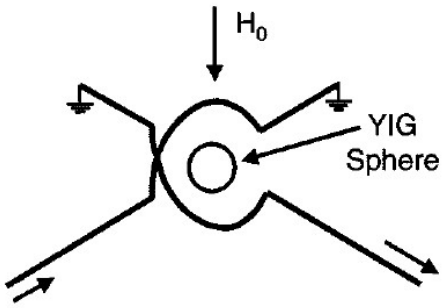

Figure 1.2: Coupling structure for a single-stage YIG sphere filter. Courtesy of [38].

The coupling mechanism for a single-stage filter is depicted in Fig. 5.5, featuring two orthogonal coupling loops encircling a YIG sphere. The radius of these loops determines the resonator's external coupling, with the smallest practical sizes constrained by the onset of magnetostatic wave (MSW) resonances. Currently, digitally controlled filters and oscillators capable of tuning across multiple octaves or even decades in frequency are commercially available. Recent advancements have concentrated on reducing the size of these components, enhancing compatibility with existing packaging technologies, and facilitating integration into more complex assemblies [38].

- **BaM Filters**

Recently, there has been a critical need to extend current microwave magnetic devices into the millimeter wave range to exploit the frequency spectrum further. Two important strategies have evolved to boost the operating frequency. One is to use high-$4\pi M_s$ ferromagnetic metals to replace the low-$4\pi M_s$ YIG ferrites. It has been demonstrated that using metallic thin films allows for the practical development of notch or band-stop [40] and bandpass filters [41]. The second strategy is to use low-loss hexagonal ferrites. The hexagonal ferrites have built-in high anisotropy fields and can provide a self-biasing for mm-wave applications in the 30–100 GHz range. Recent simulations have demonstrated the feasibility of hexagonal ferrite-based, stripline-type, mm-wave filters and phase shifters [42]. Experimentally, [43] demonstrates a prototype mm-wave notch filter based on a BaM slab with in-plane anisotropy. The device

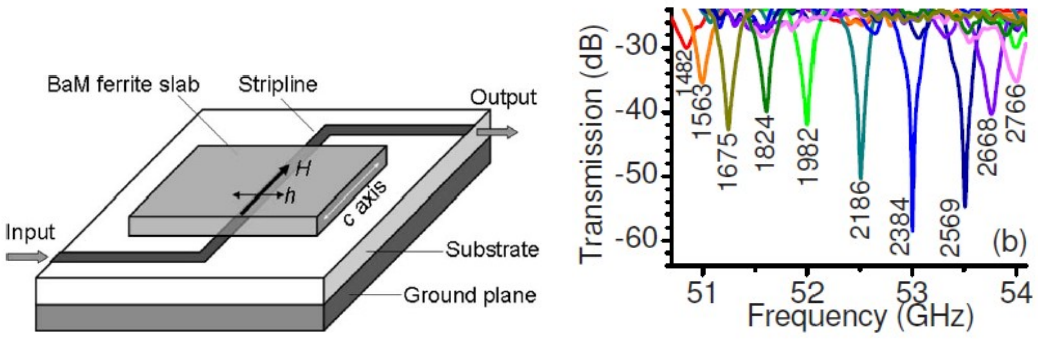

(a) (b)

Figure 1.3: (a)Structure and field configuration for a $BaFe_{12}O_{19}$ (BaM) ferrite-based notch filter. (b) Transmission profiles for ten different fields, as indicated. Courtesy of [43].

is compatible with monolithic integrated circuits. The demonstration uses a stripline device geometry, as depicted in Fig. 5.6(a). The BaM slab has an in-plane uniaxial anisotropy field of 17 kOe. This anisotropy field facilitates the operation of the filter over 51–54 GHz for an external field range of 1500–2700 Oe, as shown in Fig. 5.6(b).

In addition to notch filters, bandpass filters using hexagonal ferrites have also been demonstrated based on coupled waveguides [44]-[46]. In [44], M. Sterns et al. presented a novel tunable bandpass filter based on open-ended fine lines. Hexagonal ferrite spheres are used as resonators to cover a tuning frequency range from 39 GHz to 68 GHz. The measured insertion loss of the filter varies from 5.3 dB to 7 dB, with a typical 3 dB bandwidth between 300 MHz and 400 MHz. The stacking of two waveguides achieves off-resonance isolation of about 60 dB. Fig. 5.7 shows different views of a CAD model of the proposed coupling structure. It consists of two finlines separated by an iris. The cross-section of the filter arms has a staged profile to carry the substrates, which can be seen in Fig. 5.7 c). The fins must have an electroconductive connection to the housing to avoid parasitic modes. An indium solder has been used to connect the fins on the substrate to the channel walls. The spheres are placed directly on the substrate in the middle of a circular clearance in the metallization. The multi-slot iris is carefully designed to couple two resonator spheres while maintaining good

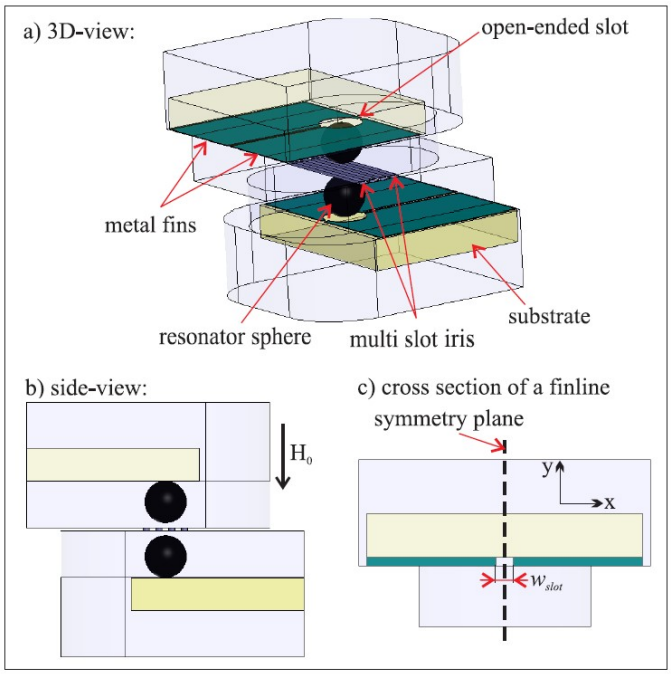

Figure 1.4: CAD model of the proposed coupling structure. a) 3D-view, b) side-view and c) cross-section of a finline. Courtesy of [44].

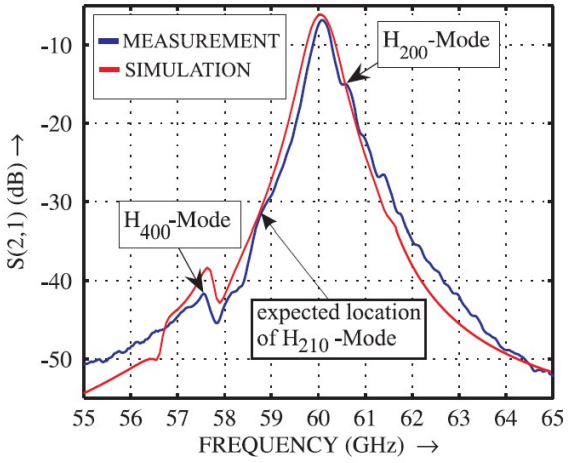

Figure 1.5: Comparison between measured and simulated resonance curves. Courtesy of [44].

off-resonance isolation. A comparison between a measured and a simulated resonance curve at 60GHz is illustrated in Fig. 5.8. A similar structure using shielded co-planar waveguides (CPW) is presented in [46].

1.1.1.3 Limiters

EW systems are required to work in a high-signal density environment, and receivers and signal processors are easily overloaded. A frequency-selective limiter (FSL) can be placed at the receiver front-end, attenuating strong signals without simultaneously attenuating other weaker signals. Most microwave FSLs utilize the frequency-selective nature of a magnetized ferrite. Above a critical RF magnetic-field level, the spin precession angle can increase no further, and coupling to higher-order spin waves grows exponentially. Energy is efficiently coupled to spin waves at approximately one-half the signal frequency and then into lattice vibrations (heat) in the ferrite. This mechanism has been analyzed in [86].

Ferrite FSLs have been implemented across various transmission line structures. For instance, non-resonant striplines built directly on single-crystal YIG films are capable of functioning over octave bandwidths [24]. In these devices, the insertion loss below the threshold is governed by the conventional conduction loss of the transmission line and the dielectric losses in the ferrite, which are typically minimal. Additionally, another variety of FSL utilizes the nonlinear excitation of spin waves in structures designed to propagate magnetostatic waves (MSWs). These devices have low limiting thresholds, reaching down to -30 dBm[47]. A detailed discussion on FSLs will be presented in Chapter 4.

1.1.1.4 Enhancers

A closely related nonlinear device is the signal-to-noise enhancer (SNE), which serves the opposite function of an FSL. At low signal levels, the SNE absorbs most of the signal energy. However, when signal levels are high, the absorption mechanism becomes saturated, allowing

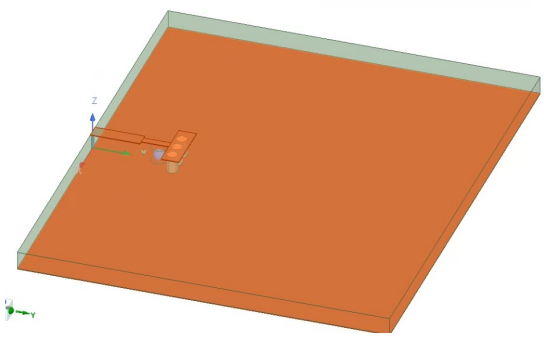

Properties of the Material

	Name	Type	Value	Units
	Relative Permittivity	Simple	20	
	Relative Permeability	Simple	1	
	Bulk Conductivity	Simple	0	siemens/m
	Dielectric Loss Tangent	Simple	0	
	Magnetic Loss Tangent	Simple	0	
	Magnetic Saturation	Simple	4600	gauss
	Lande G Factor	Simple	2	
	Delta H	Simple	32	Oe
	- Measured Frequency	Simple	55	GHz
	Mass Density	Simple	4600	kg/m^3

(a) (b)

Figure 1.6: (a)A schematic in HFSS with a ferrite sphere embedded inside the substrate. (b) Parameters to specify for ferrite materials in HFSS.

a larger portion of the signal to pass through. Like the FSL, this effect is frequency selective, enabling the SNE to attenuate low-level signals such as broadband noise while permitting strong, coherent signals to pass through with relatively minimal attenuation. The SNE employs MSWs in a thin-film structure [48] and was originally developed for use in frequency memory loops. Among its commercial applications, the SNE has notably enhanced detection sensitivity in DBS TV receivers [49].

1.1.2 Modeling of RF Magnetic Devices

Although ferrites have been utilized to construct various RF devices, their complex nature poses significant challenges to modeling such devices accurately and computationally efficiently. The state-of-art modeling and design tools are described in the following sections.

1.1.2.1 Full-Wave Modeling

Full-wave modeling tools such as the High-Frequency Structure Simulator (HFSS) [50] solve Maxwell's equations based on Polder's permeability tensor. In Fig. 5.9(a), a schematic plot with a ferrite sphere embedded inside the substrate is shown. Fig. 5.9(b) lists the material

properties of ferrites that the user can specify, including relative permittivity, magnetic saturation, Delta H, and its measured frequency. The relative permeability value is not meaningful because HFSS will replace it with Polder's permeability tensor. The advantage of HFSS is that it can solve ferrites in a linear regime, making it a good candidate for designing linear RF magnetic devices like filters and antennas. However, it can neither model the nonlinear property of the magnetic material nor include spin waves where exchange coupling is involved. What's more, to model the spin waves inside magnetic materials precisely, the meshing density has to be greater than that of the EM wave meshing density due to the fact that the spin waves' wavelength is smaller by more than an order of magnitude of the EM wavelength at the same frequency. Thus, the execution time for the simulator is usually tremendous.

1.1.2.2 Micromagnetics Modeling

Micromagnetics modeling is a computational approach used to study and predict the behavior of magnetic materials at the microscopic scale. This method is particularly valuable in understanding the complex interactions and dynamics of magnetic domains and domain walls within ferromagnetic and ferrimagnetic materials. Common micromagnetics simulators such as OOMMF or MuMax [51]-[55] solve the nonlinear Landau-Lifshitz-Gilbert (LLG) equation (equation of motion for electron spins inside ferrite materials) [56] at the micron scale, where magnetostatic approximation can be applied to model the dipole-to-dipole coupling and exchange coupling. The computational domain (the magnetic material) is divided into small cells, with the LLG equation solved numerically for each cell to simulate the time evolution of the magnetization across the entire material. Yet, computationally, it is no longer affordable in practical microwave devices when the scale of those interactions reaches millimeters, and the full-wave electrodynamic interactions must be considered.

1.1.2.3 Behavioral Modeling

Recently, behavioral modeling of FSLs was proposed, which treated FSLs as general nonlinear systems with memories and used mathematical models to predict their performance [57]. The mathematical model achieved good accuracy with moderate computation complexity, yet the physics of FSLs was obscured, and therefore, the model is not generalizable. Furthermore, despite the great success these modeling efforts have achieved in their respective domains of applications, the intuitive understanding of the physics in magnetic material is often overshadowed by the complexity of the mathematics.

1.1.3 Equivalent Circuit Modeling

With the limits and challenges of various existing modeling tools, building equivalent circuit models is advantageous because they can include magnetic materials' nonlinearity, non-reciprocity, and dispersive properties. Moreover, circuit simulators are intrinsically stable compared with micromagnetic simulators. In the 1960s, P. S. Carter et al. [101] proposed a gyrator/inductor model to represent the coupling of two coils through a YIG sphere. That model, however, did not define the circuit parameters based on the material parameters, nor did it include the resistors to represent the Gilbert damping in magnetic material. Later on, some equivalent circuits for other RF magnetic devices are exploited. Ferrite-core inductors, for example, play a significant role in electromagnetic noise suppression. Techniques for extracting equivalent circuit parameters, such as series resistance, inductance, and parasitic capacitance, are presented in [61]. This modeling approach also helps characterize ferrite materials' effective permeability. Similarly, the analysis of multi-element MRI coils benefits from advanced simulation techniques that integrate 3-D electromagnetic and RF circuit tools [62]. This integration facilitates accurate and efficient coil design, optimizing performance while ensuring safety through precise SAR mapping. In addition, [63] develops an RF circuit model for single-walled carbon nanotubes (SWNTs), considering both DC and capacitively

contacted geometries. The nanotube is modeled as a nano-transmission line with distributed kinetic and magnetic inductance and distributed quantum and electrostatic capacitance. The complex, frequency-dependent impedance is calculated for various measurement geometries. This model helps understand the electrical properties of SWNTs at high frequencies and has applications in determining the switching speed of nanotube-based electronic devices. Regarding nonlinear Rf magnetic devices, some empirical circuit models for FSLs have also been demonstrated in [58, 59, 60]. However, the major problem with these circuit models is that they had circuit parameters derived to match specific experimental results. As a result, the models were only applicable to specific devices.

This thesis aims to develop and utilize equivalent circuit representation of ferrite materials to facilitate a better understanding and design of RF magnetic devices. The advantages of the proposed circuit modeling are the following:

- **Physics-Based**: We want to develop a series of equivalent circuit models that can represent the dynamic spin precession physics and the propagation of spin waves in magnetic material for both linear and nonlinear cases. These circuit models will be derived rigorously from the micromagnetics theory, i.e., LLG equation [56]. Yet they describe the impact of material parameters, such as the biasing field, the saturation magnetization, and the material shapes on the spin precessions concisely and intuitively.

- **Computationally efficient**: The micromagnetic simulator needs to discretize the magnetic material so that the single unit dimension is close to the lattice constant, normally in the nanometer range. Hence, they can only compute very small dimensions up to 100 nm. The micromagnetic simulator cannot compute practical RF magnetic devices in millimeter dimensions. On the other hand, the full-wave simulator is only capable of performing linear simulations with a great computation cost. Compared with them, the circuit model can balance computation accuracy and efficiency. In

other words, the discretized circuit unit can cover a dimension around 100 times the lattice constant to reduce the number of discretized cells while still exhibiting a good performance inside a frequency band of interest. Besides, some simplification can also be done to accelerate the simulation further. Readers are encouraged to refer to Section 3.4.2, Section 4.4, and Appendix A for details.

- **Stability:** Utilizing a circuit simulator such as Keysight ADS to construct our circuit model, the model will be stable by the internal algorithm used by the simulator.
- **Scalability:** The models can also be scaled according to physical dimensions and be combined with other equivalent circuit models of practical devices, such as transmission lines and antennas, to create a complete equivalent circuit model of these RF magnetic devices.
- **Design-Friendly**: The model will aid the design of different RF magnetic devices.

1.2 Thesis Outline

In this dissertation, we discuss the modeling and design of RF magnetic devices using an equivalent circuit representation of spin dynamics. Below is a summary of each chapter.

Chapter 2 explores the quantum mechanical underpinnings of magnetism, focusing on the behavior of electron spins in ferrimagnetic materials. The discussion includes the derivation of the equation of motion for spinning electrons under an external magnetic field and the classifications of magnetic materials. The chapter also introduces and elaborates on key concepts like the Landau-Lifshitz-Gilbert (LLG) equation and different types of magnetic fields, providing a foundation for understanding the dynamic behaviors of magnetization in ferrimagnetic materials.

Chapter 3 develops equivalent circuit models to represent the dynamic spin precession and the propagation of spin waves in magnetic materials. The models are derived from the

LLG equation and aim to translate the micromagnetic behaviors into a circuit framework, which allows for intuitive understanding and easier simulation using standard circuit simulators. The chapter details linear and nonlinear models and validates them through practical RF device simulations, enhancing the understanding of ferrite-loaded RF components like antennas and transmission lines.

In Chapter 4, frequency-selective limiters (FSLs), crucial in protecting RF receivers from high-power signals, are modeled using physics-based equivalent circuits. The models integrate dynamic spin precession with spin wave propagation theories to simulate the interaction between electromagnetic and spin waves within these devices. This chapter also details the modeling processes for different types of FSLs. It validates the models through comparisons with measured data, establishing a robust framework for designing FSLs that function effectively across varying signal strengths and frequencies.

Chapter 5 focuses on designing and modeling millimeter wave resonators and filters using hexagonal ferrite spheres. It presents an equivalent circuit model for these resonators. This chapter also elaborates on the design process, including calibration techniques and integrating these resonators into bandpass filters. Experimental validations confirm the efficacy of the proposed designs in achieving desired resonant frequencies and bandpass phenomenon, marking a significant advancement in the application of ferrite materials in high-frequency domains.

Chapter 6 summarizes the thesis and points out future research directions.

CHAPTER 2

Micromagnetic Theory

2.1 Equation of Motion for a Spinning Electron

From quantum mechanics theory, the origin of magnetism is understood as the orderly motions of electron spins in magnetic materials. Depending on the reaction to the external field, the magnetic material can be classified into various categories: paramagnetic, diamagnetic, ferromagnetic, and ferrimagnetic [66, 67]. In the following discussion, we will limit our interest to ferrimagnetic material, in which the induced magnetic moment will align with the external magnetic field and increase the total magnetic flux in the material, as shown in Fig. 2.1. In addition, the 'ferrite' is short for ferrimagnetic material.

Figure 2.1: The influence of external magnetic field on the magnetic dipole in ferrimagnetic material.

An illustration of a spinning electron under an external magnetic field is shown in Fig. 2.2. When a magnetic bias field $\overrightarrow{H_0} = \hat{z}H_0$ is present, a torque will be exerted on the

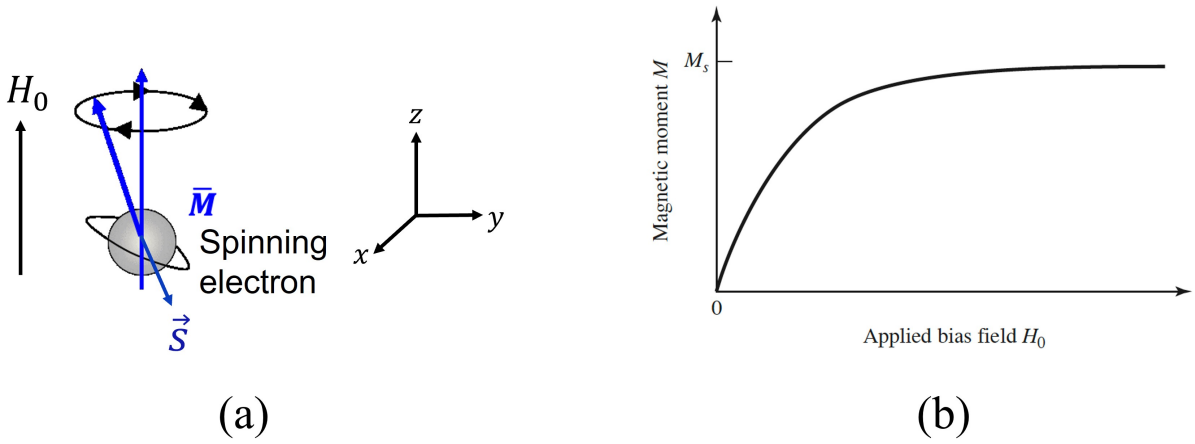

Figure 2.2: (a) Spinning magnetic dipole moment and angular momentum vector for a spinning electron. (b) Plot of total magnetization versus applied field.

magnetic dipole:

$$\vec{T} = \vec{M} \times \overrightarrow{B_0} = \mu_0 \vec{M} \times \overrightarrow{H_0} = -\mu_0 \gamma \vec{s} \times \overrightarrow{H_0} \tag{2.1}$$

And torque is equal to the time rate of change of angular momentum:

$$\vec{T} = \frac{d\vec{s}}{dt} = \frac{-1}{\gamma} \frac{d\vec{M}}{dt} = \mu_0 \vec{M} \times \overrightarrow{H_0} \tag{2.2}$$

Rewriting equation (2.2) results in the equation of motion (EoM) for the electron spin precession [69]:

$$\frac{d\vec{M}}{dt} = -\mu_0 \gamma \vec{M} \times \vec{H} \tag{2.3}$$

where $\vec{M}$ is the magnetic dipole moment, $\vec{H}$ is the total magnetic field, μ_0 is the free space permeability and γ is the gyromagnetic ratio of the electron. The equation of motion can be generalized to describe the dynamic behaviors of magnetization in magnetic material, with $\vec{M}$ now defined as the magnetization vector at a given observation location and $\vec{H}$ as the total effective magnetic field at the location which consists of an applied field, demagnetization field, anisotropic field, and exchange field according to their different physics origins [66] [67] [68]. In other words,

$$\vec{H} = \vec{H}_{appl} + \vec{H}_{demag} + \vec{H}_{anis} + \vec{H}_{ex} \tag{2.4}$$

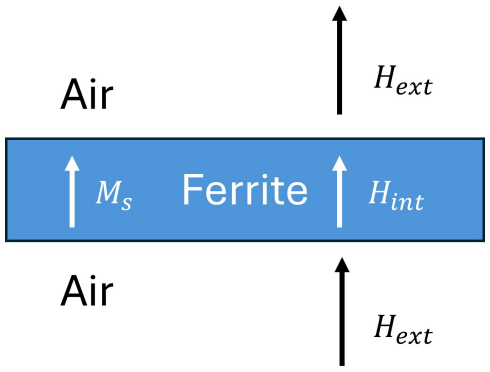

Figure 2.3: Internal and external magnetic fields for a thin ferrite film.

The detailed origin of each effective magnetic field is included in the following sub-sections.

It's important to note that the thermal fluctuation field is omitted in this context due to its relative weakness compared to the four aforementioned fields. However, the presence of a thermal field is crucial for the functionality of nonlinear RF magnetic devices like frequency selective limiters (FSL) [70][71], which require noise input to initiate spin wave oscillations.

- **Applied Field**

The applied field stems from Maxwellian principles. It refers to an external incident field. For example, a DC-applied field can be generated from an electromagnet, where coils are used to generate a DC bias field for ferrite applications. On the other hand, an RF-applied field can be generated from some transmission line structures, which serves as a perturbation on top of the DC bias field under the assumption of small signal analysis. The direction of the RF-applied field is usually perpendicular to the DC-applied field for applications in ferrite resonators, filters, and antennas [72][73]. However, there are cases when these two fields are in the same direction, like in frequency-selective limiters (FSLs) [70][71].

- **Demagnetization Field**

The demagnetization field reflects the interactions between magnetic dipoles within the material, specifically dipole-to-dipole interactions. Conventionally, in micromagnetics at scales

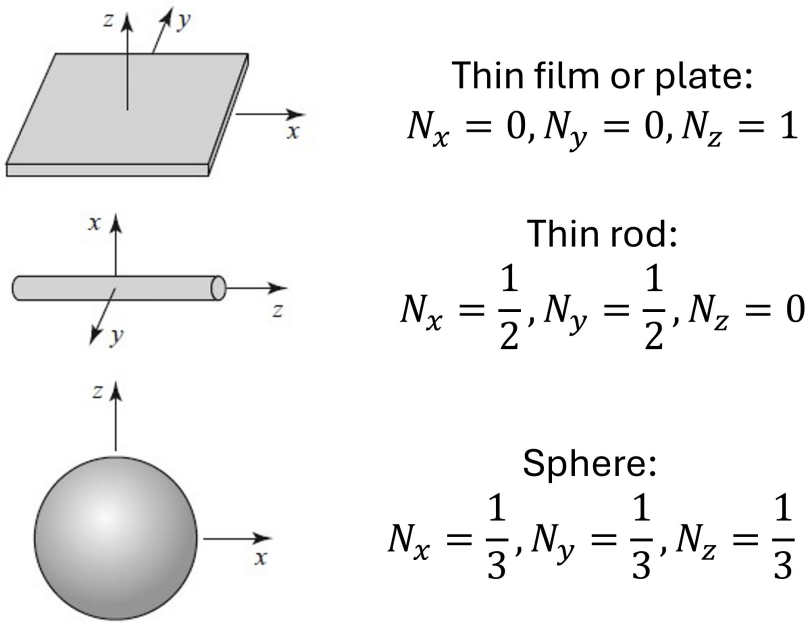

Figure 2.4: Demagnetization factors for some simple shapes

smaller than 10 micrometers, the demagnetization field is simplified as magnetostatic interactions, though it can be more accurately described through electrodynamics at larger scales.

Another way to understand the demagnetization field is through the boundary conditions at the surface of the ferrite [69]. For example, consider a thin ferrite film whose out-of-plane direction is along the biasing axis (Z-axis), as shown in Fig. 2.3. Because the external field H_{ext} is normal to the thin film, continuity of the normal component of B (B_n) at the surface gives

$$B_n = \mu_0 H_{ext} = \mu_0 (H_{int} + M_s) \tag{2.5}$$

Hence, the internal magnetic field H_{int} is

$$H_{int} = H_{ext} - M_s \tag{2.6}$$

This shows that the internal field is less than the external field by an amount equal to the saturation magnetization.

In general, the internal field, whether alternating current (AC) or direct current (DC), is influenced by the ferrite sample's shape and its alignment relative to the external field, and can be expressed as

$$\vec{H}_{int} = \vec{H}_{ext} - N \cdot \vec{M} \tag{2.7}$$

where N is defined as the demagnetization factor for that direction. Effectively, demagnetization fields can also be defined from demagnetization factor to be

$$\vec{H}_{demag} = -N \cdot \vec{M} \tag{2.8}$$

A summary of demagnetization factors for some simple structures is shown in Fig. 2.4. Note that the N_x, N_y, and N_z values correspond to the respective axis definition in the figure.

- **Anisotropy Field**

The anisotropy field and exchange field have atomic origins [66][67]. The anisotropic field emerges from spin-orbit coupling, directing the spins towards specific crystallographic axes of the material. It is the external magnetic field that must be applied to a magnetic material to align all the magnetic moments in the direction of the hard axis, which is the axis along which it is most difficult to magnetize the material. Essentially, it quantifies the strength of the magnetic field required to overcome the material's inherent anisotropy and fully align the magnetic moments against the anisotropy's preferred orientation.

- **Exchange Field**

The exchange field arises from the exchange interaction, a quantum mechanical phenomenon that leads to the coupling of magnetic moments within the material. This interaction is the result of the overlap between the electron wave functions of adjacent atoms or ions [74].

- **Saturation Magnetization**

When an external static magnetic field is applied to a ferrimagnetic material, the magnetic moments in Fig. 2.1 start to align with the field. As the strength of the applied field increases, more and more of these moments align until a point is reached where further increases in the magnetic field strength do not lead to an increase in net magnetization. This point is known as the saturation magnetization, or M_s. A sample plot for such a transition is shown in Fig. 2.2 (b).

In other words, the conservation of magnetization holds [74], i.e.,

$$M_s = \sqrt{M_x^2 + M_y^2 + M_z^2}. \tag{2.9}$$

Hence, if treating the magnetization as a vector in the Cartesian coordinate, there is a limit on the amplitude for the magnetization vector. For most RF and microwave applications, a magnetic material such as ferrite is operated under a strong DC biasing field that saturates the material in one direction. This is to prevent the formation of domains in magnetic material and energy loss associated with the rotation of domains under the influence of the RF field. The DC biasing field can be applied externally with a coil or a permanent magnet. It can also be applied by the internal anisotropic field of the material, which is called self-biased.

2.2 Landau-Lifshitz-Gilbert (LLG) Equation

When loss of the material due to the damping of the spin precession is considered, the equation of motion in equation (2.3) can be modified by including a damping term, resulting in the Landau-Lifshitz-Gilbert (LLG) equation [56],

$$\frac{\partial \vec{M}}{\partial t} = -\mu_0 \gamma \vec{M} \times \vec{H} + \frac{\alpha}{M_s} \vec{M} \times \frac{\partial \vec{M}}{\partial t} \tag{2.10}$$

where α is Gilbert's damping constant and M_s is the saturation magnetization of the material. Expanding the LLG equation to its scalar form yields,

$$\begin{aligned}
\frac{\partial M_x}{\partial t} &= -\mu_0\gamma\left(M_y H_z - M_z H_y\right) + \frac{\alpha}{M_s}\left(M_y\frac{\partial M_z}{\partial t} - M_z\frac{\partial M_y}{\partial t}\right) \\
\frac{\partial M_y}{\partial t} &= -\mu_0\gamma\left(M_z H_x - M_x H_z\right) + \frac{\alpha}{M_s}\left(M_z\frac{\partial M_x}{\partial t} - M_x\frac{\partial M_z}{\partial t}\right) \\
\frac{\partial M_z}{\partial t} &= -\mu_0\gamma\left(M_x H_y - M_y H_x\right) + \frac{\alpha}{M_s}\left(M_x\frac{\partial M_y}{\partial t} - M_y\frac{\partial M_x}{\partial t}\right).
\end{aligned} \tag{2.11}$$

Note that the LLG equation is a nonlinear equation that involves the product of magnetization vector and magnetic field.

2.2.1 Linear Form of the LLG Equation

With magnetocrystalline anisotropy and exchange coupling ignored, the magnetic field inside a ferrite can be expressed as

$$\vec{H} = H_0\hat{z} + H_x\hat{x} + H_y\hat{y}, \tag{2.12}$$

where H_0 is the applied DC biasing field and H_x, H_y are RF magnetic fields. For some RF applications that focus on the small-signal performance of the ferrite material, a small-signal assumption can be made:

$$|H_x| \ll H_0, |H_y| \ll H_0 \tag{2.13}$$

$$M_z = M_s \tag{2.14}$$

Substituting equations (4.7) and (4.8) to (4.6), the linearized LLG equation can be derived in the following form:

$$\frac{\partial M_x}{\partial t} = -\mu_0\gamma\left(M_y H_0 - M_s H_y\right) - \alpha\frac{\partial M_y}{\partial t} \tag{2.15}$$

$$\frac{\partial M_y}{\partial t} = \mu_0\gamma\left(M_x H_0 - M_s H_x\right) + \alpha\frac{\partial M_x}{\partial t} \tag{2.16}$$

$$\frac{\partial M_z}{\partial t} = 0. \tag{2.17}$$

Transforming equations (4.9) and (4.16) into the frequency domain yields,

$$j\omega M_x = -\left(\omega_0 + j\omega\alpha\right) M_y + \omega_m H_y \tag{2.18}$$

$$j\omega M_y = \left(\omega_0 + j\omega\alpha\right) M_x - \omega_m H_x \tag{2.19}$$

where ω is the operating angular frequency, $\omega_0 = \mu_0\gamma H_0$ and $\omega_m = \mu_0\gamma M_s$ are the angular frequency equivalents of the effective biasing field and the saturation magnetization.

2.2.2 Polder's Susceptibility Tensor

The solution of the above linearized LLG equation for unbound ferrite can be easily obtained by solving equations (2.18) and (2.19), which yields a frequency dispersive, anisotropic susceptibility tensor,

$$\begin{bmatrix} M_y \end{bmatrix} = \begin{bmatrix} \chi_{xx} & \chi_{xy} \\ \chi_{yx} & \chi_{yy} \end{bmatrix} \begin{bmatrix} H_x \\ H_y \end{bmatrix} \tag{2.20}$$

where,

$$\chi_{xx} = \chi_{yy} = \frac{\left(\omega_0 + j\alpha\omega\right)\omega_m}{\left(\omega_0 + j\alpha\omega\right)^2 - \omega^2} = \frac{\omega_m}{\omega_0}\frac{\omega_0^2 + j\alpha\omega\omega_0}{\omega_0^2 - \left(1+\alpha^2\right)\omega^2 + 2j\alpha\omega\omega_0} \tag{2.21}$$

$$\chi_{xy} = -\chi_{yx} = \frac{j\omega\omega_m}{\left(\omega_0 + j\alpha\omega\right)^2 - \omega^2} = \frac{\omega_m}{\omega_0}\frac{j\omega\omega_0}{\omega_0^2 - \left(1+\alpha^2\right)\omega^2 + 2j\alpha\omega\omega_0} \tag{2.22}$$

$\chi_{xx}, \chi_{yy}, \chi_{xy}, \chi_{yx}$ are called Polder's susceptibility tensor which is often used by RF and microwave engineers [69]. When loss is ignored, the susceptibility tensor can be simplified to the following,

$$\chi_{xx} = \chi_{yy} = \frac{\omega_0\omega_m}{\omega_0^2 - \omega^2} := X \tag{2.23}$$

$$\chi_{xy} = -\chi_{yx} = \frac{j\omega\omega_m}{\omega_0^2 - \omega^2} := j\kappa \tag{2.24}$$

Susceptibility tensor characterizes the response of a material's magnetization to an applied magnetic field. According to equations (2.21) and (2.22), the susceptibility starts from an initial value of ω_m/ω_0 at around the DC and reaches a resonance peak around the frequency ω_0.

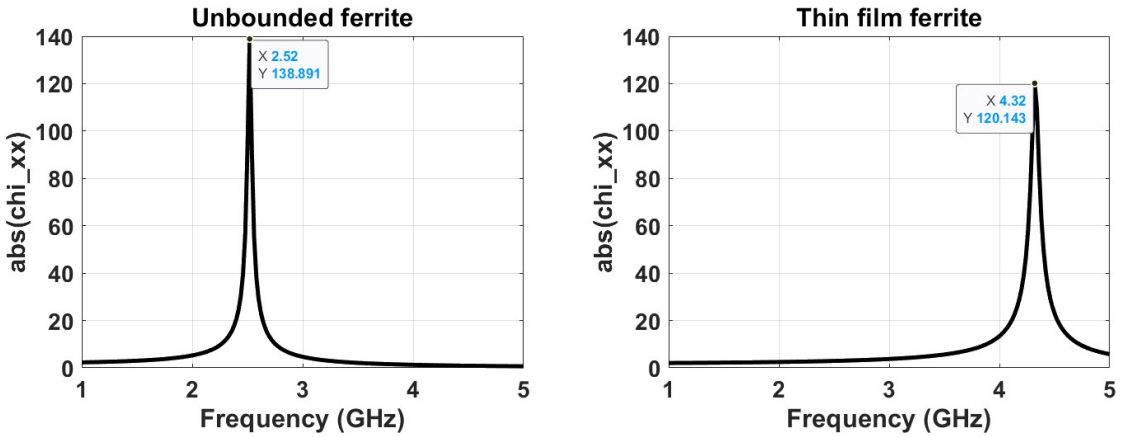

(a) (b)

Figure 2.5: $|\chi_{xx}|$ for (a) unbounded ferrite and for (b) thin-film ferrite with $H_0 = 900Oe, 4\pi M_s = 1750Guass, \alpha = 0.007$.

2.2.3 Ferromagnetic Resonance (FMR)

The ferromagnetic resonance (FMR) frequency is defined as the frequency when the susceptibility peaks. In a ferromagnetic resonance experiment, the resonance condition is met when the frequency of the oscillating field matches the natural precession frequency of the magnetization, indicating a strong response of the magnetization to the oscillating field. In other words, the natural precession frequency is set by the DC biasing field, and an oscillating field, i.e., an RF field, serves as a perturbation or excitation to the spin precession. It is worth noticing that the FMR setup is still within the small-signal assumption scenario, where the DC biasing field is much larger than the RF fields. They are perpendicular to each other according to equation (2.36).

The FMR frequency is an important material property and is also dependent on the strength and direction of the bias field.

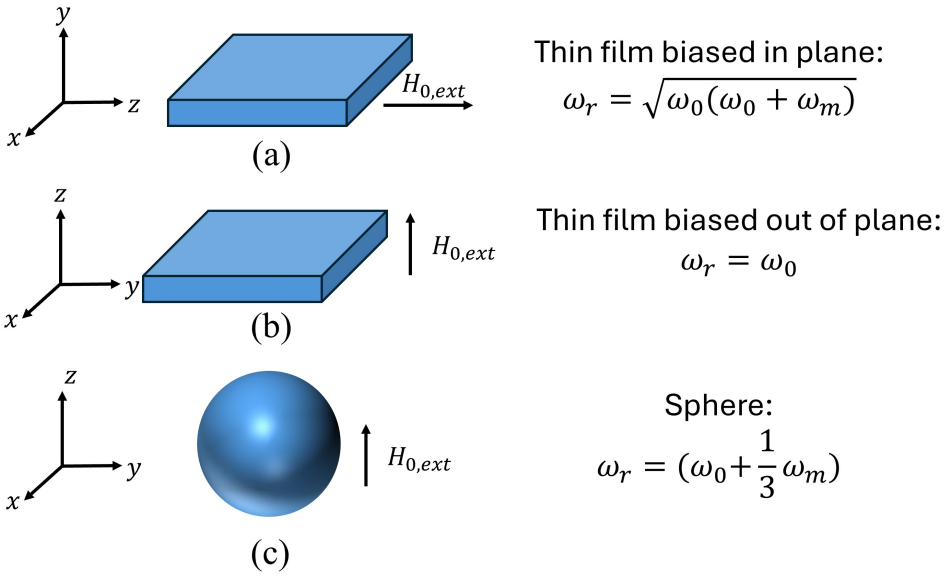

Figure 2.6: FMR frequency for (a)thin film biased in the plane, (b) out of the plane, and (c) sphere.

2.2.3.1 FMR Frequency for Unbounded Ferrite

For unbounded ferrite, the angular FMR frequency ω_r is given by

$$\omega_r = \omega_0. \tag{2.25}$$

Fig. 2.5 (a) plots the absolute value of χ_{xx} versus frequency for an unbounded (infinitely large) ferrite according to equation (2.21). The DC bias field is $900Oe$, resulting in $\omega_0 = \mu_0\gamma H_0 = 1.58e^{10}/s$. The FMR frequency $f_r = \omega_0/(2\pi) = 2.52GHz$, which corresponds to the peak frequency for $|\chi_{xx}|$.

2.2.3.2 FMR Frequency for Thin Film Ferrite Biased Out-of-Plane

For ferrite plates or thin films whose out-of-plane direction is along the biasing axis (Z-axis), a demagnetization field is applied in the opposite direction of the biasing which reduces the effective biasing field in the material to $(H_0 - M_s)$, as shown in Fig. 2.6(b). Polder's

susceptibility tensor can be obtained in the same form by simply substituting the relation $\omega_0 = \mu_0\gamma(H_0 - M_s)$ in equation (2.21) and (2.22). Consequently, the FMR frequency is given by

$$\omega_r = \omega_0 = \mu_0\gamma(H_{0,ext} - M_s). \tag{2.26}$$

2.2.3.3 FMR Frequency for Thin Film Ferrite Biased in-Plane

For ferrite plates or thin films with an in-plane biasing in the Z-axis and out-of-plane direction in the Y-axis, the demagnetization field becomes part of the RF field, as shown in Fig. 2.6(a). Because $N_x = N_z = 0, N_y = 1$ for thin films, the internal RF magnetic field is related to the applied RF magnetic field by:

$$H_y = H_{y,appl} - M_y \tag{2.27}$$

$$H_x = H_{x,appl}. \tag{2.28}$$

Substituting equations (2.27) and (2.28) to equations (2.18) and (2.19), the linearized LLG equation thus becomes,

$$j\omega M_x = -\left(\omega_0 + j\omega\alpha\right) M_y + \omega_m \left(H_{y,appl} - M_y\right) \tag{2.29}$$

$$j\omega M_y = \left(\omega_0 + j\omega\alpha\right) M_x - \omega_m H_{x,appl} \tag{2.30}$$

When an external RF magnetic field is applied only to the X-axis, the resulting magnetization susceptibility is given by,

$$\chi_{xx} = \frac{M_x}{H_{x,appl}} = \frac{\omega_m}{\omega_0} \frac{\omega_r^2 + j\alpha\omega\omega_0}{\omega_r^2 - \left(1 + \alpha^2\right)\omega^2 + j\alpha\omega\left(2\omega_0 + \omega_m\right)} \tag{2.31}$$

where ω_r is the thin film FMR frequency, which is given by,

$$\omega_r = \sqrt{\omega_0\left(\omega_0 + \omega_m\right)}. \tag{2.32}$$

Fig. 2.5 (b) plots the absolute value of χ_{xx} versus frequency for a thin film ferrite according to equation (2.31). Similarly, the DC bias field is $900Oe$, and a saturation magnetization

of $4\pi M_s = 1750 Gauss$ is assumed. The theoretical FMR frequency can be calculated using equation (2.32), which gives $f_r = \omega_r/(2\pi) = 4.32 GHz$. Obviously, it also corresponds to the frequency where the χ_{xx} peaks. Comparing equation (2.32) to (2.25), it is evident that the FMR of the thin film ferrite is much higher than that of the unbound ferrite, when $\omega_m \gg \omega_0$. The initial susceptibility and the shape of the susceptibility dispersion remain similar for both cases. This implies that the in-plane biased thin film ferrite may be more appropriate for RF and microwave applications due to the lower required biasing field to reach a high FMR and, thus, a higher initial permeability.

2.2.3.4 FMR Frequency for Arbitrarily Shaped Ferrite

The FMR frequency for arbitrarily shaped ferrite is given by Kittel's equation when the Z-axis is assumed to be the bias direction [69]:

$$\omega_r = \omega = \sqrt{(\omega_0 + \omega_m N_x)\,(\omega_0 + \omega_m N_y)}. \tag{2.33}$$

The ω_0 and ω_m are defined as follows:

$$\omega_0 = \mu_0 \gamma H_{0,effective} = \mu_0 \gamma (H_{0,ext} - N_z M_s + H_a) \tag{2.34}$$

$$\omega_m = \mu_0 \gamma M_s \tag{2.35}$$

In practice, it is convenient to substitute $\mu_0 \gamma = 2\pi \cdot 2.8 MHz/Oe$. And H_a is the anisotropy field.

2.3 Ferrite Material Properties

Table 3.1 summarizes some key material properties of several kinds of ferrites. Hexaferrite, spinel ferrite, and garnet ferrite are all types of ferrimagnetic materials, but they differ in their chemical composition, crystal structure, and magnetic properties [67]. Hexaferrites, or barium hexaferrites, are characterized by their hexagonal crystal structure. Spinel ferrites

Table 2.1: Ferrimagnetic material properties[67]

	Material	Abbr	Landé g-factor	$4\pi M_s$ (Gauss)	Anisotropy field (Oe)	Coercive field (Oe)
Hexaferrite	$BaFe_{12}O_{19}$	BaM	1.87	4000	17460	1935
	$SrFe_{12}O_{19}$	SrM		4320	16000	6635
	$Ba_4Zn_2Fe_{36}O_{60}$	Zn_2U		4223	10038	2580
Spinel	$MgFe_2O_4$	MgFO	2.06	2150	173	1.8
	$MnFe_2O_4$	MnFO	2.20	4000	5400	196
	$CoFe_2O_4$	CFO		5370	6800	1566
Garnet	$Y_3Fe_5O_{12}$	YIG	2.00	1750	82	

have a cubic crystal structure with the general formula AB_2O_4, where "A" is a divalent metal ion (such as Fe, Ni, Mn, Mg, Zn, etc.) and "B" is a trivalent metal ion (usually Fe). Garnet ferrites, more commonly known as rare-earth iron garnets, have a complex cubic lattice structure with the general chemical formula of $3Fe_2O_3 * 5X_2O_3$, where "X" represents a rare-earth element such as yttrium (Y) or gadolinium (Gd). Yttrium iron garnet (YIG, $Y_3Fe_5O_{12}$) is a well-known example.

A brief explanation for each parameter is included below.

- **Landé g-factor**: The Landé g-factor is a factor used in quantum mechanics and atomic physics to describe the magnetic moment of an atom, ion, or molecule in terms of its angular momentum. It is influenced by factors such as the type of ferrite (e.g., spinel, garnet), the distribution of metallic ions in the crystal lattice, and the interactions between those ions. Considering only the electron's spin magnetic moment (and neglecting orbital contributions), the g-factor is theoretically exactly 2. In practice, it is also approximated to be 2 for most materials.

- **Saturation magnetization**: Saturation magnetization for ferrite refers to the max-

imum magnetization that a ferritic material can achieve when subjected to a large external magnetic field. Beyond this point, even if the magnetic field intensity is increased, there will be no significant increase in the material's magnetization. This occurs because all the magnetic moments in the ferrite have become aligned with the external field. In addition, it should be noted that both M_s and $4\pi M_s$ are the symbols for saturation magnetization. The unit for M_s is emu/cm^3 (electromagnetic units per cubic centimeter) in the CGS (centimeter-gram-second) system. When converting to the SI (International System of Units) system, where the unit of magnetization is A/m (amperes per meter), $1emu/cm^3$ corresponds to $10^3 A/m$. The unit for $4\pi M_s$ is Gauss in the CGS system, and $1Gauss$ corresponds to $10^3/(4\pi)A/m$ in the SI system.

- **Anisotropy field**: The anisotropy field, often denoted as H_a, is the external magnetic field that must be applied to a magnetic material to align all the magnetic moments in the direction of the hard axis. In Table 3.1, hexaferrite has a much larger anisotropy field compared with other kinds of ferrite materials. This property facilitates the potential for high-frequency applications because the large anisotropy field can raise the FMR frequency to the millimeter-wave band.

- **Coercive field**: The coercive field H_c for a ferrite material refers to the intensity of the external magnetic field that must be applied in the opposite direction to reduce the magnetization of the ferrite to zero after it has been magnetized to saturation. In other words, it's the measure of the resistance of the ferrite to becoming demagnetized.

2.4 Spin Wave

Spin waves can be understood from multiple perspectives. From the wave perspective, spin waves can be understood as electromagnetic (EM) waves that propagate inside ferrimagnetic materials, affected by the material properties and biasing fields. From the particle perspective, spin waves are also known as 'magnons', which represent collective excitations within

an ordered array of spins in ferrimagnetic materials. For both perspectives, it is common to describe spin waves from the dispersion relationship [74]. In this section, the dispersion relation is derived from the wave perspective. Readers are encouraged to read Chapter 5 of [74] for more details.

2.4.1 Dispersion Relation Without Exchange Coupling

Under magnetostatic approximation, Maxwell's equations become:

$$\begin{aligned} \nabla \times \vec{H} &= 0 \\ \nabla \cdot \vec{B} &= 0 \\ \nabla \times \vec{E} &= j\omega \vec{B} \end{aligned} \tag{2.36}$$

where $\vec{B} = [\mu]\vec{H} = \mu_0([U] + [\chi])$. The susceptibility tensor is defined in Section 3.3.2 to be

$$[\chi] = \begin{bmatrix} \chi_{xx} & \chi_{xy} & 0 \\ \chi_{yx} & \chi_{yy} & 0 \\ 0 & 0 & 0 \end{bmatrix} = \begin{bmatrix} X & -j\kappa & 0 \\ j\kappa & X & 0 \\ 0 & 0 & 0 \end{bmatrix} \tag{2.37}$$

The constants X and κ are defined in equations (2.45) and (2.46).

Substituting equation (2.37) to (2.36) and representing $\vec{H} = -\nabla\psi$, Walker's equation is derived:

$$(1 + X)\left[\frac{\partial^2\psi}{\partial x^2} + \frac{\partial^2\psi}{\partial y^2}\right] + \frac{\partial^2\psi}{\partial z^2} = 0. \tag{2.38}$$

The solutions of Walker's equation are commonly referred to as magnetostatic modes.

Assuming plane wave propagation, the dispersion relationship can be solved from Walker's equation to be

$$\omega = \left[\omega_0\left(\omega_0 + \omega_m \sin^2\theta\right)\right]^{1/2} \tag{2.39}$$

where θ is the angle of propagation with respect to the bias direction. Note that this dispersion relation is independent of the magnitude of k, which indicates that plane waves at this frequency ω can have any wavelength. This phenomenon is plotted in Fig. 2.7

(a), where both $\theta = 0$ and $\theta = 90^o$ are considered. For intermediate propagation angles, the frequency will lie between these two extremes. It is worth noticing that this frequency degeneracy in the magnetostatic approximation is removed by considering the effects of either finite sample boundaries or the exchange interaction, as discussed below.

2.4.2 Dispersion Relation With Exchange Coupling

With exchange coupling, the effective magnetic field includes an additional exchange magnetic field, i.e.,

$$\overrightarrow{H_{eff}} = \vec{H} + \overrightarrow{H_{ex}} \tag{2.40}$$

The exchange magnetic field is proportional to the spatial differentiation of the magnetization vector, i.e.,

$$\overrightarrow{H_{ex}} = \lambda_{ex} \nabla^2 \vec{M} \tag{2.41}$$

where λ_{ex} is the exchange constant ($\lambda_{ex} = 3 * 10^{-16} m^2$ for YIG). In other words, the exchange field arises when the magnetization vector inside a ferrite is not spatially uniform, where adjacent magnetization vectors are interacting with each other.

To quantify the effect of exchange coupling, the susceptibility tensor needs to be inverted to express $\vec{H}$ in terms of $\vec{M}$.

Rewriting equation (2.20) gives

$$\begin{bmatrix} M_x \\ M_y \end{bmatrix} = \begin{bmatrix} X & j\kappa \\ -j\kappa & X \end{bmatrix} \begin{bmatrix} H_x \\ H_y \end{bmatrix} \tag{2.42}$$

where $X = \frac{\omega_0 \omega_m}{(\omega_0)^2 - \omega^2}$ and $\kappa = \frac{\omega \omega_m}{(\omega_0)^2 - \omega^2}$.

Expanding equation (2.42) leads to

$$M_x = X H_x + j\kappa H_y \tag{2.43}$$

$$M_y = -j\kappa H_x + X H_y \tag{2.44}$$

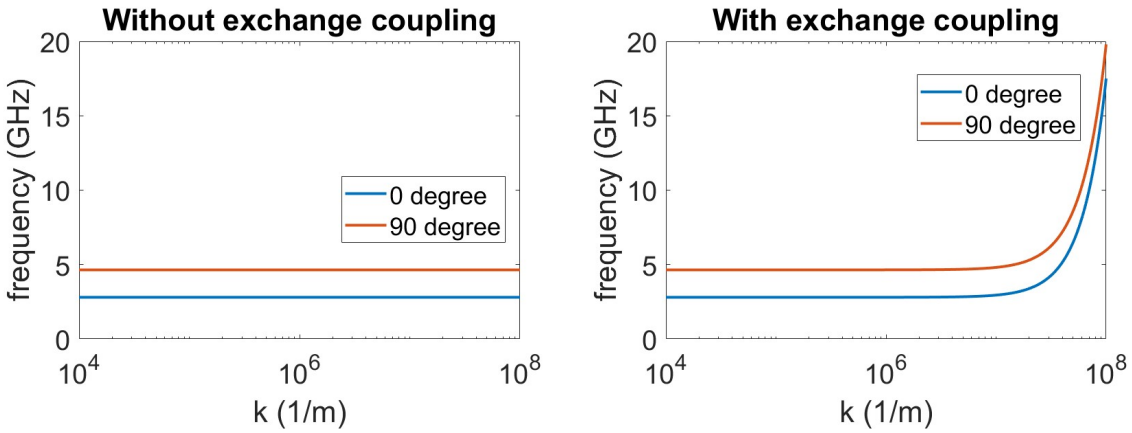

(a) (b)

Figure 2.7: (a)Magnetostatic wave dispersion relations without exchange for propagation parallel (0-degree) and perpendicular (90-degree) to the applied bias field. (b)Magnetostatic wave dispersion relations with exchange for propagation parallel (0-degree) and perpendicular (90-degree) to the applied bias field. $\lambda_{ex} = 3e^{-16}$, $H_0 = 1000Oe$, $4\pi M_s = 1750Gauss$.

Solving equations (2.43) and (2.44) and substituting the expressions for X and κ gives the following relation between $\vec{H}$ and $\vec{M}$:

$$\begin{bmatrix} H_x \\ H_y \end{bmatrix} = \frac{1}{\omega_m} \begin{bmatrix} \omega_0 & j\omega \\ -j\omega & \omega_0 \end{bmatrix} \begin{bmatrix} M_x \\ M_y \end{bmatrix} := [A_{op}] \begin{bmatrix} M_x \\ M_y \end{bmatrix} \tag{2.45}$$

With exchange coupling, equations (2.18) and (2.19) are modified to include additional terms, and become the following:

$$j\omega M_x = -\left(\omega_0 + j\omega\alpha\right) M_y + \omega_m(H_y + \nabla^2 M_y) \tag{2.46}$$

$$j\omega M_y = \left(\omega_0 + j\omega\alpha\right) M_x - \omega_m(H_x + \nabla^2 M_y) \tag{2.47}$$

Solving equations (2.46) and (2.47) leads to a different relation between $\vec{H}$ and $\vec{M}$:

$$\begin{bmatrix} H_x \\ H_y \end{bmatrix} = \frac{1}{\omega_m} \begin{bmatrix} \omega_0 - \lambda_{ex}\omega_m\nabla^2 & j\omega \\ -j\omega & \omega_0 - \lambda_{ex}\omega_m\nabla^2 \end{bmatrix} \begin{bmatrix} M_x \\ M_y \end{bmatrix} := [A'_{op}] \begin{bmatrix} M_x \\ M_y \end{bmatrix} \tag{2.48}$$

Assuming plane wave propagation, ∇^2 can be replaced by $(-k^2)$, where k is the propagation constant of the spin wave. Hence, equation (2.48) becomes

$$\begin{bmatrix} H_x \\ H_y \end{bmatrix} = \frac{1}{\omega_m} \begin{bmatrix} \omega_0 + \lambda_{ex}\omega_m k^2 & j\omega \\ -j\omega & \omega_0 + \lambda_{ex}\omega_m k^2 \end{bmatrix} \begin{bmatrix} M_x \\ M_y \end{bmatrix} := [A'_{op}] \begin{bmatrix} M_x \\ M_y \end{bmatrix} \tag{2.49}$$

Since the exchange term $\lambda_{ex}\omega_m k^2$ appears everywhere with ω_0, the effects of exchange can be easily added to the previous magnetostatic plane wave analysis by replacing ω_0 with $\omega_0 + \lambda_{ex}\omega_m k^2$. The dispersion relation (2.39) thus is modified to be

$$\omega = \left[(\omega_0 + \lambda_{ex}\omega_m k^2) \left((\omega_0 + \lambda_{ex}\omega_m k^2) + \omega_m \sin^2\theta \right) \right]^{1/2} \tag{2.50}$$

where a is the lattice constant ($a = 1.2nm$ for YIG) and k is the propagation constant. Note that exchange coupling has restored a one-to-one correspondence between frequency w and propagation constant k.

The dispersion relation with exchange coupling is plotted in Fig. 2.7 (b). Compared with Fig. 2.7 (a), several observations can be made:

- The exchange coupling has restored a one-to-one correspondence between ω and k.
- The exchange coupling has facilitated a higher frequency signal to propagate inside the ferrite material.
- The exchange coupling changes the dispersion dramatically only when k is large. This is attributed to the fact that λ_{ex} is small.

CHAPTER 3

Equivalent Circuit Model for Spin Precession and Spin Waves

This chapter will derive the linear and nonlinear equivalent circuit model based on the LLG equation. The linear circuit equivalence is a two-port model representing the X and Y-direction excitation of the spin units when the ferrite is biased in the Z-direction. When one of the ports is terminated due to the demagnetization effect of the thin-film ferrite material, the two-port circuit model will reduce to a parallel RLC circuit whose resonance frequency is the same as the FMR frequency. Afterwards, two examples are utilized to demonstrate the validity of such a linear RLC model. The first example is the short-circuited microstrip line loaded with thin-film ferrite. The second example is the electrically small loop antenna loaded with thin film YIG that operates at FMR frequency. The circuit model can predict the antenna's radiation efficiency and input impedance.

3.1 Field to Circuit Transformation

The rationale for representing the behavior of magnetic material with equivalent circuit models is established based on Maxwell's equations. Faraday's law indicates the electromotive force, a form of voltage, is the time rate change of the magnetic flux. Similarly, current can be related to a magnetic field through Ampere's law. To illustrate this concept, one may consider a cubic cell within an unbound volume of ferrite shown in Fig. 3.1.1. The cell has dimensions of Δx,Δy, and Δz along the X, Y, Z axes. The DC biasing field is applied to the

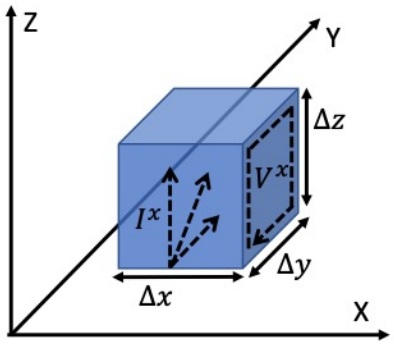

Figure 3.1: A cuboid cell in ferrite where the correspondence of field variables (H, M) to the circuit variables (I, V) is established.

Z-axis. Applying Faraday's law, the electromotive force around the perimeter of the surface $\Delta y \times \Delta z$ denoted by V^x is related to the X-component of the dynamic magnetization vector by,

$$V^x = \mu_0 \frac{\partial M_x}{\partial t} \Delta y \Delta z \tag{3.1}$$

On the other hand, the current flowing crossing the X-axis, either toward the Y or the Z-axis must have a contribution from the x-component of the Maxwellian magnetic field according to Ampere's law. This contribution can be denoted by,

$$I^x = H_x \Delta x \tag{3.2}$$

Equations (3.1) and (3.2) are called field-to-circuit transformations. Equivalent circuits for magnetic materials can thus be defined between the voltage and current.

3.2 Linear Equivalent Circuit Models

3.2.1 Equivalent Circuit Model for a Biased Magnetic Material Cell

For a small biased cuboid cell, the magnetization and magnetic field can be assumed to be uniform. Decomposing $\vec{M}$ into its three components yields

$$\vec{M} = M_x \hat{x} + M_y \hat{y} + M_z \hat{z} \approx M_z \hat{z} \approx M_s \hat{z} \tag{3.3}$$

For finite dimension ferrites, the internal magnetic field $\vec{H}$ is different from the external magnetic field due to demagnetization, i.e.,

$$\begin{aligned} \vec{H} &= H_x\hat{x} + H_y\hat{y} + H_z\hat{z} \\ &= (H_{xe} - N_x M_x)\,\hat{x} + (H_{ye} - N_y M_y)\,\hat{y} + (H_{ze} - N_z M_z)\,\hat{z}. \end{aligned} \tag{3.4}$$

Assuming the bias field is applied in the Z-direction,

$$H_{ze} = H_0 \tag{3.5}$$

Applying field-to-circuit transformations for all magnetization and magnetic field components, the linearized LLG equations (4.9) and (4.16) can now be rewritten as circuit equations,

$$I_x = -\frac{V_y}{Z_g} + \frac{\int V_x dt}{L_x} + \frac{\int V_x dt}{L_{dx}} + \frac{V_x}{R_x} \tag{3.6}$$

$$I_y = \frac{V_x}{Z_g} + \frac{\int V_y dt}{L_y} + \frac{\int V_y dt}{L_{dy}} + \frac{V_y}{R_y} \tag{3.7}$$

with Z_g, L_x, L_y, L_{dx}, L_{dy}, R_x and R_y defined as follows,

$$\begin{cases} Z_g = \mu_0\omega_m\Delta z = \mu_0^2\gamma M_s\Delta z \\ L_x = \mu_0\dfrac{M_s}{H_0}\dfrac{\Delta y\Delta z}{\Delta x} \\ L_y = \mu_0\dfrac{M_s}{H_0}\dfrac{\Delta x\Delta z}{\Delta y} \\ L_{dx} = \dfrac{\mu_0 yz}{(N_x - N_z)\,x} \\ L_{dy} = \dfrac{\mu_0 xz}{(N_y - N_z)\,y} \\ R_x = \mu_0\dfrac{\omega_m}{\alpha}\dfrac{\Delta y\Delta z}{\Delta x} = \dfrac{\mu_0^2\gamma M_s}{\alpha}\dfrac{\Delta y\Delta z}{\Delta x} \\ R_y = \mu_0\dfrac{\omega_m}{\alpha}\dfrac{\Delta x\Delta z}{\Delta y} = \dfrac{\mu_0^2\gamma M_s}{\alpha}\dfrac{\Delta x\Delta z}{\Delta y} \end{cases} \tag{3.8}$$

The ω_m is defined in the same way as in the previous Chapter:

$$\omega_m = \mu_0\gamma M_s \tag{3.9}$$

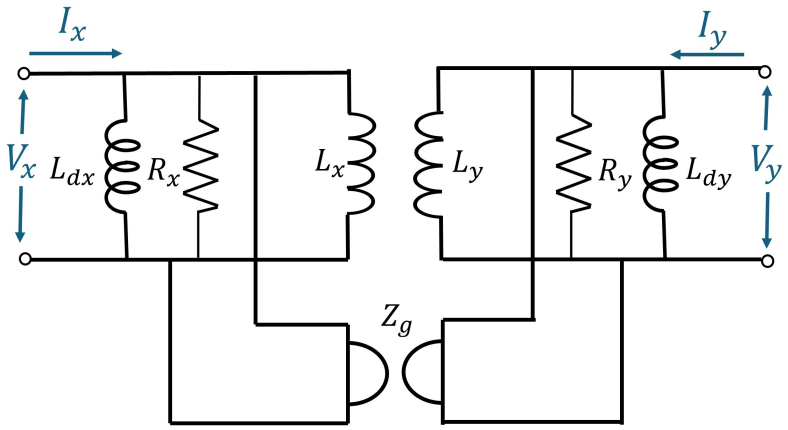

Figure 3.2: Equivalent circuit derived for a biased magnetic material cell representing its linear, dynamic, and non-reciprocal magnetization behavior.

Considering the left-hand sides of the equations (3.6) and (3.7) as incident currents I_x and I_y, the four terms on the right-hand side can be considered as currents flowing into an inductor I_{Lx} or I_{Ly} (I_{Ldx} or I_{Ldy}) and a resistor I_{Rx} or I_{Ry} and a gyrator I_{Gx} or I_{Gy}, respectively. It is evident that equations (3.6) and (3.7) represent a two-port circuit with each of the ports loaded by a resistor and two inductors while the two ports are coupled through a gyrator, as shown in Fig. 3.2. Z_g is the impedance of the gyrator, L_x, L_y, L_{dx}, L_{dy}, R_x, and R_y represent the values of the loaded inductors and resistors for both X-port and Y-port. The physical meaning of each circuit component is summarized below:

- L_x and L_y: Increase of the magnetic flux brought by the magnetic material in the X- and Y-direction, respectively.
- L_{dx} and L_{dy}: Demagnetization effects due to shape anisotropy.
- R_x and R_y: Damping loss in the ferrite material.
- Z_g: The use of a gyrator in the equivalent circuit is to model the non-reciprocity of the magnetic material and the sign of the gyrator determines the right-hand rotation characteristics of the spin precession.

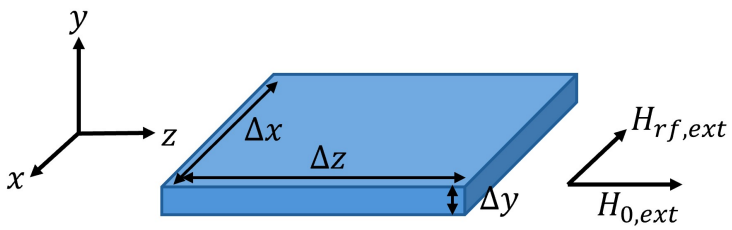

Figure 3.3: A thin film ferrite material with in-plane dimensions $\Delta x \times \Delta z$ and out-of-plane dimension Δy. A DC bias field is applied in the Z direction and an RF magnetic field is applied in the X direction.

Note that a similar gyrator/inductor model was proposed in [70] to represent the coupling of two coils through a YIG sphere. That model, however, did not define the circuit parameters based on the material parameters, nor did it include the resistors to represent the Gilbert damping in magnetic material.

3.2.2 Equivalent Circuit Model for Thin-Film Magnetic Material

Thin film magnetic materials are commonly used in RF magnetic devices by virtue of their planar structure and easy assembly. Hence, it is important to derive the equivalent circuit model for them. Fig. (3.3) shows a schematic plot for a piece of thin-film ferrite that is biased in-plane at Z-direction. Besides the DC bias field $H_{0,ext}$, an RF magnetic field serves as an excitation for the spin precession. In general, the RF magnetic field can be in arbitrary directions. However, a stronger interaction happens when the RF field is perpendicular to the DC biasing field, i.e., in the X-direction as shown in Fig. 3.3.

Substituting $N_y = 1$ for thin-film ferrite, the circuit elements values' are derived from

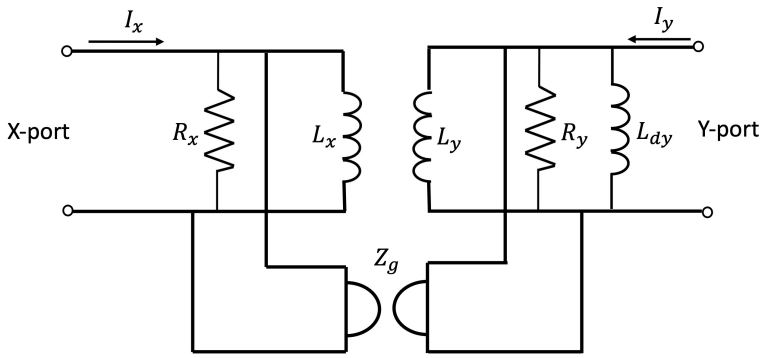

Figure 3.4: Equivalent circuit model for thin film magnetic material biased in-plane and excited at both X and Y directions.

equation (3.8) to be the following,

$$\begin{cases} Z_g = {\mu_0}^2 \gamma M_s \Delta z \\ L_x = \mu_0 \dfrac{M_s}{H_o} \dfrac{\Delta y \Delta z}{\Delta x} \\ L_y = \mu_0 \dfrac{M_s}{H_o} \dfrac{\Delta x \Delta z}{\Delta y} \\ L_{dy} = \dfrac{\mu_0 \Delta x \Delta z}{\Delta y} \\ R_x = \dfrac{\gamma {\mu_0}^2 M_s \Delta y \Delta z}{\alpha \Delta x} \\ R_y = \dfrac{\gamma {\mu_0}^2 M_s \Delta x \Delta z}{\alpha \Delta y} \end{cases} \tag{3.10}$$

Note that L_{dx} becomes effectively open-circuited and is not included in Fig. (3.4).

With the RF magnetic field in the X-direction only, the two-port circuit model can be further simplified to a one-port circuit looking from the X-direction, as shown in Fig. 3.5. The parallel connected L_y and L_{dy} are transformed through the gyrator to form a capacitor C_x. On the other hand, the R_y is transformed to form a different resistor $R_x^{(2)}$. Hence, the equivalent circuit for X-port becomes a parallel RLC resonator. Assume the damping

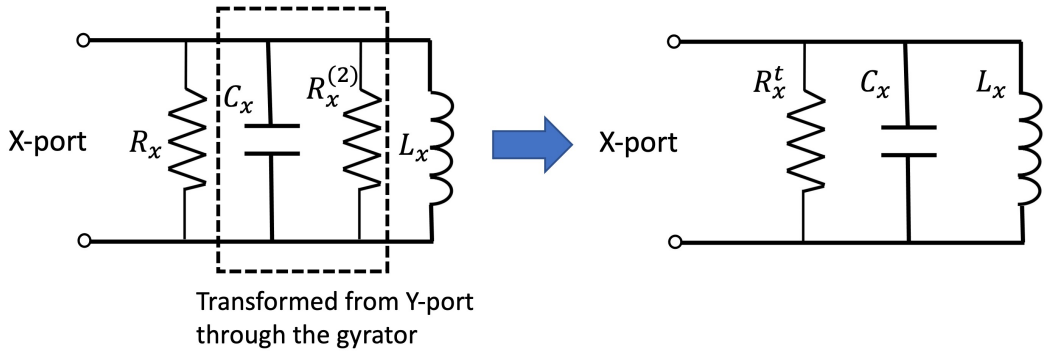

Figure 3.5: Equivalent circuit model for thin film magnetic material biased in-plane and excited only in the X-direction.

constant $\alpha \ll 1$, and the corresponding RLC values can be found.

$$\begin{cases} L_x = \mu_0 \dfrac{M_s}{H_o} \dfrac{\Delta y \Delta z}{\Delta x} \\ C_x = \dfrac{L_y \| L_{dy}}{Z_g^2} = \dfrac{1}{\mu_0 \left(\omega_m + \omega_0\right) \omega_m} \dfrac{\Delta x}{\Delta y \Delta z} \\ R_x^{(2)} = \dfrac{Q^2 Z_g^2}{R_y} \approx \mu_0 \dfrac{\omega_m \left(\omega_m + \omega_0\right)}{\alpha \omega_0} \dfrac{\Delta y \Delta z}{\Delta x} \\ R_x^t = R_x \| R_x^{(2)} = \mu_0 \dfrac{\omega_m \left(\omega_m + \omega_0\right)}{\alpha \left(2\omega_0 + \omega_m\right)} \dfrac{\Delta y \Delta z}{\Delta x} \end{cases} \tag{3.11}$$

, where Q is the quality factor of Y-port inductor, i.e., $Q = R_y/\omega \left(L_y \| L_d\right) = \left(\omega_m + \omega_0\right)/(\alpha\omega)$. Note that the resonant frequency for such RLC resonator is given by $\omega_r = \frac{1}{\sqrt{L_x C_x}} = \sqrt{\left(\omega_m + \omega_0\right)\omega_0}$, which is the same as the FMR frequency for thin-film in-plane biased ferrite.

3.2.3 Validation of Linear Equivalent Circuit Models

3.2.3.1 Stripline Resonator

For longitudinally biased microstrip or strip lines loaded with ferrite films or substrates, a complete equivalent circuit can be obtained by modifying that of the nonmagnetic microstrip or strip line. As shown in Fig. 3.6, the nonmagnetic transmission lines can be modeled by the well-known series inductor and shunt capacitor ladder circuits. Assuming that the width of the microstrip is much greater than its thickness so that a parallel plate model applies,

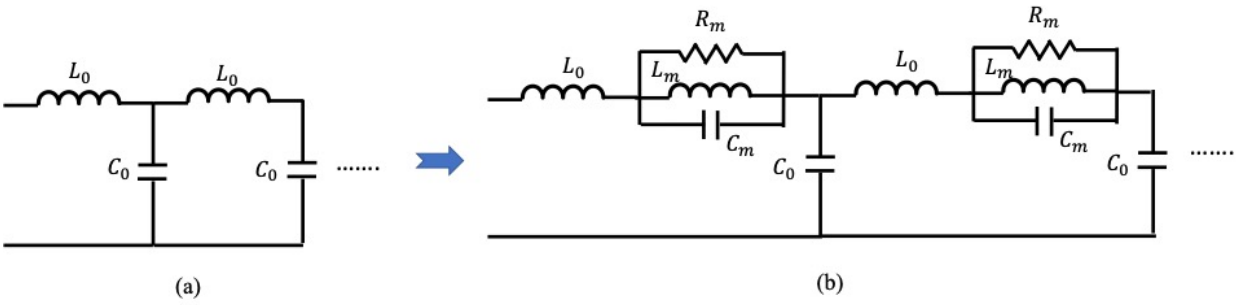

Figure 3.6: (a) LC ladder circuit equivalence of non-magnetic transmission line (b) The series L, shunt C unit cell is modified by adding a parallel RLC tank for equivalent circuit of magnetic transmission line with biased ferrite substrate

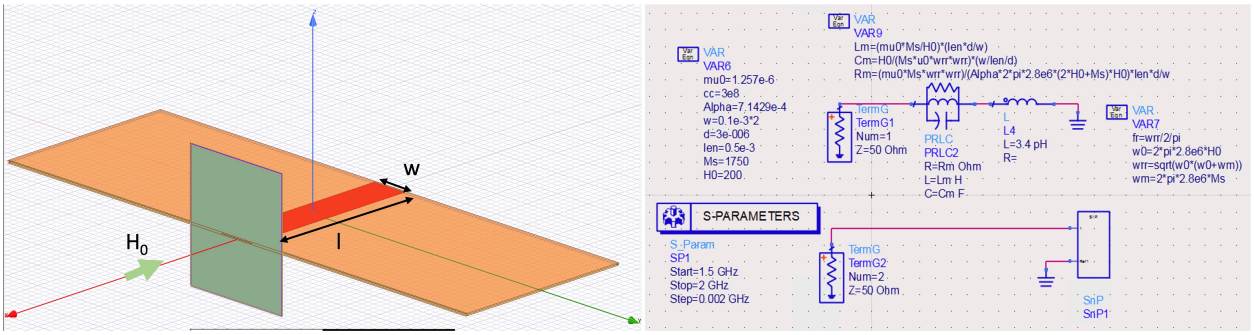

Figure 3.7: (a) A shorted circuited strip line with a width of 100um, length of 0.5mm sandwiched by two 3um thick YIG films that are longitudinally biased, simulated in HFSS. (b) ADS setup for comparison between the S-parameter derived from HFSS and the analytically derived equivalent circuit model.

the values of the LC components are given by,

$$\begin{cases} L_0 = \mu_0 \dfrac{\Delta y \Delta z}{\Delta x} \\ C_0 = \varepsilon \dfrac{\Delta x \Delta z}{\Delta y} \end{cases} \tag{3.12}$$

Assuming the magnetic field within each segment of the transmission line is uniform, and the current flowing on the strip line is longitudinal I, it is not difficult to prove that $I_x = I$. Δx,Δy, and Δz are respectively the width, thickness, and length of this segment.

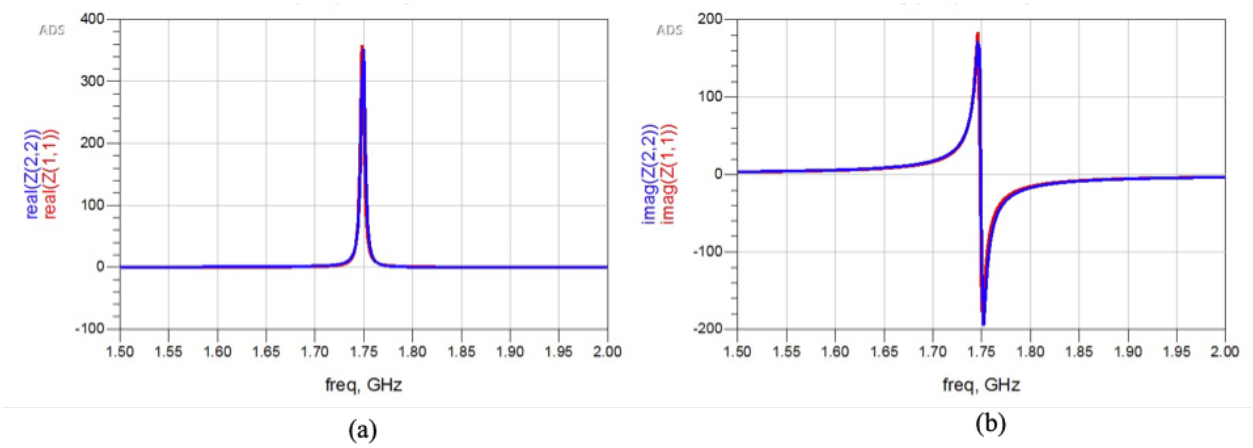

Figure 3.8: Input impedance comparison as a function of frequency between HFSS simulations (red line) and prediction of circuit model (blue line). (a) Input resistance (b) Input reactance.

Fig. 3.7 shows a stripline structure with a length l of 0.5mm and width w of 100um, sandwiched by two $d = 3um$ thick YIG films. The transmission line is short-circuited at one end and excited at the other end.

From the circuit perspective, the structure can be represented by a parallel RLC tank that represents the FMR, in series with the inductor L_o that represents the original transmission line inductance. Note that the transmission line can be represented by a single inductor when it is shorted and $l << \lambda$.

The values for the parallel RLC tank (R_m, L_m, and C_m) are rigorously derived from the equation (3.11) by substituting the physical dimensions of the structure. In other words,

$$\begin{cases} L_m = \mu_0 \dfrac{M_s}{H_o} \dfrac{ld}{(2*w)} \\ C_m = \dfrac{1}{\mu_0 (\omega_m + \omega_0) \omega_m} \dfrac{(2*w)}{ld} \\ R_m = \mu_0 \dfrac{\omega_m (\omega_m + \omega_0)}{\alpha (2\omega_0 + \omega_m)} \dfrac{ld}{(2*w)} \end{cases} \tag{3.13}$$

The reason for multiplying a factor of two for the width w in the equation (3.13) is that the magnetic field line circulates through both the top YIG layer and the bottom YIG layer,

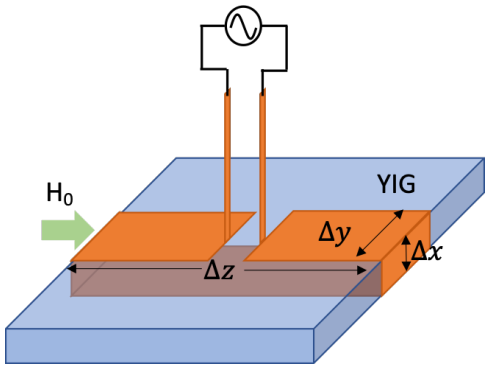

Figure 3.9: A single turn loop antenna loaded with thin film YIG biased longitudinally as shown.

making two ferrite inductors in parallel from the circuit perspective.

The structure is simulated in HFSS and its input impedance is compared to that of the RLC plus inductor model as shown in Fig. 3.8. The impedance result shows very good agreement, where the HFSS prediction is plotted against the result of the circuit model. Both the resonant frequency and its linewidth are correctly predicted by the circuit model.

3.2.3.2 Thin Film YIG loaded Electrically Small Loop Antenna

Electrically small loop antennas are among the simplest antennas. As the radiation resistance of a single-turn loop is usually small, multiple turns are often introduced to obtain an impedance that matches standard electronics. The increase of the radiation resistance through winding, however, often comes at the price of increased Ohmic resistance and parasitic capacitance. It is proposed in [73] to use the high-Q FMR of thin film YIG to increase the input impedance of a single-turn loop. The proposed antenna is a single-turn strip wrapped around a thin film YIG substrate, as shown in Fig. 3.9. The ferrite substrate is a 3.08um thick YIG film epitaxially deposited on a 500um thick GGG substrate. Its length and width are 6mm and 5mm, respectively. The conducting loop is designed to be at the same width of 6mm. A DC magnetic bias field H_0 of 36 Oersted (2865 A/m) parallel to the

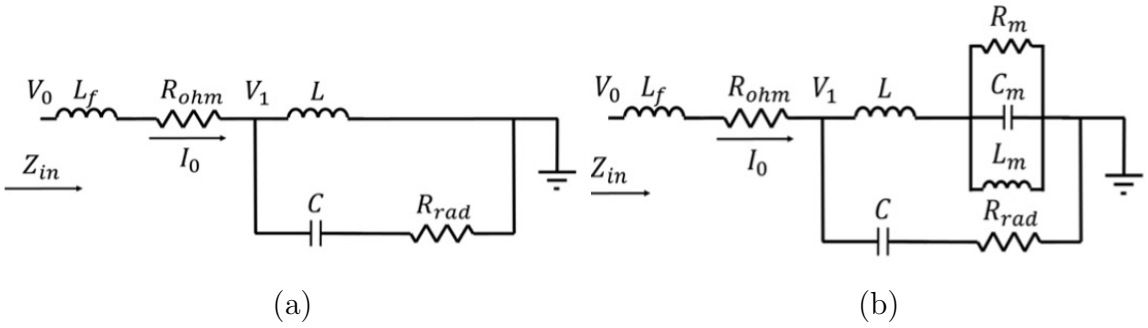

Figure 3.10: Equivalent circuit models for electrically small loops (a) without ferrite (b) with ferrite (FMR). Courtesy of [10].

current flow is assigned. The FMR-enhanced electrically small loop is designed to operate at around 0.7 GHz. What needs to be emphasized here is that this antenna is extremely small in its electrical size, with its largest physical dimension at approximately 1/60 of its operating wavelength. To better understand the role FMR played, equivalent circuit models are derived for electrically small loop antennas first without and then with the thin film ferrite. The model of the loop without ferrite is established based on the first-order (TE1) spherical wave model developed by Chu [75] so that the stored energy (parasitics) and the radiation of the lossless electrically small loop can be precisely captured.

As shown in Fig. 3.10 (a), the inductance L represents the inductive energy stored in the loop antenna. The radiation resistance R_{rad} is placed at a different branch in parallel to this inductor. An Ohmic resistance R_{ohm} is in series with the lossless circuit model to include the power dissipated on the conducting loop structure. It should be noted that in the model shown in Fig. 3.10 (a), an inductance L_f is also added in front of R_{ohm} to model the parasitic effect of the feeding lines. For the loop antenna with the loading of the thin film ferrite, similar to what is done in the previous Section, the ferrite can be represented by the insertion of a parallel RLC tank, in series with the loop inductor L as shown in Fig. 3.10(b), as the magnetic flux of the biased thin-film YIG generates an EMF in addition to that of the original air loop inductance.

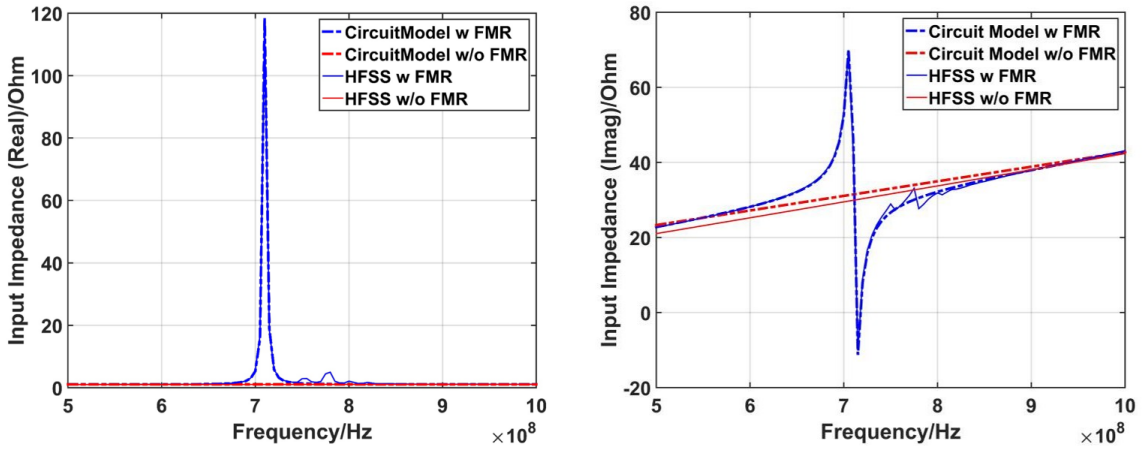

(a) (b)

Figure 3.11: Input resistance (a) and reactance (b) with and w/o FMR enhanced: HFSS vs circuit Model. Courtesy of [10]

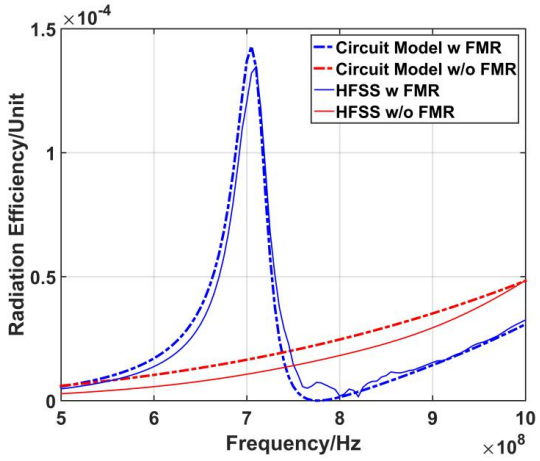

Figure 3.12: Radiation efficiency with and w/o FMR enhanced: HFSS vs Circuit Model. Courtesy of [10]

The value of RLC elements can be approximately obtained with equation (3.11) by treating the entire antenna as a cuboid ferrite cell with dimensions Δx=3.08um, Δy=6mm, and Δz=5mm as indicated in Fig. 3.9. After some optimization, the equivalent circuit model presented in Fig. 3.10(a) fits well with the full-wave simulation results of the electrically small

loop without ferrite. By just inserting the parallel RLC resonator into the circuit without altering the other parameters, the equivalent circuit model then predicts the behavior of the ferrite-loaded electrically small loop very well, which implies the parallel RLC model represents the role of the ferrite or FMR.

A comparison of the simulated input impedances between the circuit model prediction and HFSS full-wave simulations is shown in Fig.3.11. The comparison can also be extended to the prediction of radiation efficiency in Fig.3.12. Good matches between the circuit model and the full-wave simulation results for both with and without ferrite cases have been observed. The simulation results show that the input impedance rises from 1 Ohm to 118 Ohm after the loading of ferrite The radiation efficiency of the antenna has also experienced a factor of 10 increase from 0.0013% to 0.013% at the FMR frequency of 0.7GHz.

3.3 Nonlinear Equivalent Circuit Model for Spin Precession

The nonlinear equivalent circuit model for spin precession basically applies the field-to-circuit transformation to the nonlinear LLG equation rather than linearized LLG equations,

$$\frac{d\vec{M}}{dt} = -\mu_o \gamma \vec{M} \times \vec{H} + \frac{\alpha}{M_s} \vec{M} \times \frac{d\vec{M}}{dt} \tag{3.14}$$

where $\vec{M}$ is the magnetization at any point inside the ferrite, $\vec{H}$ is the internal magnetic field, α is the damping constant of ferrites, and M_s is the saturation magnetization.

Similarly, decomposing $\vec{M}$ into its three components gives

$$\vec{M} = M_x \hat{x} + M_y \hat{y} + M_z \hat{z} \tag{3.15}$$

Unlike the linear case where $M_z = M_s$ can be assumed when biased in the Z-direction, the coupling among M_x, M_y, and M_z are considered:

$$M_x^2 + {M_y}^2 + {M_z}^2 = {M_s}^2. \tag{3.16}$$

For finite dimension ferrites, the internal magnetic field $\vec{H}$ is different from the external magnetic field due to demagnetization, i.e.,

$$\begin{aligned}\vec{H} &= H_x\hat{x} + H_y\hat{y} + H_z\hat{z} \\ &= (H_{xe} - N_xM_x)\,\hat{x} + (H_{ye} - N_yM_y)\,\hat{y} + (H_{ze} - N_zM_z)\,\hat{z}.\end{aligned} \tag{3.17}$$

From Ampere's law, the currents are related to the magnetic fields by

$$I_x = H_{xe}\Delta x, I_y = H_{ye}\Delta y, I_z = H_{ze}\Delta z \tag{3.18}$$

From Faraday's law, the voltages are related to the time-changing rates of magnetic flux densities by

$$V_x = \frac{d\phi_x}{dt}, V_y = \frac{d\phi_y}{dt}, V_z = \frac{d\phi_z}{dt} \tag{3.19}$$

In addition, the magnetization is related to the magnetic flux in each direction, where Δx, Δy, and Δz are the physical dimensions of a ferrite cuboid.

$$M_x = \frac{\phi_x}{\mu_0\Delta y\Delta z}, M_y = \frac{\phi_y}{\mu_0\Delta x\Delta z}, M_z = \frac{\phi_z}{\mu_0\Delta x\Delta y} \tag{3.20}$$

Substituting (3.16) - (3.20) to (3.14), the vector LLG equation is reduced to scalar circuit equations by combining the x and y components from each side.

$$\begin{aligned}I_x &= -\frac{\Delta x\Delta y}{\mu_0\gamma\phi_z\Delta z}V_y + \frac{\Delta xH_{ze}}{\mu_0\Delta y\Delta zM_z}\int V_x dt + \frac{(N_x - N_z)\,x}{\mu_0\Delta y\Delta z}\int V_x dt \\ &\quad - \frac{\alpha\Delta x}{\gamma\mu_0^2M_s\Delta y\Delta z}\cdot\left(\frac{\phi_x}{\phi_z}\frac{d\phi_z}{dt} - V_x\right) \\ &\approx -\frac{\Delta x\Delta y}{\mu_0\gamma\phi_z\Delta z}V_y + \frac{\Delta xH_{ze}}{\mu_0\Delta y\Delta zM_z}\int V_x dt + \frac{(N_x - N_z)\,\Delta x}{\mu_0\Delta y\Delta z}\int V_x dt + \frac{\alpha\Delta x}{\gamma\mu_0^2M_s\Delta y\Delta z}V_x \\ &= -\frac{V_y}{Z_g} + \frac{\int V_x dt}{L_x} + \frac{\int V_x dt}{L_{dx}} + \frac{V_x}{R_x}\end{aligned} \tag{3.21}$$

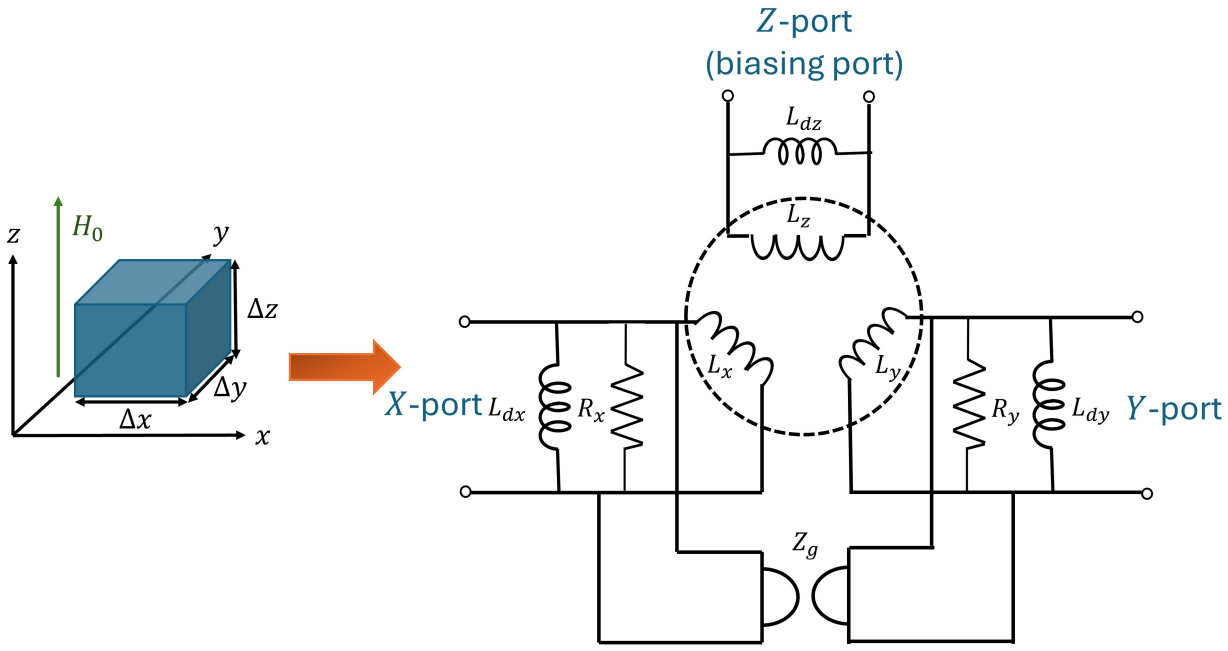

Figure 3.13: Three-port spin unit circuit model with X-port and Y-port corresponding to perpendicular pump directions, Z-port corresponding to parallel pumping direction (biasing direction).

$$
\begin{aligned}
I_y &= \frac{\Delta x \Delta y}{\mu_0 \gamma \phi_z \Delta z} V_x + \frac{\Delta y H_{ze}}{\mu_0 \Delta x \Delta z M_z} \int V_y dt + \frac{(N_y - N_z)\,\Delta y}{\mu_0 \Delta x \Delta z} \int V_y dt \\
&\quad - \frac{\alpha \Delta y}{\gamma \mu_0^2 M_s \Delta x \Delta z} \times \left(\frac{\phi_y}{\phi_z} \frac{d\phi_z}{dt} - V_y \right) \\
&\approx \frac{\Delta x \Delta y}{\mu_0 \gamma \phi_z \Delta z} V_x + \frac{\Delta y H_{ze}}{\mu_0 \Delta x \Delta z M_z} \int V_y dt + \frac{(N_y - N_z)\,\Delta y}{\mu_0 \Delta x \Delta z} \int V_y dt + \frac{\alpha \Delta y}{\gamma \mu_0^2 M_s \Delta x \Delta z} V_y \\
&= \frac{V_x}{Z_g} + \frac{\int V_y dt}{L_y} + \frac{\int V_y dt}{L_{dy}} + \frac{V_y}{R_y}
\end{aligned}
\tag{3.22}
$$

$$
I_z = \frac{\int V_z dt}{L_z} + \frac{\int V_z dt}{L_{dz}}. \tag{3.23}
$$

A three-port spin unit is constructed through field-to-circuit transformations as shown in Fig. 3.13. The currents following into each port have four contributions by virtue of the parallel circuit connection. The circuit elements values are derived as follows. Note that the

gyrator impedance Z_g and the inductances L_x, L_y, L_z are nonlinear because their values are not constants but depend on the actual current flowing through each port. On the other hand, the demagnetization inductors L_{dx}, L_{dy}, L_{dz} and loss resistors R_x, R_y are linear.

$$\begin{cases} Z_g = \mu_0^2 \gamma \dfrac{M_s I_z}{\sqrt{\left(\dfrac{I_{L_x}}{\Delta x}\right)^2 + \left(\dfrac{I_{L_y}}{\Delta y}\right)^2 + \left(\dfrac{I_z}{\Delta z}\right)^2}} \\ L_x = \mu_0 \dfrac{M_s}{\sqrt{\left(\dfrac{I_{L_x}}{\Delta x}\right)^2 + \left(\dfrac{I_{L_y}}{\Delta y}\right)^2 + \left(\dfrac{I_z}{\Delta z}\right)^2}} \dfrac{\Delta y \Delta z}{\Delta x} \\ L_y = \mu_0 \dfrac{M_s}{\sqrt{\left(\dfrac{I_{L_x}}{\Delta x}\right)^2 + \left(\dfrac{I_{L_y}}{\Delta y}\right)^2 + \left(\dfrac{I_z}{\Delta z}\right)^2}} \dfrac{\Delta x \Delta z}{\Delta y} \\ L_z = \mu_0 \dfrac{M_s}{\sqrt{\left(\dfrac{I_{L_x}}{\Delta x}\right)^2 + \left(\dfrac{I_{L_y}}{\Delta y}\right)^2 + \left(\dfrac{I_z}{\Delta z}\right)^2}} \dfrac{\Delta x \Delta y}{\Delta z} \end{cases} \tag{3.24}$$

$$\begin{cases} L_{dx} = \dfrac{\mu_0 \Delta y \Delta z}{(N_x - N_z)\,\Delta x} \\ L_{dy} = \dfrac{\mu_0 \Delta x \Delta z}{(N_y - N_z)\,\Delta y} \\ L_{dz} = \dfrac{\mu_0 \Delta x \Delta y}{N_z \Delta z} \\ R_x = \dfrac{\gamma {\mu_0}^2 M_s \Delta y \Delta z}{\alpha \Delta x} \\ R_y = \dfrac{\gamma {\mu_0}^2 M_s \Delta x \Delta z}{\alpha \Delta y} \end{cases} \tag{3.25}$$

The three-port spin unit quantifies the interaction between magnetization caused by dynamic spin precession and magnetic fields by creating a circuit equivalence. Derived from the nonlinear LLG equation, it is a general spin precession model that can be incorporated with various RF magnetic devices. Most importantly, it has the circuit elements values directly related to material properties, i.e., M_s, α, N_x, N_y,N_z, Δx, Δy, and Δz. Consequently, the spin unit is generalizable not only for different ferrite materials but also for the same ferrite material with different shape anisotropies. The reader is also encouraged to compare the

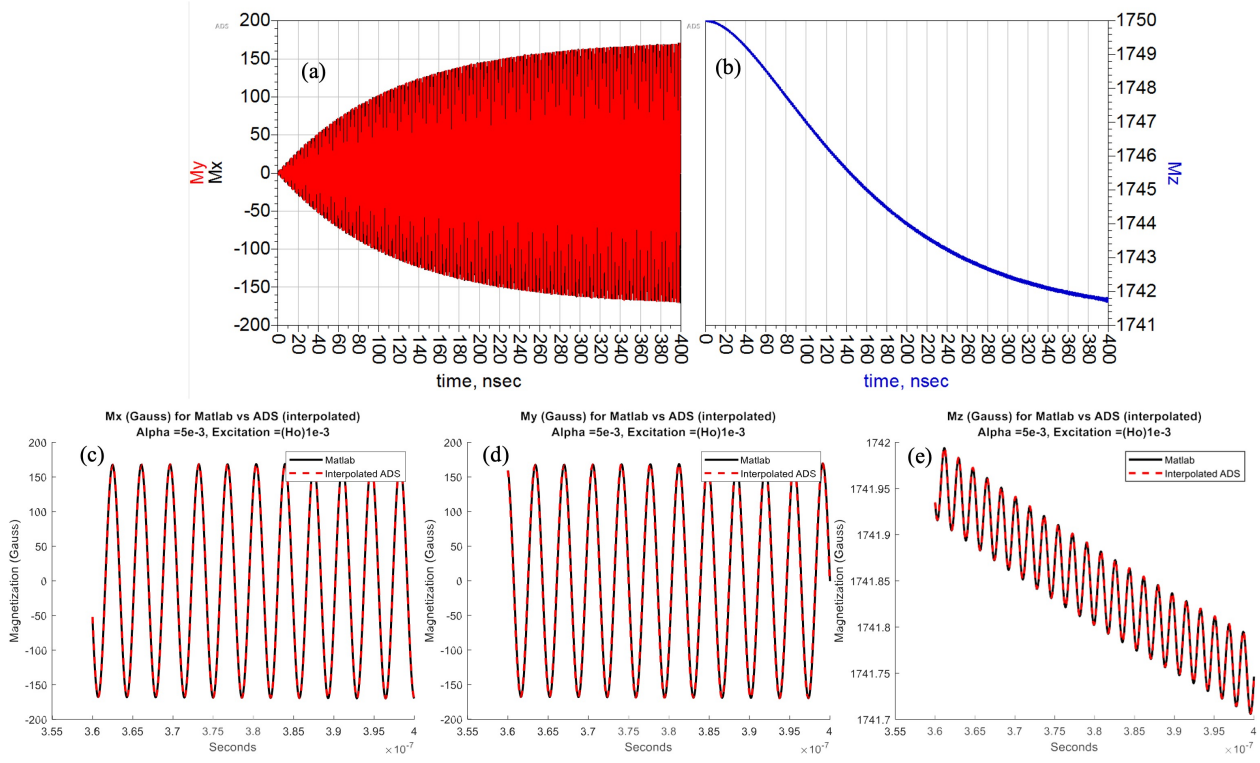

Figure 3.14: ADS simulation with the proposed circuit model for a YIG sphere in comparison with an LLG equation solver coded in MATLAB. The spherical geometry has demagnetization coefficients ($N_x = N_y = N_z = \frac{1}{3}$). (a) MATLAB-simulated trajectories of X (black) and Y (red) magnetization components vs time. (b) MATLAB-simulated trajectory of the Z-magnetization component vs time. (c),(d),(e) MATLAB (black) and ADS (red) trajectories for X, Y, and Z magnetization components respectively.

nonlinear circuit model with the linear model and verify that the nonlinear model will be reduced to the linear model under the small-signal assumption.

3.3.1 Validation of the Nonlinear Circuit Model

3.3.1.1 YIG Sphere

Two examples are used to validate the proposed circuit model. The first example assumes a YIG sphere that is magnetized in the Z-direction. The internal biasing field is set to 80 Oe (6366 A/m). An external RF field of 0.8 Oe (63.7 A/m) at the FMR frequency of 224 MHz is added in the X-axis to excite the YIG sphere, which increases the transverse magnetization and causes the reduction of the longitudinal magnetization. The simulation results are displayed in Fig. 3.14, showing that the X and Y magnetization components rise at the Larmor precession frequency of 224 MHz and reduce the longitudinal magnetization versus time. The comparison concluded that the ADS circuit model provides an accurate prediction of the large signal behavior of spin precession, which is almost identical to that of the LLG equation solver.

3.3.1.2 YIG Thin Film

The second case is a YIG thin film that is biased in one of its in-plane directions with the Y-axis pointing out of the film plane. The biasing field is applied, and the RF excitation is introduced in the same way as the first example. Due to the out-of-plane demagnetization, the precession is dominantly limited to in-plane with its X component of magnetization much greater than its Y component that oscillates at the precession frequency given by equation (2.32), which is 1.07 GHz. In addition to the magnitude reduction, the longitudinal magnetization oscillation at twice the FMR frequency is observed. The 3-port circuit model shown in Fig.3.13 is constructed by substituting $N_x = N_z = 0, N_y = 1$ to equation (3.25). Note that only L_{dy} will remain. Simulation results with both the MATLAB LLG solver and ADS circuit model display the expected trend as shown in Fig.3.15 and the agreement is again perfect. It should also be noted in Fig.3.15 that the Z component of magnetization, in addition to decaying, displays an oscillation behavior at the second harmonic of the

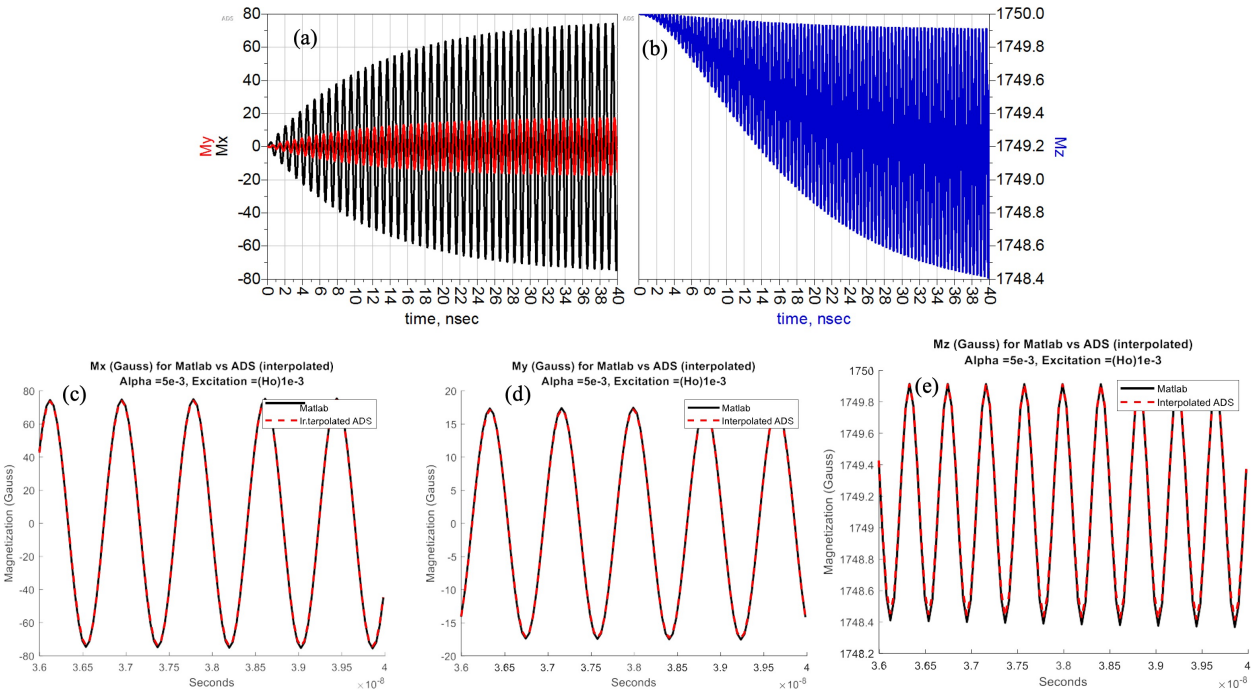

Figure 3.15: ADS simulation with the proposed circuit model for a YIG thin film in comparison with an LLG equation solver coded in MATLAB. The thin film has demagnetization coefficients ($N_x = N_z = 0,\ N_y = 1$). (a) MATLAB-simulated trajectories of X (black) and Y (red) magnetization components vs time. (b) MATLAB-simulated trajectory of Z-magnetization component vs time. (c),(d),(e). MATLAB (black) and ADS (red) trajectories for X, Y, and Z magnetization components respectively.

precession frequency. Again, this is predicted by the LLG solver and the ADS circuit model. A similar but simpler, two-port version of the equivalent circuit model for thin films was derived in [76] which describes the in-plane spin precession through analogy to the motion of a pendulum. The three-port model presented here is more complete and can be universally applied to materials with different shapes.

3.4 Circuit Model for Spin Waves

3.4.1 Magnetostatic Waves

Magnetostatic waves are approximations of electromagnetic waves within the magnetostatic limit, which applies when the scale of consideration is much shorter than the wavelength of electromagnetic waves in a non-dispersive medium. Under such an approximation, the displacement currents in Maxwell's equations are ignored. When only magnetic fields of Maxwellian origin are considered, the lossless form of the LLG equation has been expressed through the relation between $\vec{H}$ and $\vec{M}$ in the equation (2.45). Rewriting equation (2.45) to write demagnetization fields explicitly, it becomes the following,

$$\begin{bmatrix} H_x^{appl} \\ H_y^{appl} \end{bmatrix} = \frac{1}{\omega_m} \begin{bmatrix} \omega_0 & j\omega \\ -j\omega & \omega_0 \end{bmatrix} \begin{bmatrix} M_x \\ M_y \end{bmatrix} - \begin{bmatrix} H_x^{demag} \\ H_y^{demag} \end{bmatrix} \tag{3.26}$$

Considering a plane wave propagating in the Y-Z plane in an infinite biased ferrite, the demagnetization field representing the dipolar coupling is the solution of the source-less Maxwell's equations, which are approximated to be $\nabla \times \vec{H} = 0, \nabla \cdot \vec{B} = 0$. The solution is,

$$\begin{bmatrix} H_x^{demag} \\ H_y^{demag} \end{bmatrix} = \begin{bmatrix} 0 & 0 \\ 0 & -\sin^2\theta \end{bmatrix} \begin{bmatrix} M_x \\ M_y \end{bmatrix} \tag{3.27}$$

where θ is the angle between the directions of the wave propagation and the DC bias field. The magnetostatic waves are then described by,

$$\begin{bmatrix} H_x^{appl} \\ H_y^{appl} \end{bmatrix} = \frac{1}{\omega_m} \begin{bmatrix} \omega_0 & j\omega \\ -j\omega & \omega_0 + \omega_m \sin^2\theta \end{bmatrix} \begin{bmatrix} M_x \\ M_y \end{bmatrix} \tag{3.28}$$

Setting the applied magnetic field to zero, a non-trivial solution of magnetization exists only when the determinant of the matrix in equation (3.28) is zero. This yields the dispersion relation, which is called Walker's equation,

$$\omega = \left[\omega_0 \left(\omega_0 + \omega_m \sin^2\theta\right)\right]^{\frac{1}{2}}. \tag{3.29}$$

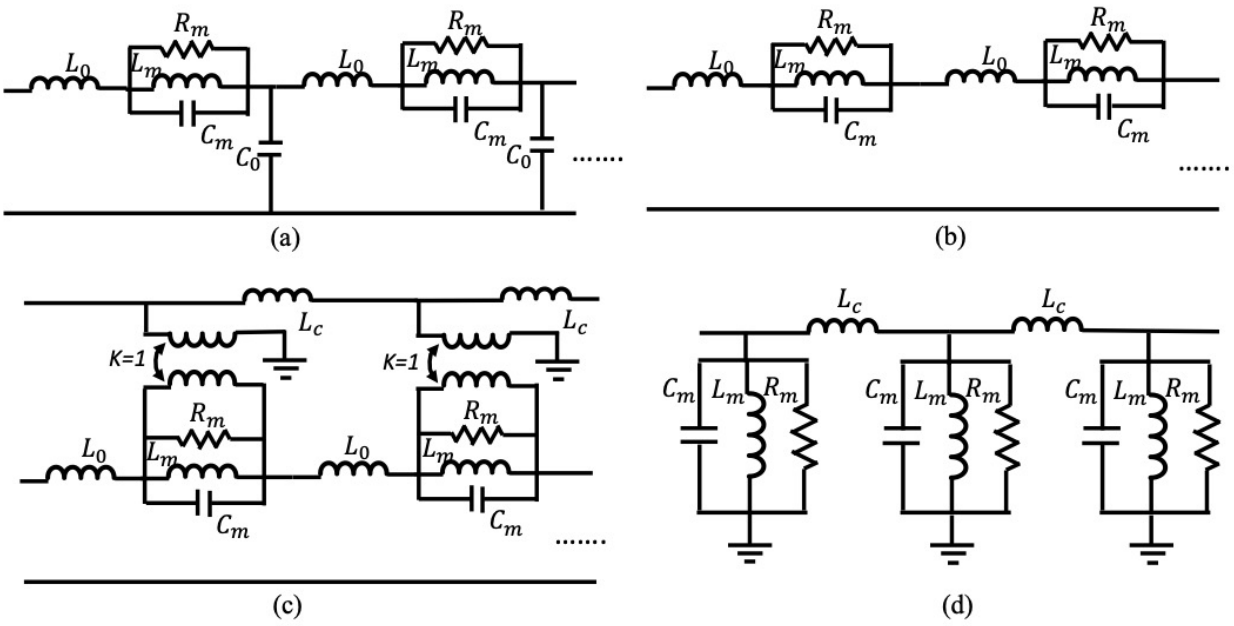

Figure 3.16: Equivalent circuits for waves traveling in an unbound, biased ferrite (a) a plane wave traveling perpendicular to the biasing direction (b) with magnetostatic wave approximation applied (c) with exchange coupling included (d) with exchange coupling included, and RLC tank transformed to shunt to ground.

If the plane wave's H-field is polarized in the X-direction and it is traveling toward the Y-axis, applying $\theta = \frac{\pi}{2}$ and assuming H_y^{appl}=0 in equation (3.28) leads to

$$H_x^{appl} = \frac{\omega_0 (\omega_m + \omega_0) - \omega^2}{\omega_m (\omega_m + \omega_0)} M_x \tag{3.30}$$

The previously derived equivalent circuit in Fig.3.5 can thus be used to represent such a plane wave as shown in Fig.3.16 (a). Applying the magnetostatic approximation means neglecting the displacement currents, i.e. the shunt capacitances in the circuit model, which results in the equivalent circuit in Fig.3.16 (b). It is evident that the resonant frequency of the structure in Fig.3.16 (b) does not depend on the phase distribution among the different unit cells, which implies a k-independent dispersion as shown by equation (3.29). This independence, however, no longer holds when spin waves with exchange coupling are considered.

3.4.2 Exchange Spin Waves

As discussed in Chapter 2, the exchange effect can be added to the dispersion relation by replacing ω_0 with $\omega_0 + \lambda_{ex}\omega_m k^2$. The dispersion relation (2.39) thus is modified to be

$$\omega = \left[\left(\omega_0 + \lambda_{ex}\omega_m k^2\right)\left(\left(\omega_0 + \lambda_{ex}\omega_m k^2\right) + \omega_m \sin^2\theta\right)\right]^{1/2} \tag{3.31}$$

When ka is small, the following relation holds:

$$1 - \cos ka \approx \frac{(ka)^2}{2} \tag{3.32}$$

Hence,

$$\omega_m \lambda_{ex} k^2 \approx 2\omega_m \lambda_{ex}(1 - \cos ka)/a^2 \tag{3.33}$$

Substituting equation (3.33) to (3.31), it becomes

$$\omega = \left(\omega_0 + \omega_m \frac{2\lambda_{ex}}{a^2}(1 - \cos(ka))\right)^{\frac{1}{2}} \left(\omega_0 + \omega_m \frac{2\lambda_{ex}}{a^2}(1 - \cos(ka)) + \omega_m \sin^2\theta\right)^{\frac{1}{2}} \tag{3.34}$$

Expanding the above equation with $\theta = \pi/2$ and ignoring the high-order terms, one yields,

$$\cos(ka) = 1 - \frac{\omega^2 - \omega_0\left(\omega_0 + \omega_m\right)}{2\omega_0 + \omega_m}\frac{a^2}{2\omega_m\lambda_{ex}} \tag{3.35}$$

It is reasonable to represent this relation by coupling inductors as shown in Fig. 3.16 (c). The value of the exchange coupling inductor can be determined by forcing the circuit model to exhibit the same dispersion relation as shown in the equation (3.35). Assuming no external RF magnetic field is applied, the voltages across the different RLC tanks are independent of each other with the exception of coupling through the transformers. Therefore, the circuit model representing the magnetization portion in Fig. 3.16 (c) is transformed into the one in Fig. 3.16 (d) where the RLC tanks are shunted to the ground. The dispersion relation can now be easily determined with the periodic structure theory using the ABCD matrix method [69], as,

$$\cos(kd) = 1 - \frac{1}{2\omega^2 L_c C_m} + \frac{L_c}{2L_m} \tag{3.36}$$

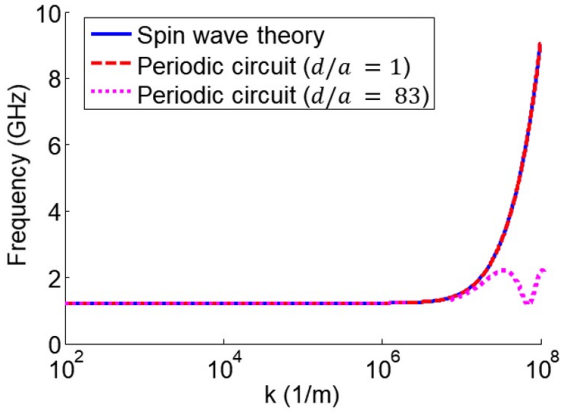

Figure 3.17: Comparison of dispersion curve calculated from spin wave theory by (3.34) to the ones calculated from the periodic circuit in Fig. 3.16 with 1.2 nm ($d/a = 1$) and 100 nm thickness ($d/a = 83$) for each unit using (3.36). Courtesy of [76].

where d is the distance between each unit, which should be set to the same value as the lattice constant a to replicate the dispersion relation in the equation (3.35). Under this condition, the expression for the coupling inductance L_c is given by,

$$L_c = \frac{d^2}{\lambda_{ex}\omega_m} \frac{\omega_0 \left(\omega_0 + \omega_m\right)}{2\omega_0 + \omega_m} L_m \tag{3.37}$$

The equivalent circuit depicted in Fig. 3.16(d) is now complete and can be used to predict the dispersive behavior of the spin wave. Similar periodic circuit models have been used to represent other types of linear or nonlinear waves [77] [78]. The dispersion relation formulated in the equation (3.36) is plotted in Fig. 3.17 and it is evident that k-independency no longer holds for high-k or short wavelength waves, where it corresponds to a frequency much higher than the ferromagnetic resonance frequency.

One practical concern is since the lattice constant a is at nanometers, modeling the entire dispersion curve with a periodic circuit model described by (3.35) and (3.36) would require $d = a$ and an overwhelmingly large number of unit cells must be used to represent a millimeter long magnetic material structure.

However, if one aims at replicating only the bottom portion of the dispersion curve, a

much coarse spatial discretization may be used as the distance resolution d determines the maximum spin wave frequency the circuit model can cover. Fig.3.17 compares the analytical spin wave dispersion relation derived from equation (3.34) to the curve derived from the periodic circuit with (3.36) on different ratios of spatial resolution d versus lattice constant a. When the spatial resolution in each resonator ($R_m L_m C_m$ parallel circuit) is close to the lattice constant (e.g., 1.2 nm), the circuit model can include high-frequency spin waves. When the thickness resolution is much coarser than the lattice constant (e.g., 100 nm), the circuit model shows a cut-off frequency without capturing the higher-frequency spin waves. Yet the lower frequency end of dispersion is still well represented. This implies that the computational complexity can be much reduced using coarser spatial discretization if only the long wavelength spin waves or those with frequencies close to the FMR are of interest.

CHAPTER 4

Modeling of Frequency-Selective Limiters (FSLs) With Physics-Based Equivalent Circuits

4.1 Introduction of Frequency-Selective Limiters (FSLs)

Power limiters are widely recognized devices that protect RF receivers from extremely high interfering signals. Traditional power limiters utilizing PIN diodes have been extensively documented in the literature [94, 95]. However, such limiters cannot discriminate the received signals at different frequencies. When a strong signal causes the limiter to turn on, all signals in the receiver are attenuated by the same amount as the strong signal. To overcome this issue, [96] proposed a nonlinear filter design consisting of a passive bandstop resonator loaded with a non-linear Schottky diode. In addition, RF-MEMS-based frequency-dependent power limiters (FDPL) were reported in [98, 100], where RF MEMS switches are combined with band-pass filters to create a power limiter that limits output RF power to specific levels based on frequency bands. The concept of using RF MEMS switches in frequency-dependent power limiter applications is based on the fact that RF MEMS switches can self-actuate under high RF power levels. The power level at which the switch actuates can be adjusted by controlling the applied DC actuation voltage.

Moreover, adaptive interference cancellation [99] techniques have also been exploited. These techniques use signal processing to identify and cancel out interfering signals, using algorithms that subtract the interference from the received signal.

Several research groups have explored the use of ferrite in power limiter applications

[24, 21, 71, 79, 23].

A thorough comparison of different limiting techniques is included below:

(1) Diode Limiters:

- Mechanism: Utilizes PIN or Schottky diodes to protect receivers from high-power signals.
- Advantages: Well-studied, effective at reducing power through nonlinear resistance changes.
- Disadvantages: Can attenuate desired signals along with unwanted ones, reducing overall sensitivity.

(2) Nonlinear Limiters:

- Mechanism: Employs nonlinear components like GaAs Schottky diodes in bandstop resonators for frequency-selective limiting.
- Advantages: Provides frequency-selective power limiting, high level of power limiting (over 30dB) with low insertion loss (<2dB).
- Disadvantages: Complex design, intermodulation distortion can occur when multiple signals are input

(3) RF-MEMS Limiters:

- Mechanism: Utilizes RF MEMS switches that self-actuate under high RF power levels, integrated with band-pass filters.
- Advantages: High linearity, low power consumption, very high isolation, and very low insertion loss. It can be made tunable by adjusting the actuation voltage.

- Disadvantages: New technology requires precise control of actuation voltage and higher complexity in design and manufacturing.

(4) Adaptive Interference Removal:

- Mechanism: Typically employs algorithms and signal processing techniques to remove or mitigate interference dynamically.
- Advantages: Flexible, can adapt to varying interference conditions, and does not rely on hardware modifications.
- Disadvantages: Requires computational resources, introduces processing delays, may not be applicable in real-time systems, and effectiveness depends on the accuracy of the interference model.

(5) Ferrite-Based Limiters:

- Mechanism: Uses the nonlinear properties of magnetic spin waves in magnetized ferrites (e.g., YIG) to dissipate high-power signals.
- Advantages: Can achieve high power dissipation at specific frequencies; provides linear and low-loss response at low power levels; short time delay on a range of microseconds to attenuate high-power signals; easy implementation.
- Disadvantages: Bulkier compared to diode and MEMS-based solutions.

In fact, most microwave FSLs are built with magnetic materials that have intrinsic nonlinearities. One candidate for such magnetic material is the yttrium iron garnet (YIG) [66]. A typical FSL device is illustrated in Fig. 4.1 (a), where a YIG thin film is grown on a gadolinium gallium garnet (GGG) substrate under the coplanar waveguides (CPW). The external static magnetic field is applied in the plane of the YIG film and parallel to the RF magnetic field created by the CPW.

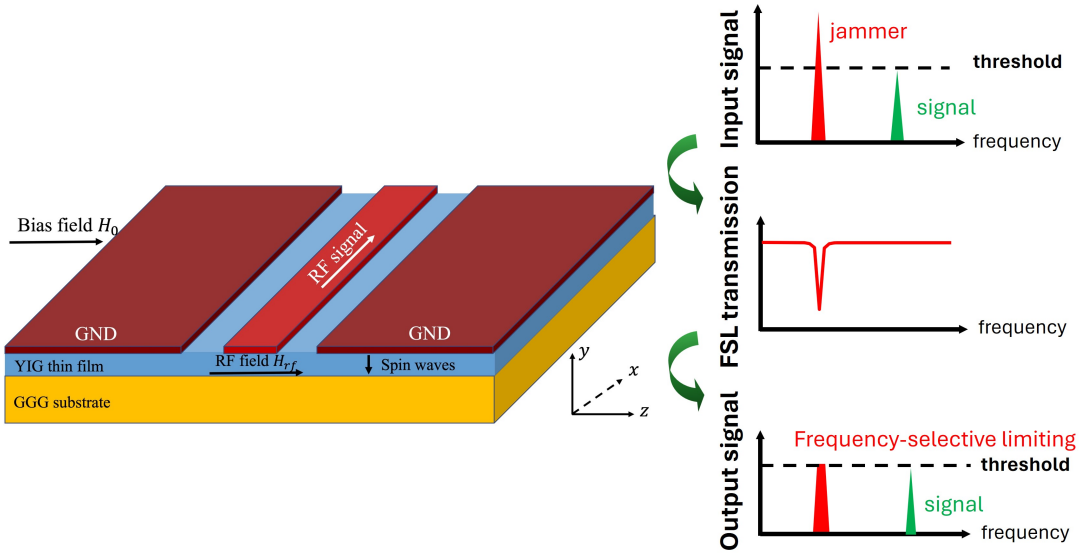

(a) (b)

Figure 4.1: (a) Schematic of a CPW-FSL with the bias field parallel to the RF field. (b) Input signal spectrum and output signal spectrum when two-tone signals pass through the FSL. One jammer has a power greater than the FSL threshold, while the signal power is below the FSL threshold.

The power spectrum of a typical FSL is shown in Fig. 4.1 (b). When a small signal of interest goes through the FSL with a large-signal interferer, the FSL attenuates only the large signals above its threshold while letting the weak, useful signal pass without attenuation.

Despite the fact that ferrite-based FSLs have been commercially available for a long time, the modeling of such devices remains challenging due to the complex nature of ferrite materials. The underlying principles for FSLs include 1) dynamic spin precession; 2) spin wave propagation; 3) coupling between electromagnetic (EM) waves and spin waves; and 4) field nonuniformity. The explanations for each operation mechanism are summarized as follows:

1. *Dynamic spin precession*: The magnetic properties of ferrites are attributed to the magnetic moments generated by spinning electrons. Under external magnetic fields, the

magnetic moments will exhibit precessional motion. Such interaction is governed by the Landau-Lifshitz-Gilbert (LLG) equation[56]. In addition, the natural spin precession frequency, i.e., ferromagnetic resonance (FMR) frequency f_r, determines the operation frequency for magnetic devices.

2. *Spin wave propagation*: the power-limiting effect of FSLs is caused by the excitation of spin waves at $f/2$, which carries away the EM wave power at f[83, 84]. The lowest operation frequency for FSLs is $2f_r$, where f_r is the FMR frequency. However, FSLs also attenuate high-power signals above $2f_r$. Such broadband behavior originates from the dispersive nature of spin waves [74].

3. *Coupling between electromagnetic (EM) waves and spin waves*: Spin waves are generated when EM waves propagate in the longitudinal direction. The power is transferred to lattice vibrations and eventually lost in heat[85]. Such coupling is nonlinear as only a high-power RF signal generates spin waves, while a low-power RF signal passes the transmission line unaffected by the ferrite [86, 87].

4. *Field nonuniformity*: the RF magnetic field provided by a CPW is spatially nonuniform[88]. Specifically, the magnetic fields near the corner of the conductor are much stronger than those at the center. Hence, in CPW-FSLs, the spin waves near the corner are excited earlier. CPW structures have been used to excite higher-order spin wave modes by virtue of such nonuniformity in magnetic filters[89]. For FSLs, the field nonuniformity will affect their power threshold and insertion loss.

These intrinsic operation mechanisms can be used to explain the behaviors of FSLs qualitatively, but building theoretical models for FSLs has been challenging due to the complex nature of magnetic materials. Full wave simulators such as Ansys HFSS solve Maxwell's equations for magnetic materials in linear regime [50]. However, they do not incorporate the nonlinear property of magnetic materials that contributes to the power-limiting effect of FSLs. The models based on micromagnetics, on the other hand, solve

the nonlinear LLG equation. However, they are only suitable for smaller device dimensions in μm scale [90, 91]. Recently, behavioral modeling of FSLs was proposed, which treated FSLs as general nonlinear systems with memories and used mathematical models to predict their performance [92]. The mathematical model achieved good accuracy with moderate computation complexity, yet the physics of FSLs was obscured, and therefore, the model is not generalizable.

4.2 Modeling Procedure of FSLs

4.2.1 Modeling Dynamic Spin Precession

Since FSLs utilize the nonlinearity of ferrite materials, the nonlinear equivalent circuit, as shown in Fig. 3.13 for spin precession, has to be constructed. The physical discretization, i.e., Δx, Δy, and Δz, depends on the device's field profile. In other words, we want to discretize the ferrite materials such that the magnetic field can be considered uniform inside a ferrite cuboid. The detailed discretization mechanism is delineated in the following sections.

4.2.2 Modeling Spin Wave Propagation

Exchange spin waves are oscillations of magnetization within magnetic materials caused by exchange coupling that has a quantum mechanics origin[74]. Fig. 4.2 illustrates its propagation with M_x changing along the thickness direction. The thickness d is divided into multiple (N_d) Δd, with each $w \times l \times \Delta d$ ferrite cuboid represented by a single three-port spin unit. Exchange coupling is represented by an inductor L_c added between the X-ports of adjacent spin units, whose value is given by combining (3.13) and (3.37):

$$L_c = \frac{l\Delta d^3}{w} \frac{\mu_0 \left(\omega_0 + \omega_m\right)}{\lambda_{ex} \left(2\omega_0 + \omega_m\right)}, \tag{4.1}$$

where $\omega_0 = 2\pi \times 2.8 \times 10^6 \times H_0$, $\omega_m = 2\pi \times 2.8 \times 10^6 \times M_s$, and $\lambda_{ex} = 3 \times 10^{-16} m^2$ for YIG.

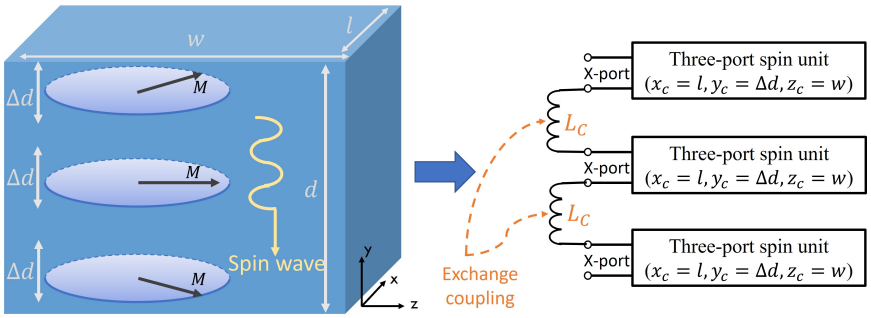

Figure 4.2: Illustration of spin wave propagation along the thickness direction and the corresponding circuit model with inductor L_c added between three-port spin units.

4.2.3 Modeling the Coupling Between EM Waves and Spin Waves

As discussed in the previous section, a three-port spin unit quantifies dynamic spin precession in three dimensions. Later on, these circuit equivalence can be incorporated with external circuitry to form a complete circuit for RF magnetic devices. Note that during the previous derivation, the bias magnetic field is assumed to be in the z direction. Hence, if the RF magnetic field lies in the z direction as well, i.e., parallel pumping, Z-port should be connected to the external circuitry. On the other hand, if the RF magnetic field lies in x or y directions, i.e., perpendicular pumping, the corresponding X-port or Y-port should be connected to the external circuitry. The former is the ideal situation for FSLs, as shown in Fig. 4.1, with the RF field in the same direction as the bias field. However, in practical FSL devices, the bias field may have a small angle with respect to the z direction due to form factor constraints. As a result, the thin ferrite film will also be partially perpendicularly pumped. Hence, both cases will be discussed in this section.

4.2.3.1 Parallel Pumping

In Fig. 4.1, the electric field only has a y component, and the magnetic field only has a z component under the quasi-TEM approximation[69]. During propagation, the EM wave

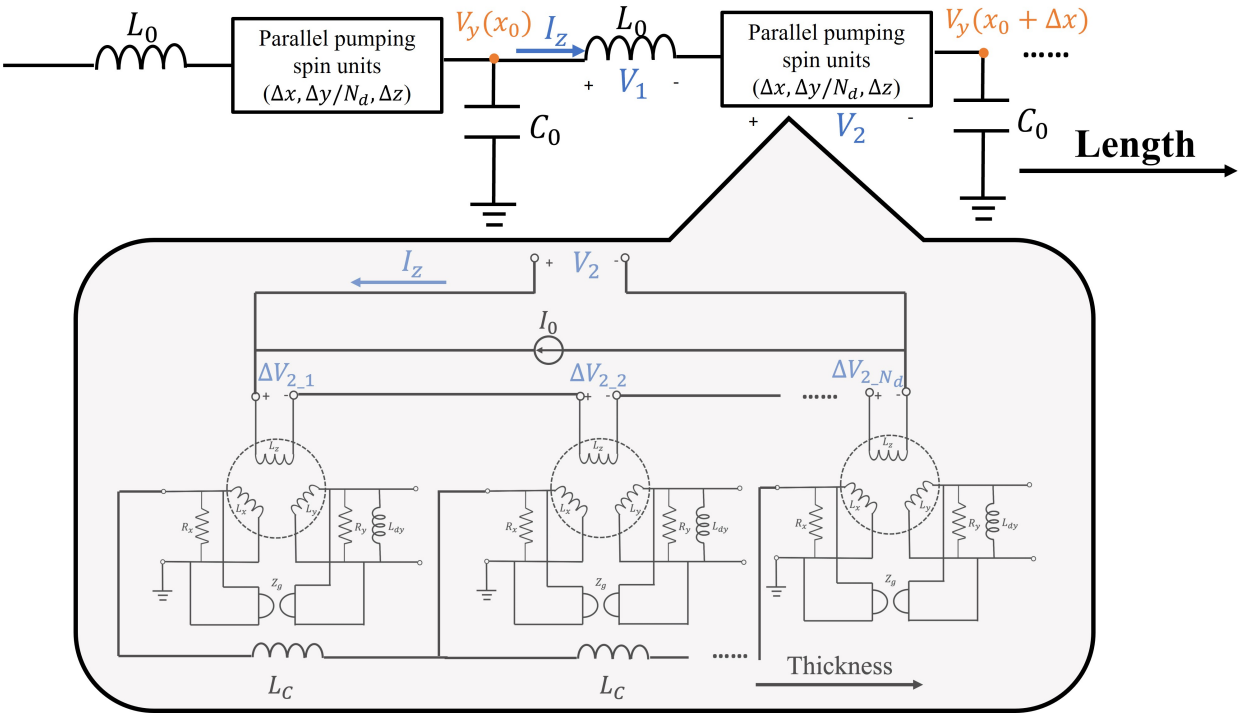

Figure 4.3: Equivalent circuit for parallel pumping with N_d spin units cascaded with one transmission line inductor.

couples to the spin wave through Z-ports of three-port spin units, as shown in Fig. 4.3. Considering exchange spin wave propagation along the thickness, there are N_d spin units within one parallel pumping section. Hence, the total voltage drop V_2 is the summation of voltage drop at the individual spin unit, i.e., ΔV_{2_i}. $V_y(x_0)$ and $V_y(x_0+\Delta x)$ are the voltages at two adjacent nodes when the EM wave travels along x direction from x_0 to $x_0+\Delta x$. I_z is the current flowing through the center conductor. L_0 and C_0 are the inductance and capacitance of the transmission line. Their values are given by $C_0 = \varepsilon \frac{\Delta z \Delta x}{\Delta y}$ and $L_0 = \mu_0 \frac{\Delta y \Delta x}{\Delta z}$.

Kirchhoff's circuit laws can be verified through Maxwell's equations:

$$-\frac{\partial H_z}{\partial x} = \varepsilon \frac{\partial E_y}{\partial t} \tag{4.2}$$

$$\frac{\partial E_y}{\partial x} = -\frac{\partial B_z}{\partial t} \tag{4.3}$$

$$B_z = \mu_0 \left(H_z + M_z\right). \tag{4.4}$$

Applying field-to-circuit transformations $E_y = -\frac{V_y}{\Delta y}$, $H_z = \frac{I_z}{\Delta z}$, (**??**) and (4.4) become:

$$\frac{\partial I_z}{\partial x} = \varepsilon \frac{\Delta z}{\Delta y} \frac{\partial V_y}{\partial t} \tag{4.5}$$

$$\mu_0 \left(\frac{\partial H_z}{\partial t} + \frac{\partial M_z}{\partial t} \right) = \frac{1}{\Delta y} \frac{\partial V_y}{\partial x}. \tag{4.6}$$

Equation (4.5) satisfies Kirchhoff's current law (KCL) at the node $V_y(x_0 + \Delta x)$. On the other hand, (4.6) satisfies Kirchhoff's voltage law (KVL) because the voltage drop at the spin unit is caused by time-changing magnetic flux in z direction:

$$V_2 = \sum_{i=1}^{N_d} \Delta V_{2\_i} = \sum_{i=1}^{N_d} \frac{d\phi_{z\_i}}{dt} \tag{4.7}$$

$$M_z = \frac{\phi_z}{\mu_0 \Delta x \Delta y} = \frac{\sum_{i=1}^{N_d} \phi_{z-i}}{\mu_0 \Delta x \Delta y} \tag{4.8}$$

$$V_1 = L \frac{\partial I_z}{\partial t}. \tag{4.9}$$

Substituting (4.7), (4.8) and (4.9) into (4.6) and multiplying both sides by $x_c y_c$, it becomes

$$V_1 + V_2 = V_y(x_0 + x_c) - V_y(x_0), \tag{4.10}$$

which is exactly KVL.

Hence, the loading of thin-film ferrite can be represented by cascading spin units with transmission line inductors. When the RF power is low, the RF signal should be able to pass through the device unaffected by the spin units because the excitation of spin waves only happens at high power levels. Using the circuit diagram in Fig. 4.3, low RF power corresponds to a small RF magnetic field, i.e., small I_z. In this case, the magnetic moments in the ferrites are saturated by the bias magnetic field in the z direction as well. As a result, $M \approx M_z \approx M_s$ is a constant. Hence, the $\frac{\partial M_z}{\partial t}$ term in (4.6) will become zero, causing V_2 to be zero. As a result, the equivalent circuit reduces to the transmission line lumped-element

model because the spin units are short-circuited. In this case, the EM waves will not couple with spin waves, as expected. When the RF power becomes larger, the spin wave oscillation fueled by the RF field results in a large change in M_z, which will induce a voltage drop in the transmission line, and the EM wave power will be lost in the FSL device.

4.2.3.2 Perpendicular Pumping

As discussed before, FSLs should operate under parallel pumping conditions. However, in practice, the bias magnetic field may have a small angle θ with the RF magnetic field due to the requirement of form factors. As a result, if we decompose the RF magnetic field, there will be an effective RF field perpendicular to the bias field, whose value is $H_{rf}\sin\theta$. The schematic of perpendicular pumping is illustrated in Fig. 4.4.

From the FSL measurement, this perpendicular component of pumping does not affect the FSL nonlinearity but just contributes to the out-of-band FMR absorption. As a result, it's convenient to simplify the nonlinear three-port spin unit in its linear case, which becomes a parallel RLC resonator with values given in (3.11):

$$\begin{cases} L_x = \mu_0 \dfrac{M_s}{H_o}\dfrac{\Delta y \Delta z}{\Delta x} \\ C_x = \dfrac{1}{\mu_0\left(\omega_m+\omega_0\right)\omega_m}\dfrac{\Delta x}{\Delta y \Delta \mathrm{z}} \\ R_x = \mu_0 \dfrac{\omega_m\left(\omega_m+\omega_0\right)}{\alpha\left(2\omega_0+\omega_m\right)}\dfrac{\Delta y \Delta z}{\Delta x}. \end{cases} \tag{4.11}$$

Note that the resonant frequency for such RLC resonator is given by $\omega_r = \frac{1}{\sqrt{L_x C_x}} = \sqrt{\left(\omega_m+\omega_0\right)\omega_0}$, which is also the FMR frequency for a thin-film in-plane biased ferrite. In addition, the physical meanings for Δx, Δy, and Δz differ from those of parallel pumping cases. For example, from Fig. 4.1, Δx lies along the length direction while Δz lies in the width direction for the CPW-FSL. However, in Fig. 4.4, Δx lies in the width direction while Δz lies in the length direction. Hence, these different physical scalings must be handled during simulations.

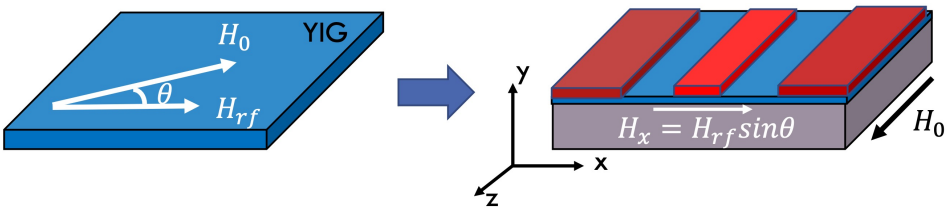

Figure 4.4: Schematic of a thin-film ferrite with a non-zero bias angle, causing perpendicular pumping with effective RF magnetic field in x direction and bias field in z direction

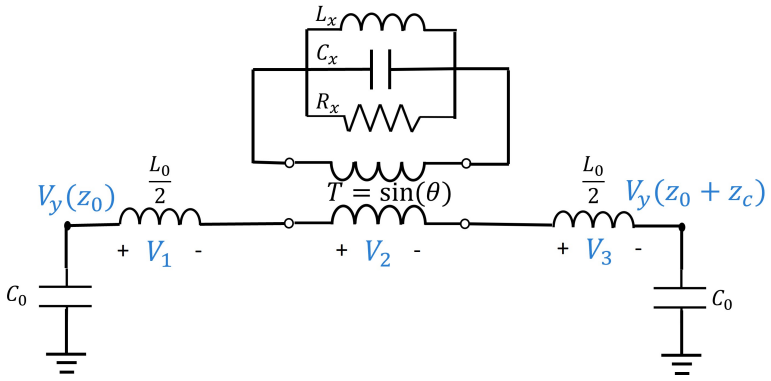

Figure 4.5: Equivalent circuit model for perpendicular pumped thin-film ferrite.

Similar to the parallel pumping case, the RLC resonator is connected to the transmission line lumped-element model to represent the loading of ferrite, as shown in Fig. 4.5. The transformer T is used to quantify the effect of perpendicular pumping by setting $T = \sin(\theta)$, where θ is the angle between the RF field and the bias field. When $\theta = 90°$, the entire RLC resonator is coupled to the transmission line, representing pure perpendicular pumping. On the other hand, when $\theta = 0°$, the RLC resonator does not affect external circuitry.

Kirchhoff circuit laws can also be verified through Maxwell's equations and are given below. From Fig. 4.4, the effective magnetic field lies in x direction and the electric field lies in y direction. Hence,

$$-\frac{\partial H_x}{\partial z} = \varepsilon \frac{\partial E_y}{\partial t} \tag{4.12}$$

$$\frac{\partial E_y}{\partial z} = -\frac{\partial B_x}{\partial t}. \tag{4.13}$$

Applying field-to-circuit transformations, (4.12) and (4.13) become the following:

$$\frac{\partial I_x}{\partial z} = \varepsilon \frac{\Delta x}{\Delta y} \frac{\partial V_y}{\partial t} \tag{4.14}$$

$$\frac{1}{\Delta y} \frac{\partial V_y}{\partial z} = \frac{\mu_0}{\Delta x} \frac{\partial I_x}{\partial t} + \frac{1}{\Delta y \Delta z} V_2. \tag{4.15}$$

By inspection, (4.14) satisfies Kirchhoff's current law (KCL) by setting the transmission line capacitance $C_0 = \varepsilon \frac{\Delta x \Delta z}{\Delta y}$. Equation (4.15) satisfies Kirchhoff's voltage law (KVL) using the definition of TL inductance $V_1 + V_3 = L_0 \frac{\partial I_x}{\partial t} = \mu_0 \frac{\Delta y \Delta z}{\Delta x} \frac{\partial I_x}{\partial t}$.

After substituting and multiplying both sides by $\Delta y \Delta z$, (4.15) becomes

$$V_1 + V_2 + V_3 = V_y\left(z_0 + \Delta z\right) - V_y\left(z_0\right), \tag{4.16}$$

which satisfies KVL.

4.2.4 Modeling Field Nonuniformity

The field distribution of a CPW line is spatially non-uniform. Such nonuniformity can be visualized and quantified by examining the magnitude of magnetic fields throughout the cross-section of a CPW line. As shown in Fig. 4.7 (a), a CPW line is on top of a YIG thin film buffer. Note that the YIG buffers have the same electric properties and physical dimensions as YIG thin films, which represents the fact that these regions will later be occupied by YIG to build an FSL. From this schematic plot, the magnetic field is nonuniform both in the conductor width direction and in the substrate thickness direction. In the width direction, the magnetic field is concentrated near the edges of the center conductor. In the thickness direction, the magnetic field becomes smaller as the thickness goes deeper.

Such nonuniformity can be quantified by generating the z components of the magnetic fields, i.e., $mag(H_z)$ from HFSS. Fig. 4.6 plots the strengths of H_z when the observation points are near the center conductor (in blue) and farther away from the center conductor

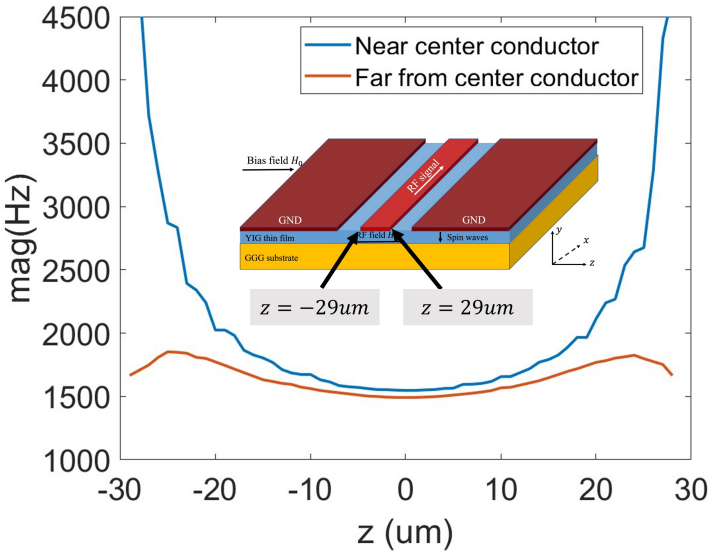

Figure 4.6: Strength of the magnetic field along the z direction when the observation points are near the center conductor (in blue) and farther away from the center conductor (in orange).

(in orange). The width of the center conductor is 58 um, and we can clearly identify a much larger magnetic field strength near the edges of the center conductor, i.e., $z \pm 29um$.

The nonuniformity will affect the performance of FSLs when the CPW line is loaded with thin-film YIG. This is because electron spins at different locations will experience different magnetic fields. For example, the electron spins near the edges of the center conductor will receive much larger RF field perturbation, so the spin waves in that region will be excited earlier compared with other regions. Hence, to predict the performance of CPW-FSLs precisely, such nonuniformity has to be considered.

This section addresses the two-dimensional nonuniformity by dividing the substrate region and creating an inductor array associated with it. As shown in Fig. 4.7, the substrate under the center conductor is divided into six sub-regions. Within each region, the magnetic field H and magnetic flux ϕ are assumed to be uniform. The equivalent circuit for such division is illustrated in Fig. 4.7 (b)$\sim$(d). Originally, the CPW line inductance is a single

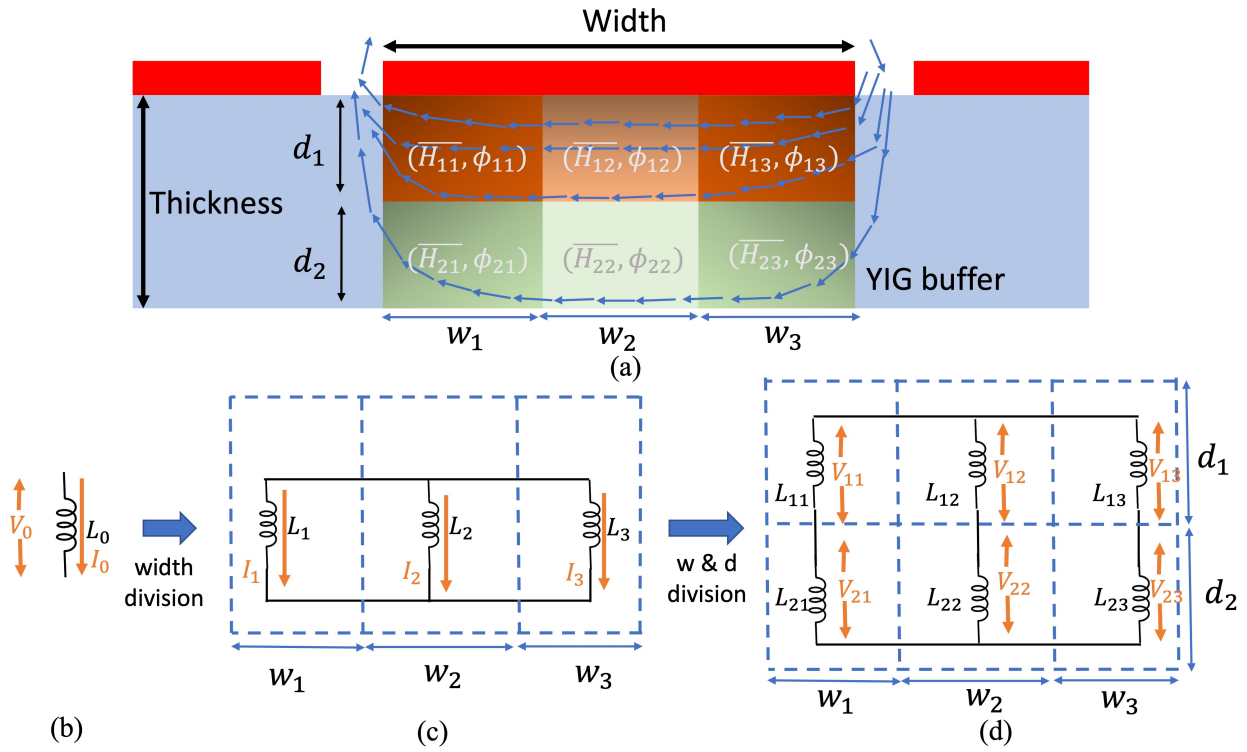

Figure 4.7: Schematic of the magnetic field distribution at the cross-section of the CPW line, The substrates are divided into six regions. Within each region, the magnetic field and magnetic flux are assumed to be uniform. (b) Equivalent circuit for transmission line inductance when only width division is considered, and width + thickness division is considered.

L_0. Assume the current flowing through it is I_0, and the voltage change across it is V_0. Later on, we divide the substrate region along the width direction, and three inductors are introduced, each corresponding to one sub-region. According to Ampere's law,

$$I_j = H_{1j} \times w_j, j = 1, 2, 3. \tag{4.17}$$

Hence, these three inductors L_1, L_2, and L_3 will have different current flows because the H field values are different. As a result, they are connected in parallel. Then, on top of the width division, we apply thickness division so that six inductors are introduced in total. Suppose the voltage drops at inductors L_{11} and L_{21} are V_{11} and V_{21}. According to Faraday's

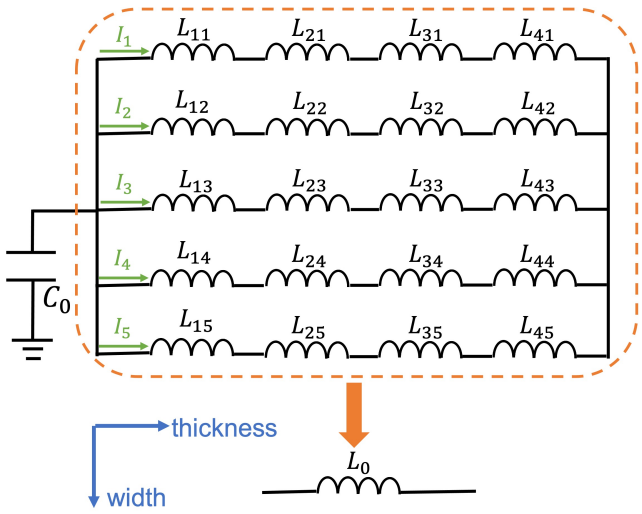

Figure 4.8: Complete circuit model for the 5*4 inductors array.

law,

$$V_0 = V_{11} + V_{21} = \frac{d\left(\phi_{11} + \phi_{21}\right)}{dt} = \frac{d\phi_{11}}{dt} + \frac{d\phi_{21}}{dt}. \tag{4.18}$$

Consequently, L_{11} and L_{21} should be connected in series because their voltage drops add together to form the total voltage drop from the center conductor to the ground. As a result, an inductor array is formed. The detailed steps to calculate individual inductor values are listed in the following section.

4.2.4.1 Calculate Average H-field $\bar{H_{ij}}$ in Each Physical Region

The definition of inductance is the magnetic flux linkage versus the current. Since the magnetic flux is linearly proportional to the magnetic field, different magnetic fields correspond to different inductors. In Fig. 4.7, six divisions are illustrated for better visualization. The actual realization, however, used 40 physical divisions, with 10 in width and four in thickness. Since the magnetic field is symmetric along the width direction (the field at the left corner is the same as the field at the right corner), 10 physical width divisions can be merged by pairs to create a five-by-four inductor array, as shown in Fig. 4.8. Within each region, average H-field $\bar{H_{ij}}$ is calculated from the HFSS simulation, where $i = 1, 2, \ldots, 4$ is the thickness

division index and $j = 1, 2, \ldots, 5$ is the width division index.

4.2.4.2 Calculate Current Flow I_i in Each Branch

According to Ampere's law, $I = \int \vec{H} \cdot d\vec{l}$. Under the quasi-TEM approximation, the RF magnetic field created by the CPW line is parallel to the conductor width direction, so $\vec{H}$ and $d\vec{l}$ are in the same direction. Hence, different widths and different magnetic fields will multiply together to create different currents flowing through the center conductor, i.e., I_1, I_2, and I_3 in Fig. 4.7. When there are five divisions along the width, the corresponding currents can be calculated using

$$I_j = H_{1j} \times w_j, j = 1, 2, \ldots, 5, \tag{4.19}$$

where H_{1j} is the magnetic field below the center conductor.

4.2.4.3 Calculate Inductors' Ratios for Width Divisions

As discussed earlier, inductors divided along the width should be connected in parallel. For parallel-connected inductors, the current flows are inversely proportional to the inductances:

$$\frac{I_m}{I_n} = \frac{\sum_i L_{in}}{\sum_i L_{im}}, \tag{4.20}$$

where i is the index for thickness divisions.

4.2.4.4 Calculate Inductors' Ratios for Thickness Divisions

Contrary to the width division, inductors divided along the thickness should be connected in series with the ratios determined by the magnetic-flux ratios:

$$\frac{L_{mj}}{L_{nj}} = \frac{\phi_{mj}}{\phi_{nj}} = \frac{\overline{H_{mj}} \times d_m}{\overline{H_{nj}} \times d_n}, \tag{4.21}$$

where j is the index for width divisions, d_m and d_n are the thickness for different divisions, $\overline{H_{mj}}$ and $\overline{H_{nj}}$ are average H fields magnitude in sub-regions.

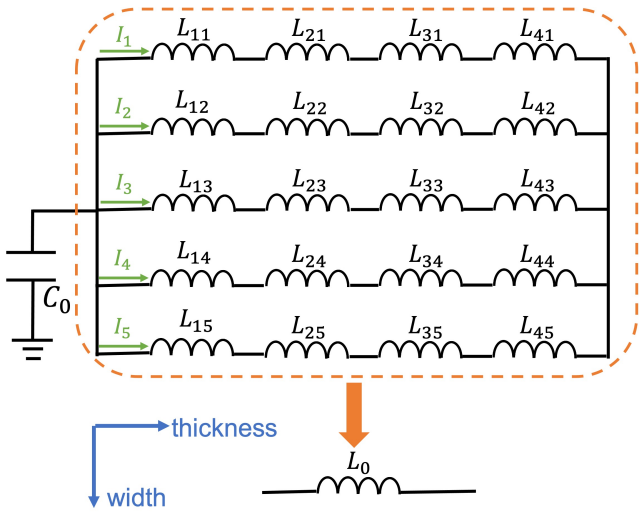

Figure 4.9: Complete circuit model for the 5*4 inductors array.

4.2.4.5 Calculate Individual Inductances

Having obtained the inductances' ratios both in the width direction and the thickness direction, we can calculate their values using the fact that the total inductance should recover the original CPW line inductance L_0, as shown in Fig. 4.8. The individual inductances are listed in the following section.

4.2.4.6 Insert Parallel Pumping and Perpendicular Pumping Spin Units

As discussed in section 5.2.3, the interaction between ferrites and transmission lines can be modeled by cascading three-port spin units with transmission line inductors. When the CPW line inductor is divided into a two-dimensional array, such cascading can be performed element-wise, as depicted in Fig. 4.10. Because both parallel pumping and perpendicular pumping can happen in CPW-FSLs, parallel pumping spin units and perpendicular pumping RLC resonators are cascaded with sub-inductors. For each spin unit, its length (Δx), width (Δz), and thickness (Δy) are specified according to the physical divisions,i.e., $\Delta x = \Delta l$ and $\Delta y = \Delta d$.

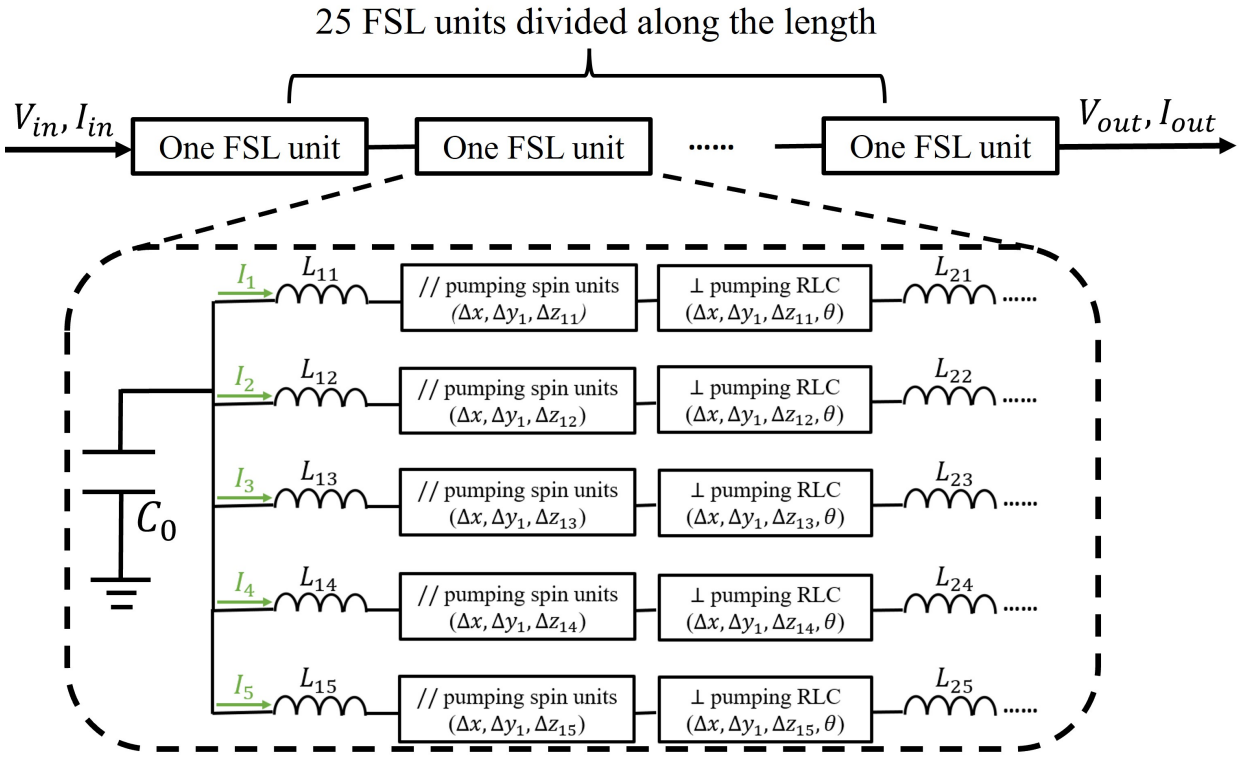

Figure 4.10: Complete circuit model for the inductors array with spin units. For linear S-parameters simulation, the nonlinear spin units are replaced by linear RLC resonators described in Fig. 4.5.

What needs special attention is that the widths of the spin units should not be equal to the physical widths, i.e., w_1, w_2,... w_5. Instead, we should assign 'effective widths' that reflect the magnetic field information in that region. According to (4.19), the effective width of the magnetic field line is larger, further away from the center conductor because the field is smaller. With a uniquely defined current, the effective width can be calculated using

$$z_c(ij) = \frac{I_j}{H_{ij}}. \tag{4.22}$$

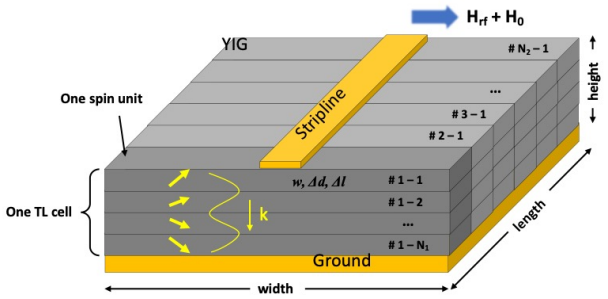

Figure 4.11: Stripline FSL device structure that shows spin wave oscillations launched along the thickness direction under the excitation of the RF wave traveling in the transmission line. Courtesy of [76].

4.3 Model Validation

This section confirms the proposed circuit models with measurements from commercially available stripline FSL [76] and CPW-FSL [93]. For stripline FSL, the magnetic field distribution can be assumed to be uniform at the device's cross-section. Hence, field nonuniformity is not a major concern, so the model is simplified. For CPW-FSL, on the other hand, a complete model with field nonuniformity has to be used to achieve a good agreement between simulation and measurements.

4.3.1 Stripline FSL

The bottom half of a stripline FSL structure is illustrated in Fig. 4.11, which shows an RF wave traveling toward the longitudinal direction excites spin wave oscillations along the thickness of the YIG substrate. Fig.4.11 also shows a possible discretization strategy for modeling, which divides the transmission line into multiple segments in its longitudinal direction. For each segment, the current passing through the stripline feeds the RF energy to the oscillation of the spin waves along the thickness direction through the nonlinear spin precession model presented in Chapter 3, while the propagation of the spin waves between the two thickness boundaries can be represented by the spin wave equivalent circuit in

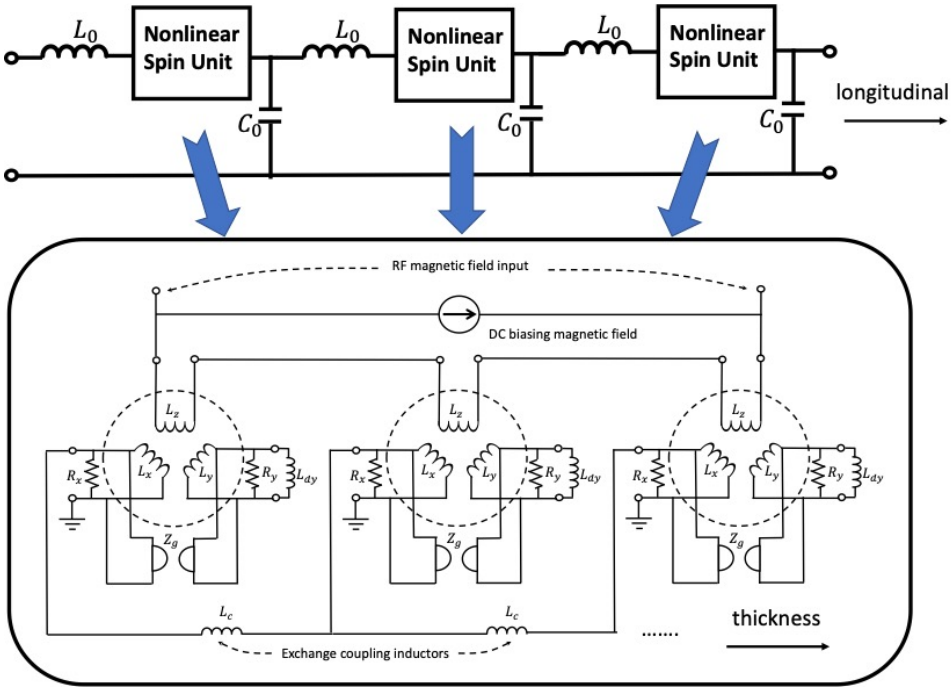

Figure 4.12: Proposed circuit model in the form of multiple segments of LC transmission line model where a nonlinear spin unit is inserted into each LC unit. Each nonlinear spin unit consists of a large group of nonlinear spin precession models, which are coupled to each other through a series inductor representing exchange coupling.

Fig.3.16(d).

The resulting equivalent circuit for the entire FSL device is thus yielded, as depicted in Fig.4.12, which consists of an LC ladder network that represents the transmission line but with the insertion of the nonlinear spin unit into each LC unit. The Z-ports are also excited by a common RF current representing the RF magnetic field under the center strip, which is approximately uniform over the cross-section of the stripline.

Such a model is used to predict the performance of a commercially available stripline FSL device presented in [76]. The stripline is 25 um wide, and the conductor is sandwiched by two layers of 100 um thick, 200 um wide single-crystal YIG. The total length of the stripline FSL is 38 mm, and the bias field applied is 100 Oe (7.96 x 103 A/m) in parallel with the

RF field. The circuit model uses 5 divisions in the longitudinal direction and 500 divisions in the thickness direction. The circuit parameters are chosen based on (3.24), (3.25), and (3.37).

The dimension parameters are defined as follows. Δz as the width of the ferrite, which is 200um, Δy or d as the thickness of each division in the thickness direction and with an additional factor of $\frac{1}{2}$ to include the upper half of the stripline area, which is 100um/500/2=100nm. Δx is the division in the longitudinal direction, which equals $38mm/5 = 7.6mm$. The YIG is assumed to have a saturation magnetization 1750 Oe ($1.39 \times 105A/m$) and a Gilbert damping constant of 5×10^{-4}. The entire circuit can be implemented in ADS and simulated with either transient simulations or envelope simulations. The damping resistors in the circuits are assumed to be thermal resistors, and their thermal noise excites the oscillation of spin waves powered by the RF field through the nonlinear spin precession.

The following four metrics are used to characterize the performance of the FSL device. (1) Limiting threshold. FSL devices start to attenuate the incoming RF signal when its power is above a certain threshold. This threshold is determined by the linewidth of the YIG material and the strength of the magnetic field, which is often controlled by the width of the center strip. (2) Power-dependent insertion loss. The attenuation level to the strong signal in FSL is nonlinear and depends on its power. Signal with higher power receives greater attenuation. (3) Delay time. FSL devices require a certain amount of energy to be established in the spin waves before they start to attenuate the incoming RF signal, which leads to a delay in the power-limiting action. This delay time depends on the input power level. (4) Frequency selectivity. The power-limiting mechanism of the FSL device is the coupling of the RF energy of the strong signal to the half-frequency spin wave oscillations in the material, which results in a significant energy loss to the strong signal. A weak signal that co-exists with the strong signal but at a different frequency should not correlate with the spin wave oscillations. It will thus not be attenuated in an ideal material with no damping. However, due to the damping of the spin precessions in real material, a certain correlation

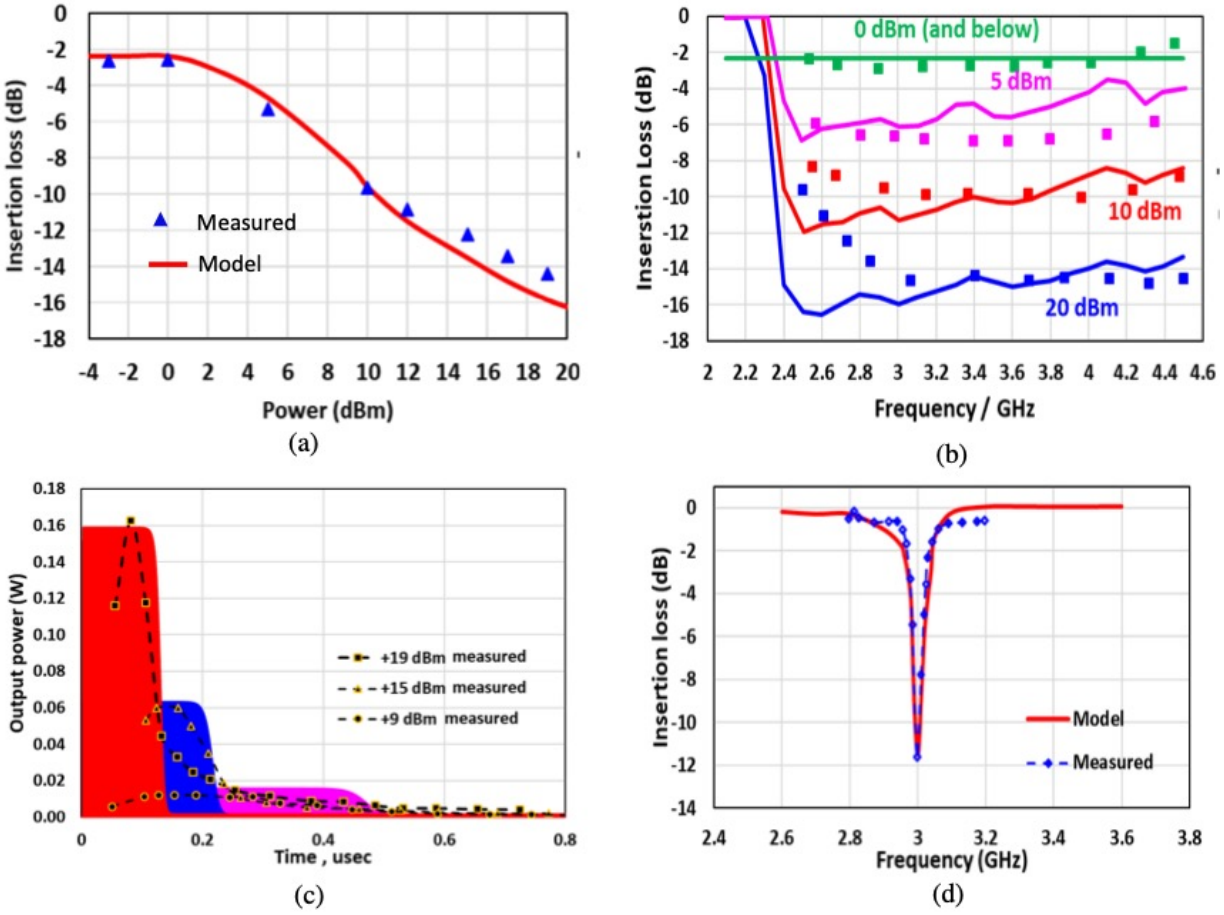

Figure 4.13: Fig.4.12 Simulated results for the stripline FSL device with the proposed circuit model, comparing to the measured results on the four metrics (a) Insertion loss vs. input power at 3GHz. (b) Insertion loss vs. frequency at four different power levels. (c) Delay time before the power limiting effect appears (d) Frequency selectivity when a strong signal presents at 3GHz. Courtesy of [76].

may be formed when the weak signal frequency is close to the strong signal frequency, which causes absorption of the weak signal. Frequency selectivity characterizes how narrow the absorption band the strong signal creates to the weak signal.

The predicted results with the circuit model for the above four performance metrics are plotted in Fig.4.13 (a)-(d) and compared with the experimental results presented in [76].

Table 4.1: Simulation Inductors' Values

	$/L_0$		$/L_0$		$/L_0$		$/L_0$
L_{11}	1.50	L_{21}	1.23	L_{31}	5.94	L_{41}	1.73
L_{12}	0.73	L_{22}	0.97	L_{32}	4.60	L_{42}	1.31
L_{13}	0.76	L_{23}	1.41	L_{33}	6.57	L_{43}	1.81
L_{14}	0.22	L_{24}	0.54	L_{34}	2.02	L_{44}	0.52
L_{15}	0.10	L_{25}	0.29	L_{35}	1.80	L_{45}	0.45

Very good agreement is observed for all four metrics, which confirms the effectiveness of the proposed model.

4.3.2 CPW FSL

The complete circuit model in Fig. 4.10 is implemented in the Advanced Design System (ADS) to simulate a CPW-FSL device provided by a third-party manufacturer. The total length of the CPW-FSL is 38 mm, and the center conductor width is 58 μm. The external bias field is applied by permanent magnets with $H_0 = 352\ Oe$, yielding a FMR frequency at 2 GHz with $N_y = 0.95, N_z = 0.05$ and $Ms = 1750Oe$. The conductors are sandwiched by two layers of 100 μm single-crystal YIG, making the effective width 116 μm. This is because the magnetic field lines will circle the top and bottom YIG thin films, doubling the widths of the YIG films. Experimental results including S-parameters, insertion loss, time delay, IM spectrum, and frequency selectivity are used as references and compared with simulation results from ADS to validate the proposed circuit model.

4.3.2.1 Simulation Setup

The discrete inductors' values used in the circuit model are summarized in Table 4.1. They are derived according to the simulated magnetic field distribution from Ansys HFSS and

Table 4.2: Simulation Effective Widths

	$/w$		$/w$		$/w$
z_{c11}	0.0345*2	z_{c21}	0.1264*2	z_{c31}	0.3141*2
z_{c12}	0.0725*2	z_{c22}	0.1639*2	z_{c32}	0.4179*2
z_{c13}	0.0696*2	z_{c23}	0.1133*2	z_{c33}	0.2923*2
z_{c14}	0.3144*2	z_{c24}	0.3809*2	z_{c34}	0.8802*2
z_{c15}	0.5176*2	z_{c25}	0.5467*2	z_{c35}	1.0560*2

(4.19)$\sim$(4.21). The values for the transmission line (TL) inductance and capacitance are also extracted from Ansys HFSS to be $L_0 = 0.87nH$ and $C_0 = 0.49fF$ for one FSL unit of length 1.52 mm. We can verify that the combination of these inductors will recover the original TL inductance. In other words,

$$\sum_i L_{i1} \left\| \sum_i L_{i2} \right\| \sum_i L_{i3} \left\| \sum_i L_{i4} \right\| \sum_i L_{i5} = L_o. \tag{4.23}$$

Table 4.2 summarizes the effective widths for the spin units according to (4.22). They are normalized to the CPW conductor width (58 μm). Each z_{cij} is multiplied by a factor of two to represent the double-layer effect. It is worth noting that the effective width is smaller for the spin units at the larger magnetic field region, i.e., z_{c11}, compared with that of the spin units at the smaller magnetic field region, i.e., z_{c31}.

Table 4.3 lists other simulation parameters. Notably, the damping constant α and the effective bias fields are made different for broadband simulations. The rationale for such changes are given in the Appendix. Apart from these changes, all other simulation parameters are defined from the physical device structure. For example, the length for one spin unit is $38mm/N = 1.52mm$, where N is the number of divisions along the length. The thicknesses for the spin units, on the other hand, relate with the physical thickness by the number of divisions along the thickness N_d. Note that this division is in addition to the division $d_1 \sim d_4$ based on the field profile.

Table 4.3: Other Simulation Parameters

Symbol	Meaning	Value
M_s	Saturation magnetization	$1750Oe$
α_1	Damping constant @4GHz	9.8×10^{-4}
α_2	Damping constant @5GHz	8.9×10^{-4}
α_3	Damping constant @6GHz	8.0×10^{-4}
H_0	External bias field	$352Oe$
H_{02}	Effective bias field @ 5GHz	$475Oe$
H_{03}	Effective bias field @ 6GHz	$613Oe$
θ	Angle between the bias field and the RF field	9°
N	Number of units divided in length	25
N_d	Number of units divided in thickness	5
d_1	thickness of divided regions 11∼15	2.5 μm
d_2	thickness of divided regions 21∼25	7.5 μm
d_3	thickness of divided regions 31∼35	90 μm
d_4	thickness of divided regions 41∼45	100 μm
w_1	width of divided regions 11∼41	2 μm
w_2	width of divided regions 12∼42	4 μm
w_3	width of divided regions 13∼43	4 μm
w_4	width of divided regions 14∼44	18 μm
w_5	width of divided regions 15∼45	30 μm
x_c	spin unit length	$38/N = 1.52mm$

Continued on next page

Table 4.3: Other Simulation Parameters (Continued)

y_{c1}	spin unit thickness for d_1	$2.5/N_d$=0.5 μm
y_{c2}	spin unit thickness for d_2	7.5 μm
y_{c3}	spin unit thickness for d_3	90 μm
z_c	spin unit effective width	From Table II
L_0	TL inductance for one FSL unit	0.87 nH
C_0	TL capacitance for one FSL unit	0.49 fF
N_x	Demagnetization factor in x direction	0
N_y	Demagnetization factor in y direction	0.95
N_z	Demagnetization factor in z direction	0.05

4.3.2.2 Comparison Between Simulation and Measurements

- **Small Signal S-parameters**

The comparison between small signal simulated S-parameters and measurements are shown in Fig. 4.14 from 1 GHz to 8 GHz. A broadband match is indicated in S_{11} because the characteristic impedance of the CPW line is designed to match 50 ohm port impedance. From the S_{21} plot, the FMR absorption starts at around 2 GHz. The absorption from 3 GHz to 4 GHz, on the other hand, is attributed to the excitation of magnetostatic waves, which will be included in future publications.

- **Large Signal Insertion Loss**

The large signal insertion loss of the CPW-FSL device was obtained from the decibel value of the output power over the input power. The comparisons between the measurement results and the simulation results at 4 GHz, 5 GHz, and 6 GHz are shown in Fig. 4.15(a). With a bias field of $H_0 = 254\ Oe$, the FMR frequency is 2 GHz, so the FSL power absorption starts

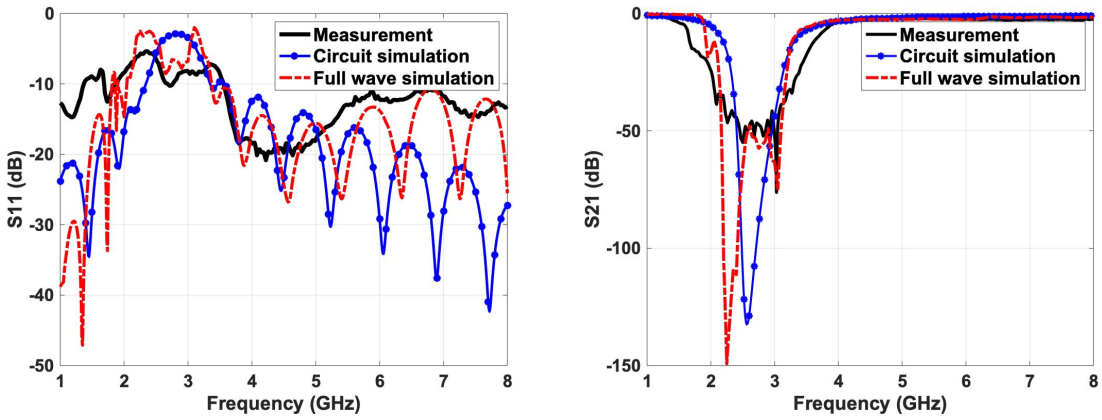

(a) (b)

Figure 4.14: Small signal (a) S_{11} (b) S_{21} comparison between measurement, circuit simulation, and full wave simulation from 1 GHz to 8 GHz.

at $2 \times f_r = 4$ GHz. Higher frequency, on the other hand, excites higher-order spin waves propagating along the periodic circuit in Fig. 4.2.

The comparisons between the measurement results and the simulation results are shown in Fig. 4.15(a). The simulation results have a good match with the measurement results, showing a power threshold of 0 dBm, 5 dBm, and 8 dBm for 4 GHz, 5 GHz, and 6 GHz excitations, respectively.

Specifically, the comparison between the uniform model and nonuniform model is shown in Fig. 4.15(b). The red dotted line is the simulation results without considering field nonuniformity, i.e., the model in [76] where a single L_0 is used. The blue solid line, on the other hand, is the simulation results considering field nonuniformity, i.e., the model in Fig. 4.10 where the inductor array is used. By considering field nonuniformity, the softening of the power threshold can be predicted because the spin units are excited nonuniformly.

- **Time Delay**

In FSLs, the buildup of spin wave oscillations requires time, which leads to a certain time

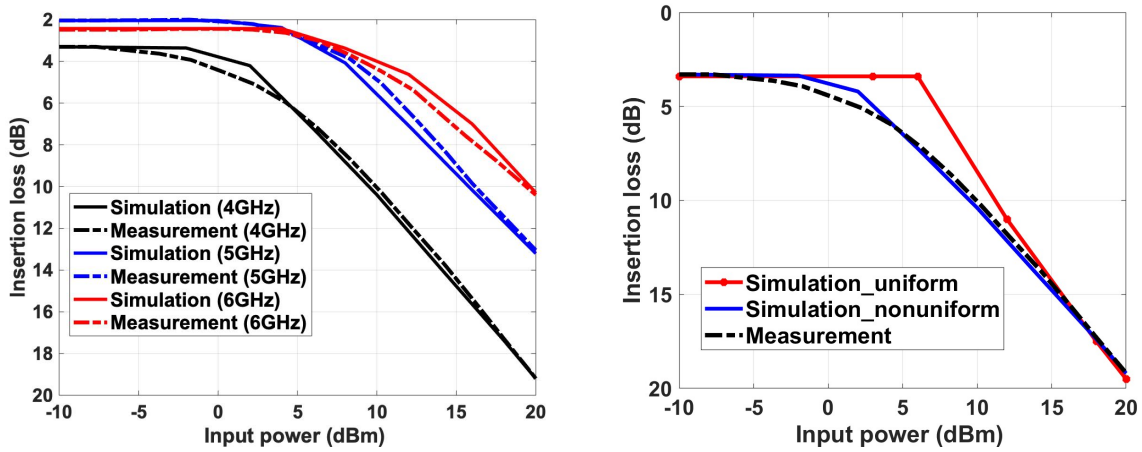

(a) (b)

Figure 4.15: (a) Comparison of insertion loss between measurement results and simulation results with input power sweeping from -10 dBm to 20 dBm at 4 GHz, 5 GHz, and 6 GHz.(b) Comparison of insertion loss between measurement and simulation results with and without considering field nonuniformity. The input power sweeps from -10 dBm to 20 dBm at 4 GHz.

delay before the device attenuates a large signal. Such time delay can be quantified by measuring voltage waveforms at the output of the FSL device. The measurement set-up is shown in Fig. 4.16, where a 4 GHz signal is generated by a Tektronix Arbitrary Waveform Generator (AWG) 7112C with a 12 Gs/s DAC sampling rate. Afterwards, the signal is connected to a power amplifier (PA) to provide high-power signals to the FSL device. The output of the FSL is then connected to the digital oscilloscope with a 100 Gs/s sampling rate to capture the output voltage waveforms. The comparison of voltage waveforms is shown in Fig. 4.17. Initially, at time $t = 0$, the high-power signal passes through the FSL device unaffected by the YIG film, causing a large output peak voltage. After some time, however, the power-limiting effect shows up, and the output voltage peak-to-peak value becomes smaller because the signal power is lost in the YIG film. In addition, when the input power becomes larger, the delay time becomes shorter. The time delay for P_{in}=12 dBm was 0.85 μs, while the time delay for P_{in}=16 dBm was 0.65 μs. A close match between simulation

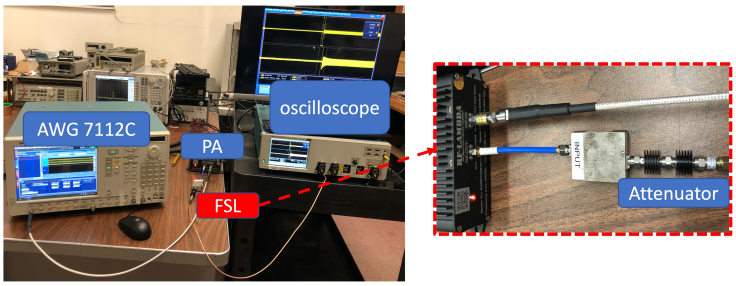

Figure 4.16: FSL transient measurement set-up.

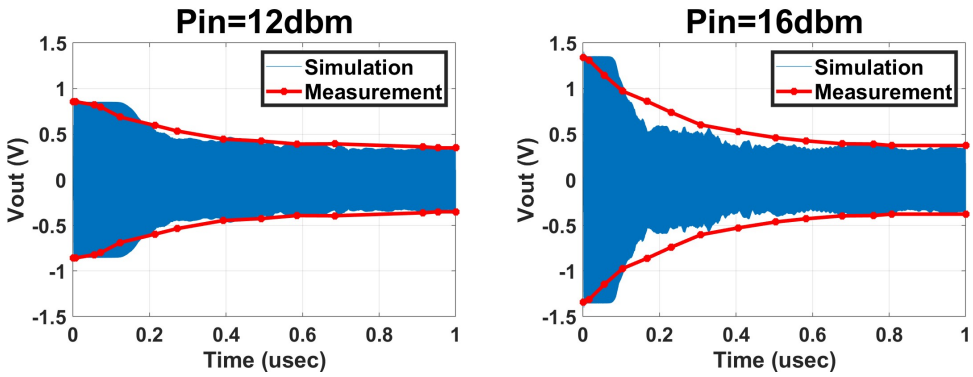

(a) (b)

Figure 4.17: Comparison of voltage waveforms at 4 GHz at the FSL output between measurement (dotted red lines) and simulation (solid blue areas) with input power to FSL of (a) 12 dBm and (b) 16 dBm.

and measurement results indicates that the proposed circuit model can predict the transient response of the FSL device in addition to the steady-state response, i.e., insertion loss.

- **Intermodulation (IM) Spectrum**

Due to the nonlinear nature of the FSL device, intermodulation (IM) tones will be generated when more than one frequency tone is present at the input, with at least one above threshold[24]. A sample signal spectrum at the output of the device is shown in Fig. 4.18, where two tones are present, with f_1 at 3.997 GHz and f_2 at 4.003 GHz. The two signals have different powers, with P_1 =10 dBm and P_2 =-12.6 dBm. According to Fig. 4.15, the power

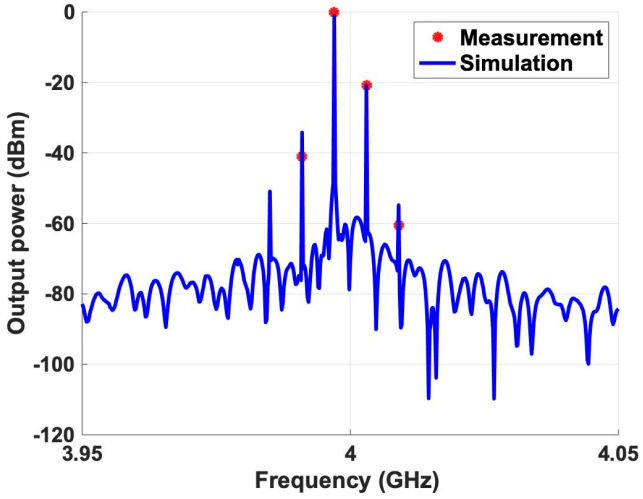

Figure 4.18: IM spectrum comparison between simulation (blue lines) and measurement (red dots) when P_1=10 dBm at 3.997 GHz and P_2=-12.6 dBm at 4.003 GHz.

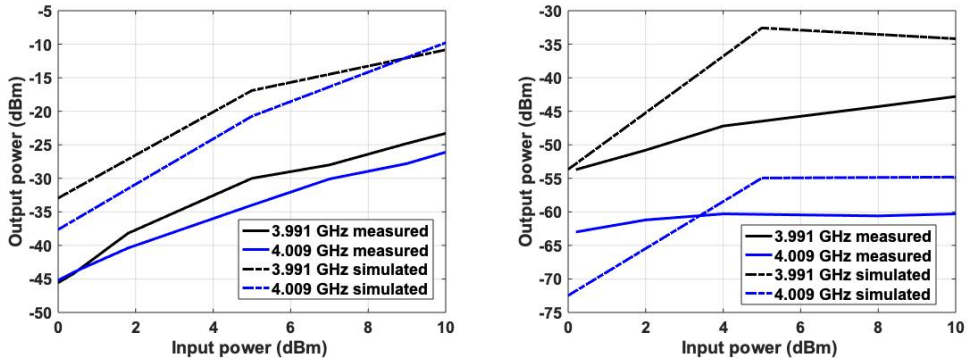

(a) (b)

Figure 4.19: IM3 power comparison between simulation (dashed lines) and measurement (solid lines) when (a) P_1=P_2 sweeps from 0 dBm to 10 dBm, with f_1=3.997 GHz and f_2=4.003 GHz (b) P_1 sweeps from 0 dBm to 10 dBm at 3.997 GHz and P_2=-12.6 dBm at 4.003 GHz..

threshold at 4 GHz is around 0 dBm, making f_1 an above-threshold signal. As a result, IM tones are generated at the output. Specifically, third-order IM tones are generated at $2*f_1-f_2$ =3.991 GHz and $2*f_2-f_1$ =4.009 GHz. The comparison between simulation and

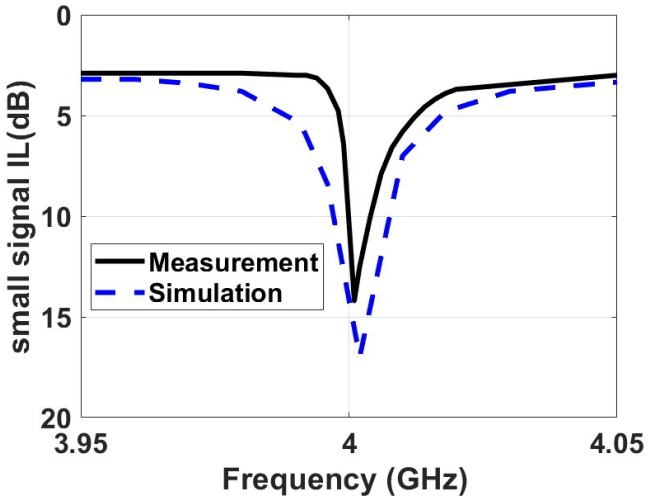

Figure 4.20: Frequency selectivity comparison between simulation (blue dashed line) and measurement (black solid line) when P_1=10 dBm at 4 GHz and P_2=-10 dBm sweeps from 3.95 GHz to 4.05 GHz.

measurement indicates that the circuit model is capable of predicting the IM tone's power levels to a certain degree.

Fig. 4.19 shows more results with input power level sweeping. For example, Fig. 4.19(a) shows the third-order intermodulation (IM3) tones power comparison at different frequencies between simulation (dashed lines) and measurement (solid lines) when P_1 sweeps from 0 dBm to 10 dBm at 3.997 GHz and P_2 remains to be -12.6 dBm at 4.003 GHz. On the other hand, Fig. 4.19(b) shows the output power comparison with equal-power input tones. In other words, $P_1 = P_2$ sweeps from 0 dBm to 10 dBm. In this case, stronger IM3 tones are generated because the two signals are over-threshold. The discrepancies between the simulation results and the measurement might be attributed to the inhomogeneous bias field in the device that is hard to quantify in the current device setup.

- **Frequency Selectivity**

Frequency selectivity reflects FSL's capability to limit a large signal without affecting a small

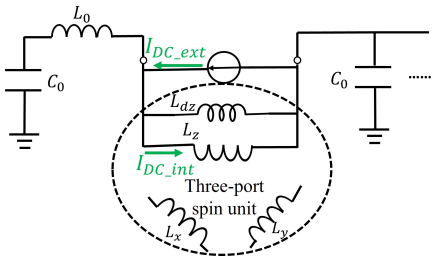

Figure 4.21: Justification of the asymmetry in the frequency selectivity plot. I_{DC_ext} is the external DC current, and I_{DC_int} is the internal DC current.

signal nearby if the frequency separation is a few tens of MHz. This behavior is measured and simulated by fixing an over-threshold (10 dBm) signal at 4 GHz while sweeping a below-threshold (-10 dBm) signal from 3.95 GHz to 4.05 GHz. A comparison of small signal insertion loss between the simulation and measurement is shown in Fig. 4.20. It's worth noticing that the maximum absorption occurs slightly higher than the large signal frequency at 4 GHz. This shift of frequency and the asymmetry of the small signal insertion loss is believed to be caused by the reduction of the DC demagnetization field caused by large spin wave amplitudes [74]. To be specific, the internal bias field is related to the external bias field by $H_i = H_0 - N_z M_z$. With small RF excitation, $M_z \approx M_s$. However, when the RF power becomes larger, $M_z < M_s$ because of the increase of spin precession angle. Consequently, the internal bias field becomes larger, resulting in a higher FMR frequency. In the circuit perspective, as shown in Fig.4.21, the external bias current I_{DC_ext} is shared between L_{dz} and L_z, where L_{dz} is related with N_z according to (3.25) and L_z is a nonlinear inductor. With higher power, L_z becomes smaller, causing a greater I_{DC_int}. This shift of FMR frequency to a higher end accounts for the observed asymmetry in Fig.4.21. This phenomenon has also been reported in [70] and [94]. The fact that the demagnetization in all dimensions has been included in the three-port spin model provides the modeling capability of such asymmetry.

Table 4.4: Computation Time With Different Simulators

Simulators	Linear simulation	Nonlinear simulation
HFSS	$>$ 20 hrs for the entire device; 2 hrs for 1/8 of the device	Not capable
ADS with circuit in [76]	10 secs	7 hrs
ADS with circuit in [93]	10 secs	2 hrs

4.4 Model Evaluation: Computation Time

A comparison of computation time with different simulators is included in Table 4.4. For linear simulations, the circuit simulator takes significantly less time than the full-wave simulator Ansys HFSS [50]. In practice, only 1/8 of the entire device is simulated in HFSS to extract the field profile. On the other hand, the computation time for nonlinear simulations depends on the total number of spin units. For the circuit in [76] (for a stripline-FSL), 500 divisions are created in the thickness direction and five in the length direction, resulting in 2500 spin units in total. For the circuit in [93] (for a CPW-FSL), 35 spin units are included in one FSL unit, with 25 FSL units connected in the length direction. Hence, there are 875 spin units, resulting in a shorter simulation time with even better simulation accuracy with field nonuniformity considered. The number of thickness divisions is smaller with $N_d = 5$ because broadband simulation is mainly facilitated by changing effective bias fields and damping constants. Otherwise, N_d is directly related to the highest frequency the circuit can simulate.

CHAPTER 5

Modeling and Design of Millimeter Wave Resonators and Filters Based on Hexagonal Ferrite

5.1 Background and Motivation

As discussed in Chapter 1, magnetic resonators and filters based on ferromagnetic resonance (FMR) have been demonstrated since the 1960s [101, 102] through embedding YIG spheres in a waveguide structure. They can achieve broader frequency ranges than electrical filters and mechanical filters because the tuning is directly related to the FMR frequency of the ferrite material, which changes both its effective inductance and capacitance at the same time.

Recently, there has been a critical need to extend current microwave magnetic devices into the millimeter wave range to exploit the frequency spectrum further. Two important strategies have evolved to boost the operating frequency of the magnetic filters. One is to use high-$4\pi M_s$ ferromagnetic metals to replace the low-$4\pi M_s$ YIG ferrites. It has been demonstrated that using metallic thin films allows for the practical development of notch or band-stop [40] and bandpass filters [41]. The second strategy is to use low-loss hexagonal ferrites. The hexagonal ferrites have built-in high anisotropy fields and can provide a self-biasing for mm-wave applications in the 30–100 GHz range. Recent simulations have demonstrated the feasibility of hexagonal ferrite-based, stripline-type, mm-wave filters [42]. Experimentally, [43] demonstrates a prototype mm-wave notch filter based on a BaM slab with an in-plane uniaxial anisotropy field of 17 kOe, which facilitates the operation of the

filter over 51–54 GHz for an external field range of 1500–2700 Oe. The device is compatible with monolithic integrated circuits. In addition to notch filters, bandpass filters using hexagonal ferrites have also been demonstrated based on coupled waveguides [44]-[46]. In [44], M. Sterns et al. presented a novel tunable bandpass filter based on open-ended fin lines. Hexagonal ferrite spheres are used as resonators to cover a tuning frequency range from 39 GHz to 68 GHz. The measured insertion loss of the filter varies from 5.3 dB to 7 dB, with a typical 3 dB bandwidth between 300 MHz and 400 MHz. The stacking of two waveguides achieves off-resonance isolation of about 60 dB. A multi-slot iris is carefully designed to couple two resonator spheres while maintaining good off-resonance isolation. A similar structure using shielded co-planar waveguides (CPW) is presented in [46].

Despite these continuous research interests, several factors hinder the design of mm-wave magnetic resonators or filters. Firstly, there is no systematic way of design, and full-wave simulators are heavily relied on to tune device parameters. Secondly, no performance metrics are used to evaluate the device performance based on different coupling structures. Thirdly, the waveguide-based design in [44]-[46] is bulky in size, with potential room for better integration of bulk BaM crystal spheres.

This section discusses the modeling and design of BaM resonators and filters based on the equivalent circuit representation. It expands from the state-of-the-art magnetic filter design in the following aspects:

- A systematic way is proposed to design mm-wave BaM resonators and filters. The resonator is optimized for a good energy coupling coefficient and then coupled to construct a bandpass filter.

- A performance metric for BaM resonators is proposed using an equivalent circuit model, which quantifies the efficiency of coupling between electromagnetic (EM) waves and spin precession. A discussion on the effects of different device parameters on coupling factors is included.

- The design procedure for a bandpass filter through coupling several BaM resonators is delineated.
- A planar printed-circuit-board-based design of BaM resonators and filters is fabricated and measured. A comparison between measurement results and simulation results validates the proposed design procedure.
- A Small device form factor is achieved, with an effective resonator of 1.1 mm $\times$ 1.5 mm and bandpass filter of size 9 mm $\times$ 2.4 mm.

5.2 Modeling and Design of Resonators Built With BaM Sphere

Using sphere-shaped resonators offers significant benefits due to the direct linear relationship between the resonant frequency ω_r and the external bias field $H_{0,ext}$, which is given by

$$\omega_r = \mu_0 \gamma (H_{0,ext} + H_a) \tag{5.1}$$

where H_a represents the anisotropic field strength and is in the same direction as the bias field $H_{0,ext}$. In this section, the modeling of BaM sphere resonators is included, and device metrics are proposed to quantify the resonator design with different transmission line structures.

5.2.1 Equivalent Circuit Representation of BaM Sphere Resonators

A hexagonal ferrite sphere has a diameter d and is biased in the z-direction, whose anisotropy field H_a aligns with external bias field direction $H_{0,ext}$. Hence, H_a can be treated as part of the bias current in the circuit model constructed in Chapter 3, Fig. 3.2. An RF magnetic field H_{rf} is applied in the X-direction, provided by a transmission line. The two-port gyrator circuit equivalence is modified from Fig. 3.2 to become as shown in Fig. 5.1, with the corresponding circuit elements' value. Note that the volumetric effect of the sphere is included in a scaling factor $\pi/6$, as discussed in [64].

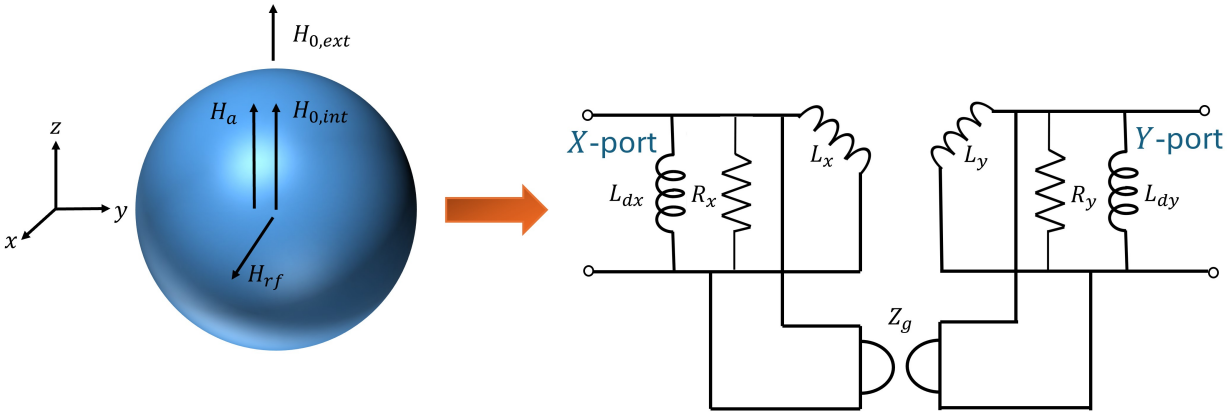

Figure 5.1: Two-port equivalent circuit model for the barium hexagonal ferrite sphere biased in z direction.

$$Z_g = \mu_0^2 \gamma M_s d \frac{\pi}{6} \tag{5.2}$$

$$L_x = \mu_0 \frac{M_S}{H_{0,ext} + H_a} d \frac{\pi}{6} \tag{5.3}$$

$$L_y = \mu_0 \frac{M_S}{H_{0,ext} + H_a} d \frac{\pi}{6} \tag{5.4}$$

$$L_{dx} = \mu_0 \frac{d\pi}{(N_x - N_z)\,6} = O \cdot C \cdot \left(N_x = N_z = \frac{1}{3} \right) \tag{5.5}$$

$$L_{dy} = \mu_0 \frac{d\pi}{(N_y - N_z)\,6} = O \cdot C \cdot \left(N_y = N_z = \frac{1}{3} \right) \tag{5.6}$$

With a transmission line excitation, the RF magnetic can be assumed to be in the X-direction. Hence, the two-port circuit model can be simplified to one-port, as shown in Fig. 5.2. Specifically, L_y is transformed from Z_g to become C_m:

$$C_m = \frac{L_y}{{Z_g}^2} = \frac{1}{\mu_0 \omega_0 \omega_m} \frac{6}{d\pi} \tag{5.7}$$

And the resonance frequency is given by:

$$\omega_r = \frac{1}{\sqrt{L_m C_m}} = \omega_0 = \mu_0 \gamma (H_{0,ext} + H_a) \tag{5.8}$$

which corresponds with the FMR frequency for a ferrite sphere according to Kittle's equation.

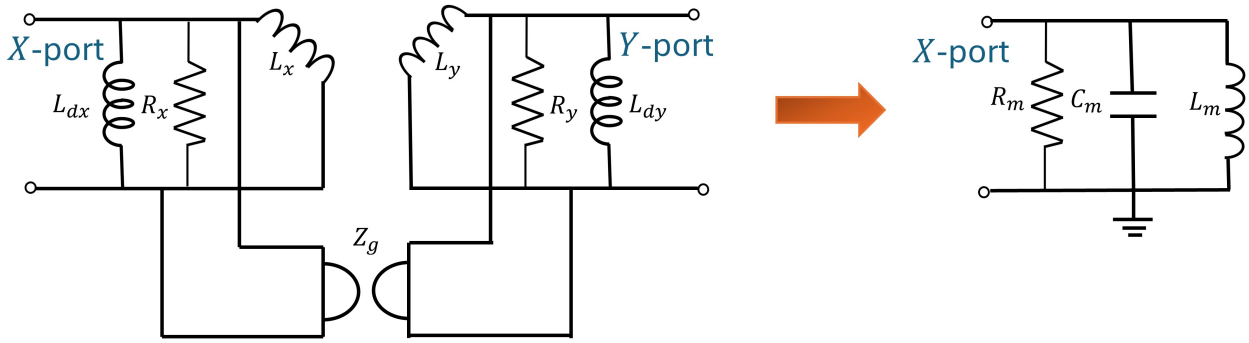

Figure 5.2: One-port equivalent circuit model for the barium hexagonal ferrite sphere.

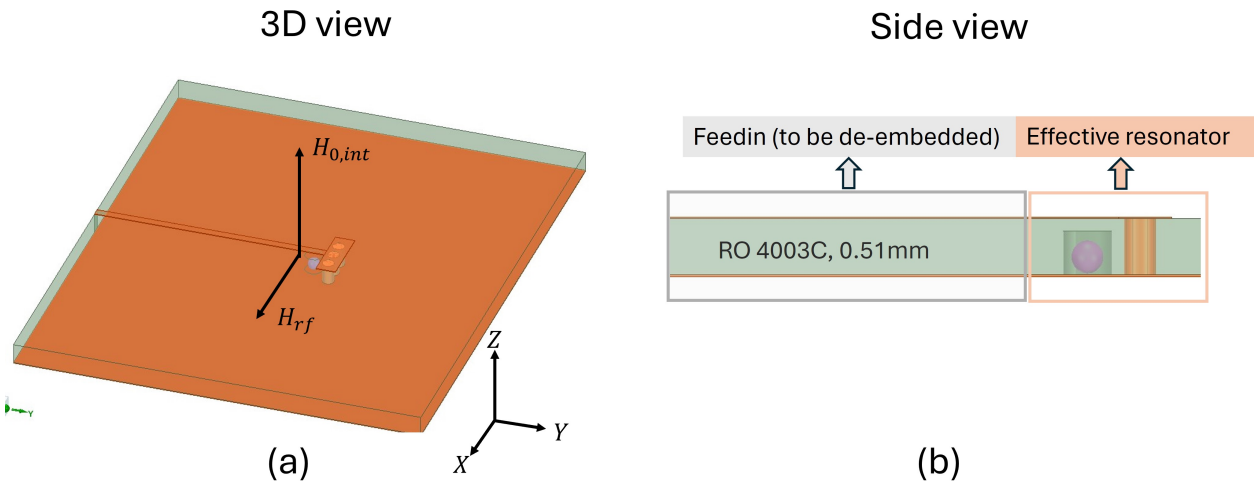

Figure 5.3: HFSS schematic of a BaM resonator. (a) 3D view.(b) Side view. A microstrip line of width 0.2mm is excited on the left side and grounded on the right side. The BaM sphere is inserted inside a blind via near the grounding vias.

5.2.2 Modeling of a Transmission Line loaded BaM Sphere Resonator

5.2.2.1 Device Schematic

A transmission line is necessary to excite the BaM sphere resonator. Specifically, the microstrip line is known to have a uniform field distribution inside the substrates, making it a good candidate for FMR mode excitation. A proposed design schematic is shown in Fig.5.3,

where a microstrip line of width 0.2 mm is set on top of the Rogers 4003C substrate of thickness 0.51mm. It is excited through a lumped port on the left-hand side and grounded through three vias on the right-hand side. The extra feeding length of the microstrip line facilitates the connection of end-launch connectors during PCB fabrication. This feeding line is not part of the resonator structure and will be de-embedded using the Thru-Reflect-Line (TRL) technique [101].

The BaM sphere is placed next to the shorted end of the microstrip line inside a blind cylindrical via with radius $r = 0.2mm$ and thickness $h_{via} = 0.4mm$. The blind via is greater than the BaM sphere to facilitate easy assembly and allow the sphere to rotate freely inside the via when the bias field is applied for its self-alignment between the anisotropy field and the bias field. By doing this, no manual alignment is needed during the fabrication process.

5.2.2.2 Equivalent Circuit Model for the Resonator

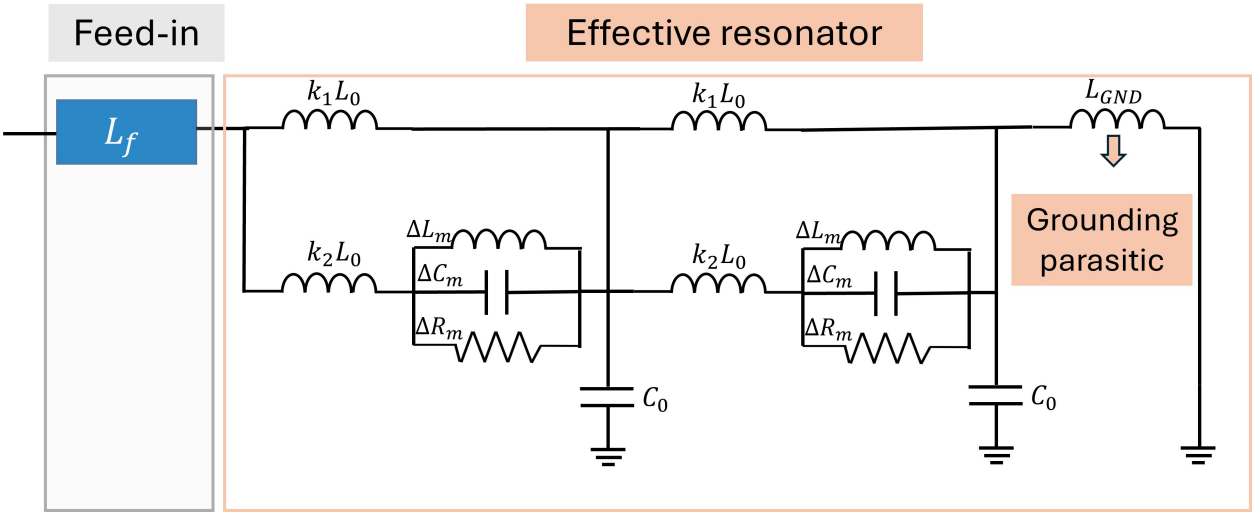

Figure 5.4: Equivalent circuit model for the transmission line loaded ferrite resonator.

The complete circuit model for the transmission line loaded ferrite sphere resonator becomes as shown in Fig.5.4. The feeding part is a microstrip line of length L_f in this case, while it can also be any S-parameter box output from the TRL calibration. The effective

resonator comprises several sections of the LC ladder network, with parallel RLC resonators representing the BaM sphere inserted in between. Another section of the transmission line represents the grounding parasitics. At the effective resonator region, the transmission line

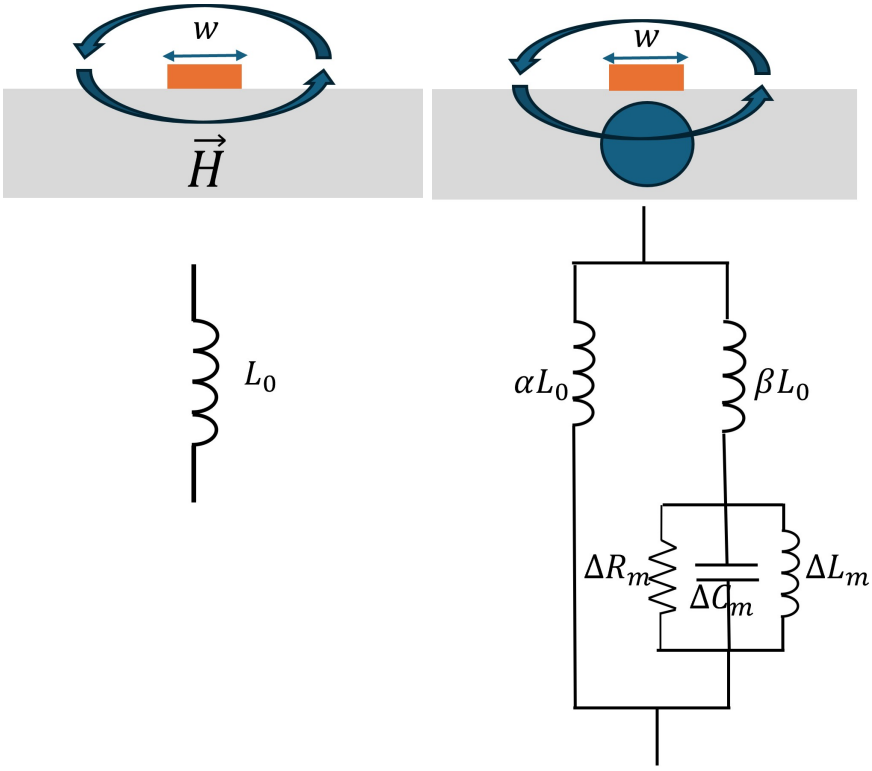

Figure 5.5: Illustration of magnetic flux and transmission line inductance (a) without ferrite sphere. (b) with a ferrite sphere. The equivalent ferrite resonator $\Delta L_m, \Delta C_m, \Delta R_m$ is inserted into one branch of the transmission line inductor.

inductor L_o is divided into two parallel-connected sub-inductors $(k_1 L_0, k_2 L_0)$ to reflect that the BaM sphere is only present inside the substrate, the bottom half of the microstrip line. In other words, not all magnetic flux is enclosed by the BaM sphere, with a certain air portion. The detailed reasoning of such division is similar to the CPW-FSL modeling, as delineated in Chapter 3. With a microstrip line, the magnetic field can be assumed to be uniform along the width direction. Hence, the transmission line inductance L_0 can be divided into two $2L_0$,

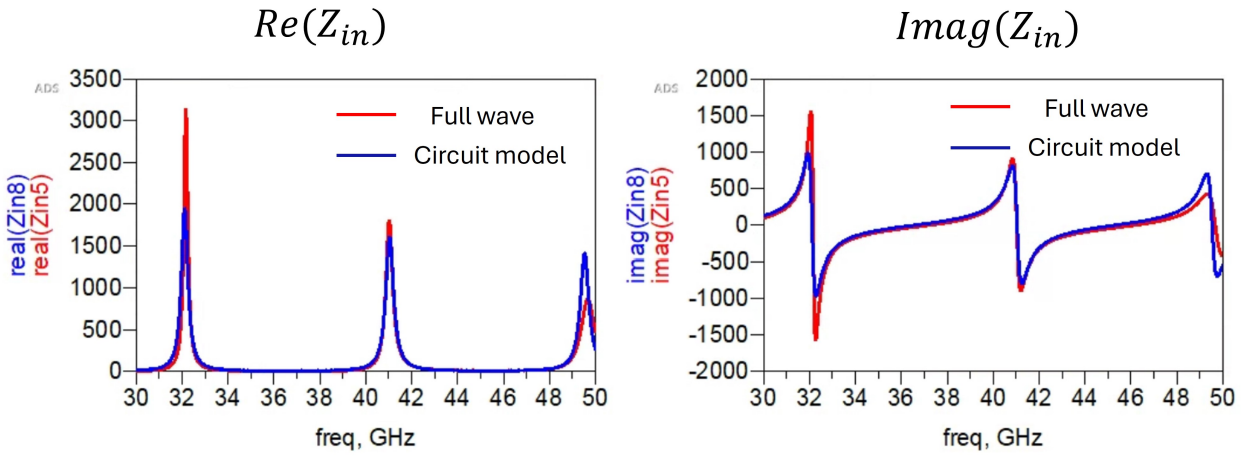

Figure 5.6: Comparison of Re(Zin) and Imag(Zin) of the entire structure between HFSS simulated results (red lines) and ADS circuit results (blue lines) when there is no BaM sphere.

as shown in Fig. 5.5 (b), representing the substrate and air flux, respectively.

5.2.2.3 Validation of the Equivalent Circuit Model

The proposed circuit representation can be validated against full-wave simulations for the no-ferrite and with-ferrite cases. For the no-ferrite case, a comparison of $Re(Z_{in})$ and $Imag(Z_{in})$ is shown in Fig. 5.6. The transmission line inductance at the effective resonator region is extracted to be $L_0 = 0.24nH$. The transmission line capacitance C_0 is calculated by $C_0 = \frac{L_0}{Z_0^2}$, substituting $Z_0 = 120Ohm$ for a line width of 0.2 mm. In addition, it is worth noticing that the transmission line itself yields multiple resonances with $L_f = 9.3mm$.

With the ferrite resonator added, parallel RLC resonators are distributively connected to the transmission line, as shown in Fig.5.4. The values of ΔL_m and ΔC_m are calculated rigorously from equations (5.6) and (5.7). Specifically, an internal effective field of 13333 Oe is applied in the Z-direction during simulation, which in practice consists of both an external bias field and an internal anisotropy field. Substituting $d = 300\mu m$, $H_{0,ext} + H_a = 13333Oe + M_s/3$, and $M_s = 4600Oe$ to (5.6), the theoretical L_m is calculated to be 60 pH,

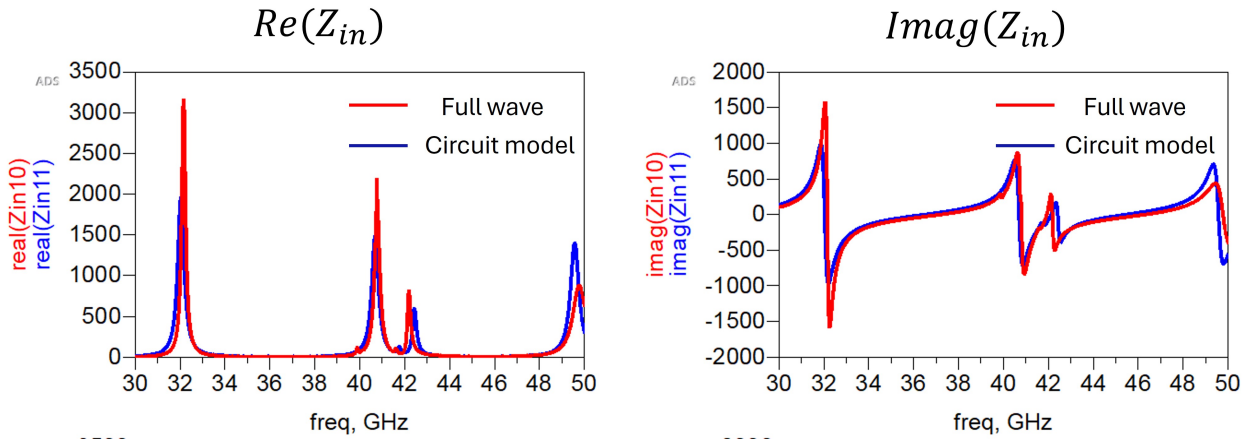

Figure 5.7: Comparison of Re(Zin) and Imag(Zin) of the entire structure between HFSS simulated results (red lines) and ADS circuit results (blue lines) when there is a BaM sphere.

with a theoretical FMR frequency of 41.2 GHz. Since two parallel RLCs are inserted in a distributed fashion, each resonator should yield half of the theoretical L_m inductance. In other words, $\Delta L_m = \frac{1}{2} L_m = 30pH$.

A comparison between full-wave and circuit model simulation results with the sphere resonator is included in Fig.5.7. With the addition of the BaM sphere, The simulation results in terms of $real(Z_{in})$ and $imag(Z_{in})$ match roughly between full-wave simulation and circuit model. The remaining discrepancies may be because the sphere is not excited uniformly in simulation, while equations (5.6) and (5.7) assume a uniform excitation.

5.2.2.4 TRL Calibration of the Feeding Part

The ferrite resonator is fed through a feed-in line. In simulation, it is a microstrip line of length L_f. In the experiment, it combines a connector and a microstrip line, which adds to additional losses and phase shifts. Hence, it is essential to de-embed the feed-in line's effect to see the effective resonator's real response, which is the orange portion in Fig. 5.4. Here, the Thru-Reflect-Line (TRL) technique [101] is adopted. The calibration procedure is illustrated in Fig.5.8, and the HFSS schematic is shown in Fig.5.9. Specifically, three

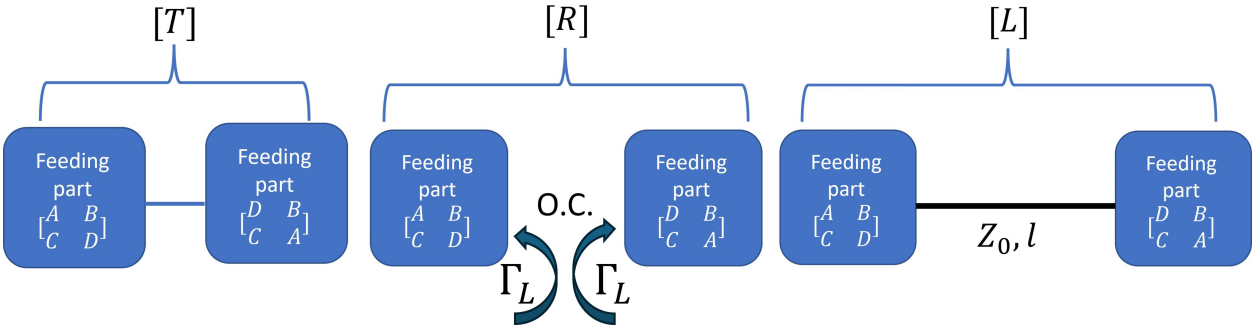

Figure 5.8: TRL calibration setup.

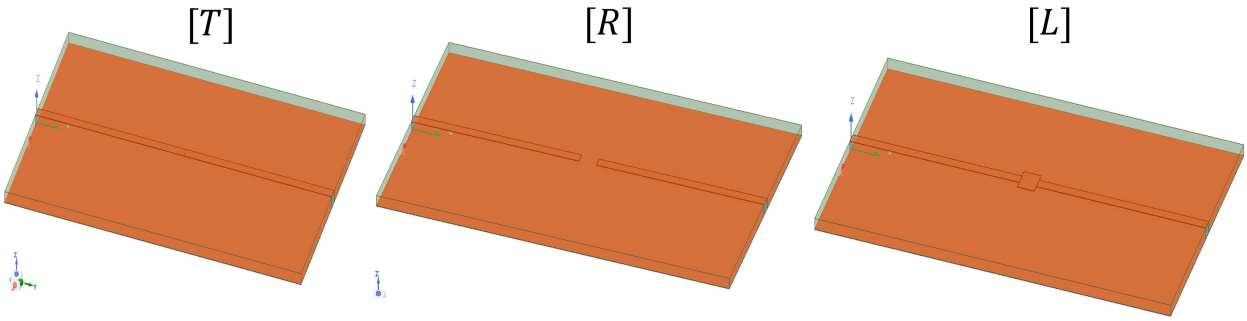

Figure 5.9: TRL calibration setup in HFSS.

sets of measurements (through, reflect, and line) are performed, generating three sets of S-parameters: $[T]$,$[R]$, and $[L]$. The 'Through' measurement means two symmetrical feeding parts are connected, and the S-parameter $[T]$ is obtained. 'Reflect' measurement means the reference plane between two feeding parts is left open or short, with a reflection coefficient Γ_L. In this case, it is open. The corresponding S-parameter $[R]$ is obtained. 'Line' measurement means the reference plane between two feeding parts is connected using a transmission line with length l and a characteristic impedance $Z_o = 50Ohm$. The S-parameter $[L]$ is obtained. Using the signal flow graph approach, the S-parameters of the feeding parts $[S]$ are related

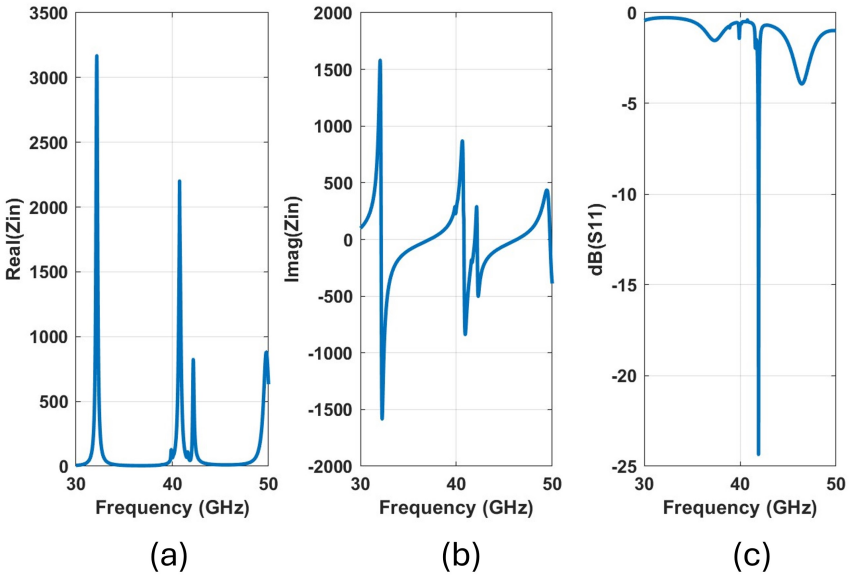

Figure 5.10: Plot of (a) $Re(Z_{in})$ (b) $Imag(Z_{in})$ (c) $dB(S_{11})$ of the entire resonator.

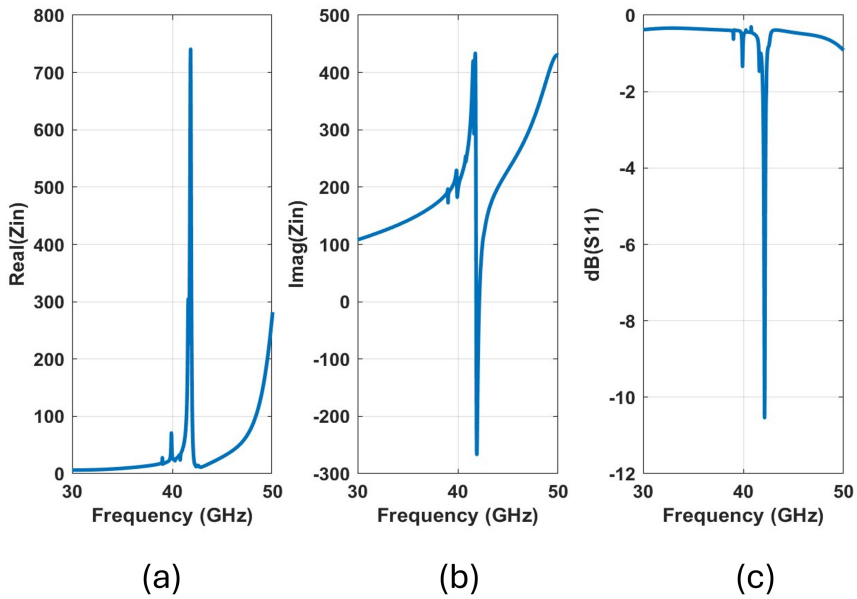

Figure 5.11: Plot of (a) $Re(Z_{in})$ (b) $Imag(Z_{in})$ (c) $dB(S_{11})$ of the effective resonator after feed-in deembedding.

to $[T], [R], [L]$ by the following equations:

$$\begin{cases} T_{11} = S_{11} + \frac{S_{22}S_{12}^2}{1-{S_{22}}^2} \\ T_{12} = \frac{{S_{12}}^2}{1-{S_{22}}^2} \\ R_{11} = S_{11} + \frac{{S_{12}}^2\Gamma_L}{1-S_{22}\Gamma_L} \\ L_{11} = S_{11} + \frac{S_{22}{S_{12}}^2e^{-2\gamma l}}{1-{S_{22}}^2e^{-2\gamma l}} \\ L_{12} = \frac{{S_{12}}^2e^{-2\gamma l}}{1-{S_{22}}^2e^{-2\gamma l}} \end{cases} \tag{5.9}$$

Solving equation (5.9) leads to the following expressions for feed-in S-parameters:

$$\begin{cases} e^{\gamma\ell} = \frac{L_{12}^2+T_{12}^2-(T_{11}-L_{11})^2 \pm \sqrt{\left[L_{12}^2+T_{12}^2-(T_{11}-L_{11})^2\right]^2-4L_{12}^2T_{12}^2}}{2L_{12}T_{12}} \\ S_{22} = \frac{T_{11}-L_{11}}{T_{12}-L_{12}e^{-\gamma\ell}} \\ S_{11} = T_{11} - S_{22}T_{12} \\ S_{12}^2 = T_{12}\left(1-S_{22}^2\right) \\ \Gamma_L = \frac{R_{11}-S_{11}}{S_{12}^2+S_{22}(R_{11}-S_{11})} \end{cases} \tag{5.10}$$

Note that the choice of sign for $e^{\gamma\ell}$ can be determined by the requirement that imaginary parts of γ be positive or by knowing the phase of Γ_L to be within 90 degrees (for an open connection for the 'reflect' measurement). After feeding part de-embedding, the effective resonator response in terms of $Re(Z_{in})$, $Imag(Z_{in})$, and $dB(S_{11}$ is included in Fig. 5.11. We can notice the difference between the effective resonator and the whole structure, as plotted in Fig. 5.10 (a) - (c) for comparison. After feed-in line de-embedding, the transmission line resonances are shifted further away from the frequency band of interest, and the ferrite resonance at 41 GHz can be seen clearly in Fig. 5.11 (a) and Fig. 5.11 (b). On the other hand, the S-parameter plots are similar for both cases, with the dip corresponding to the FMR frequency.

5.2.2.5 Energy Coupling Factor

Common performance metrics should be defined to quantify and characterize the performance of ferrite resonators built with different structures. In surface acoustic wave (SAW)

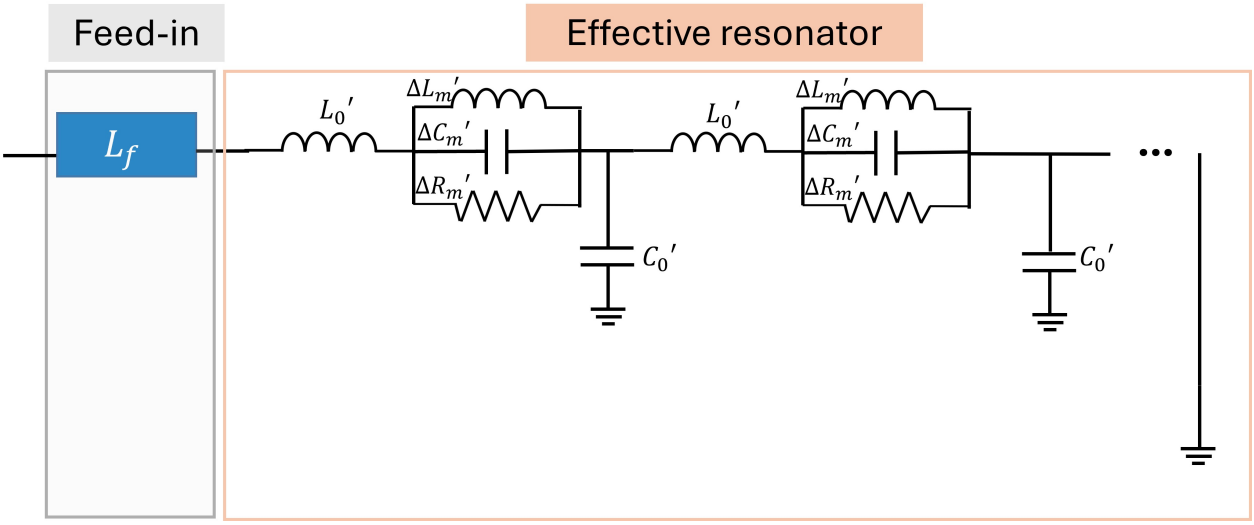

Figure 5.12: Equivalent circuit model to define coupling factor.

and bulk acoustic wave (BAW) resonators, an important design metric is the 'energy coupling factor,' defined as the ratio between the internal resonator capacitance C_m and the external electrode capacitance C_0 [103, 104]. Similarly, the energy coupling factor in the ferrite resonator system can be defined as the ratio between ferrite inductance L_m and external transmission line inductance L_0. In other words,

$$c = \frac{L_m}{L_o}. \tag{5.11}$$

Specifically, the equivalent circuit representation is illustrated in Fig. 5.12 for the microstrip line structure described earlier. Due to fabrication limits, the transmission line length at the resonator region can not be well represented by a single inductor. On the other hand, several sections of the LC ladder network have to be cascaded with several PRLC units representing ferrite to form an entire circuit equivalence. Note that Fig. 5.12 is another form of Fig. 5.4. In Fig. 5.4, the PRLC is in series with one branch of transmission line inductance to reflect the physics of the structure. In Fig. 5.12, the PRLC is in series with the LC ladder network to extract the coupling factor. Obviously, the values for $\Delta L_m^{'}$, $\Delta C_m^{'}$, and $\Delta R_m^{'}$ in Fig. 5.12 should not be the same as ΔL_m, ΔC_m, and ΔR_m in Fig. 5.4

Table 5.1: Parameter value in Fig. 5.12

$\Delta R_m^{'}$	$\Delta L_m^{'}$	$\Delta C_m^{'}$	$L_0^{'}$	$C_0^{'}$	c
$100Ohm$	$2.1e^{-12}H$	$7.1e^{-12}F$	$1.3e^{-10}H$	$9.028e^{-15}F$	1.6%

due to different circuit topology. The values are of $\Delta L_m^{'}$, $\Delta C_m^{'}$, and $\Delta R_m^{'}$ are summarized in Table 5.1.

A coupling factor of 1.6% is yielded for the current design. From equation (5.11), we can identify some design considerations that would affect the coupling factor. Firstly, the transmission line inductance L_0 is directly related to its length, thickness, and line width. To fully contain the sphere inside the substrate, the substrate must be thicker, which is 0.51 mm. This thickness effectively increases the inductance of the grounding via. Secondly, the sphere does not occupy the entire closed flux region, as shown in Fig. 5.5. Hence, its contribution to the overall inductance is obscured. A better design can improve the current coupling by optimizing the excitation structure or using planar material for a closed flux. In addition, it is worth noticing that the feeding part doesn't affect the coupling factor because it can be de-bedded. However, the grounding inductance will affect the coupling factor because it's part of the resonator design.

5.3 Modeling and Design of Bandpass Filters Built With BaM Spheres

With the design of a resonator, it is convenient to move forward to the design of a filter by coupling several resonators together. Both bandstop and bandpass filters can be realized, and the process for designing a bandpass filter is delineated in the section.

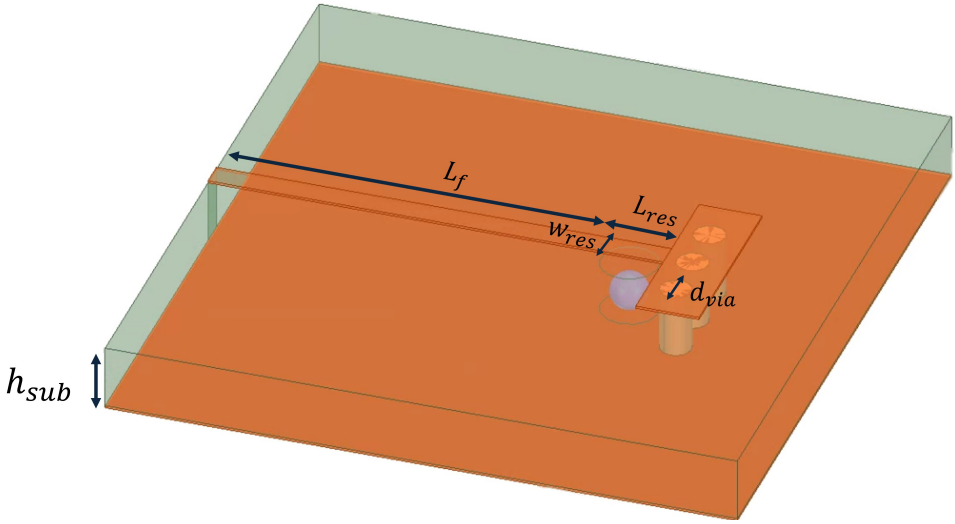

Figure 5.13: Design parameters to optimize the resonator. d_{via} is the diameter of grounding vias. L_{res} is the length of the transmission line at the effective resonator region. w_{res} is the width of the transmission line. h_{sub} is the substrate thickness. L_f is the length of the feed-in, but it doesn't affect the effective resonator performance.

5.3.1 Optimize Resonator Topology for a High Coupling Factor

The coupling factor defined in the previous section indicates how efficiently energy can be coupled to excite resonances in ferrites through the excitation of electromagnetic waves. When coupling several resonators to build a filter, the coupling factor will affect the filter insertion loss at the passband. Hence, it is desirable to optimize the resonator topology for a good coupling factor before proceeding to the filter design. Fig. 5.13 shows several physical parameters that can be optimized. d_{via} is the diameter of grounding vias. L_{res} is the length of the transmission line at the effective resonator region. w_{res} is the width of the transmission line. h_{sub} is the substrate thickness. L_f is the length of the feed-in, but it doesn't affect the effective resonator performance. The best design with fabrication considerations in mind yields a coupling factor of 1.6% when $w_{res} = 0.2mm$, $L_{res} = 0.6mm$, $d_{via} = 0.5mm$, and $h_{sub} = 0.51mm$. The effects of device parameters are included below.

Table 5.2: Effect of conductor width

w_{res}	$\Delta R'_m$	$\Delta L'_m$	$\Delta C'_m$	L'_0	C'_0	c
0.2mm	$100Ohm$	$2.0e^{-12}H$	$7.1e^{-12}F$	$1.3e^{-10}H$	$9.028e^{-15}F$	1.5%
0.6mm	$60Ohm$	$8e^{-13}H$	$1.84e^{-11}F$	$8.25e^{-11}H$	$1.391e^{-14}F$	1.0%
1.0mm	$50Ohm$	$6e^{-13}H$	$2.44e^{-11}F$	$6.65e^{-11}H$	$1.977e^{-14}F$	0.9%
1.4mm	$30Ohm$	$4e^{-13}H$	$3.67e^{-11}F$	$5.65e^{-11}H$	$2.558e^{-14}F$	0.7%

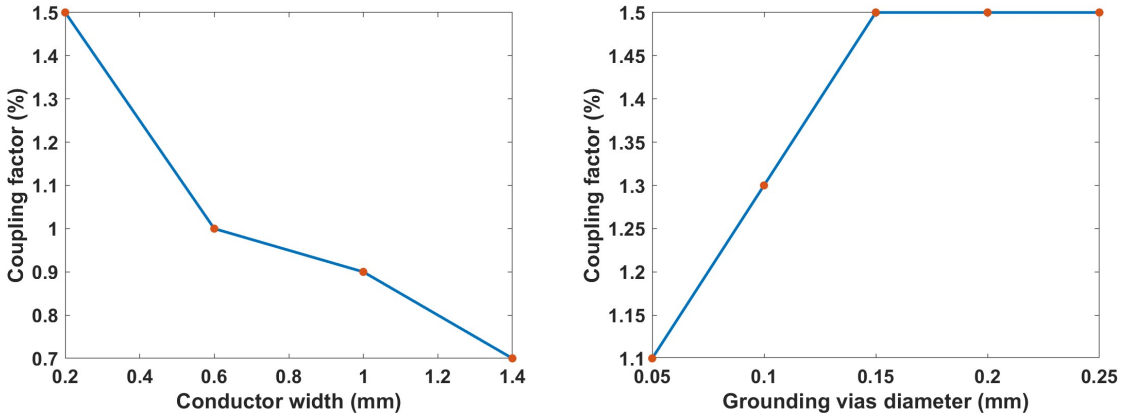

(a) (b)

Figure 5.14: Effect of (a) conductor width and (b) grounding vias' diameter on the coupling factor.

5.3.1.1 Effect of Conductor Width

The center conductor width w_{res} affects both the ferrite inductance $\Delta L'_m$ and the transmission line inductance L'_o. Table 5.2 summarizes the inductors' values, and the corresponding coupling factors are plotted in Fig. 5.14(a). From Table 5.2, both $\Delta L'_m$ and L'_o decrease with the width increasing. The former is because the ferrite sphere occupies a smaller percentage of the magnetic flux with the width increasing. From Fig. 5.5(b), L_m will be obscured when $\beta > \alpha$, leading to a smaller $\Delta L'_m$. The latter is because the transmission line yields a smaller characteristic impedance and self-inductance when w_{res} increases. The resulting

Table 5.3: Effect of grounding vias' diameter

d_{via}	$\Delta R'_m$	$\Delta L'_m$	$\Delta C'_m$	L'_0	C'_0	c
0.25mm	$100Ohm$	$2.0e^{-12}H$	$7.1e^{-12}F$	$1.3e^{-10}H$	$9.028e^{-15}F$	1.5%
0.20mm	$100Ohm$	$2.1e^{-12}H$	$7.1e^{-12}F$	$1.35e^{-10}H$	$9.41e^{-15}F$	1.5%
0.15mm	$100Ohm$	$2.1e^{-12}H$	$7.1e^{-12}F$	$1.395e^{-10}H$	$9.688e^{-15}F$	1.5%
0.10mm	$100Ohm$	$2.1e^{-12}H$	$7.1e^{-12}F$	$1.595e^{-10}H$	$1.108e^{-14}F$	1.3%
0.05mm	$100Ohm$	$2.1e^{-12}H$	$7.1e^{-12}F$	$1.945e^{-10}H$	$1.351e^{-14}F$	1.1%

coupling factor, on the other hand, increases as w_{res} decreases. It is worth noticing that a similar conclusion arrived in [46], where a high-impedance CPW line is used to couple energy effectively to the BaM sphere. The data in Table 5.2 is generated with a grounding vias' diameter d_{via}=0.25mm based on microstrip line excitation.

5.3.1.2 Effect of Grounding Vias' Diameter

The grounding vias act as an inductor whose inductance is primarily dominated by their diameters d_{via}. With an equivalent circuit representation shown in Fig. 5.12, this extra inductance will be added on top of the transmission line inductance and affect the effective air inductance for the resonator, i.e., L'_0. Table 5.3 and Fig. 5.14 (b) show the influence of via diameters on the coupling factors. The coupling factor decreases with the via diameter decreasing because of a greater L'_0. The data in Table 5.3 is generated with a conductor width w_{res}=0.2mm based on microstrip line excitation.

5.3.1.3 Effect of Transmission Line Topology

Transmission line topology also plays an important role in the coupling factor. A CPW line is used as an example. Fig. 5.15(a) shows the 3D view of the CPW line resonator under the same biasing field in the Z-direction. Fig. 5.15 (b) shows the top view, and it can be seen

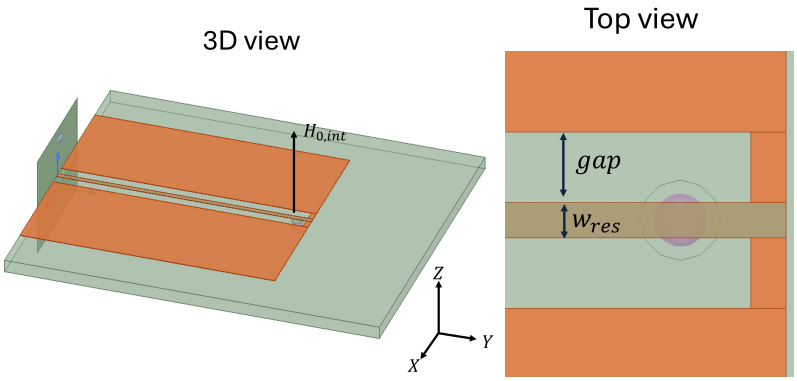

(a) (b)

Figure 5.15: (a) 3D view and (b) top view of the CPW line resonator.

Table 5.4: Effect of transmission line topology

Topology	$\Delta R'_m$	$\Delta L'_m$	$\Delta C'_m$	L'_0	C'_0	c
MLIN	$100Ohm$	$2.0e^{-12}H$	$7.1e^{-12}F$	$1.3e^{-10}H$	$9.028e^{-15}F$	1.5%
CPW	$30Ohm$	$8e^{-13}H$	$1.86e^{-11}F$	$9.95e^{-11}H$	$1.345e^{-14}F$	0.8%

that the BaM sphere is placed near the short end. Table 5.4 compares the extracted circuit parameters for the microstrip line (MLIN) and CPW line (CPW) when the conductor width w_{res} is fixed at 0.2mm. The transmission line inductance L'_0 is smaller for the CPW case under the short grounding path. However, the ferrite inductance $\Delta L'_m$ is also smaller since the magnetic field is concentrated near the conductor plane, which does not interact with the sphere as much, which is embedded inside the substrate. The resulting coupling factor c is also smaller for the CPW case.

A resonator design using BaM films under IC technology can potentially exceed a coupling factor of 5%, and the details are included in Appendix B and [106].

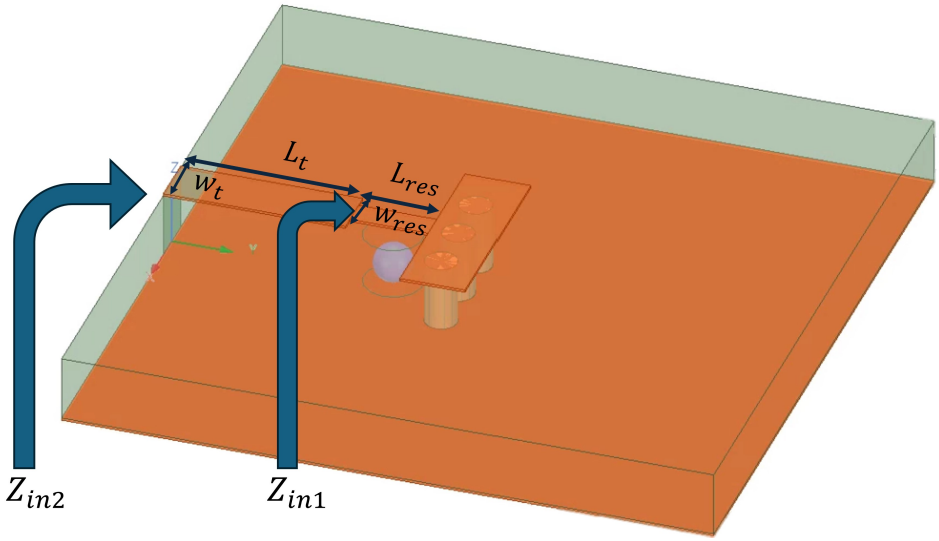

Figure 5.16: Tune input impedance of the resonator by adding another transmission line with length L_t and width w_t.

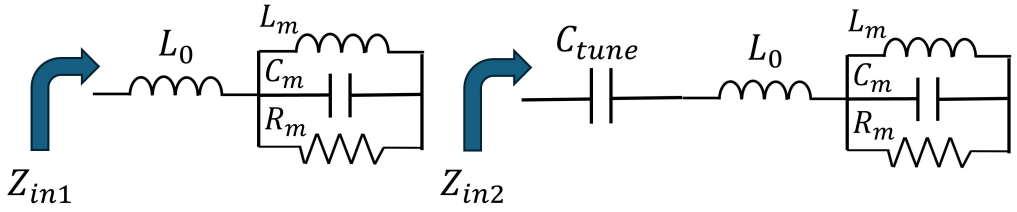

(a) (b)

Figure 5.17: Input impedance of (a) the effective resonator. (b) after adding a transmission line or capacitor.

5.3.2 Add Tuning Transmission Line or Capacitor

Due to the small coupling factor, the transmission line inductance has a great impact on the ferrite resonator. In other words, the input impedance of the effective resonator, i.e., Z_{in1} in Fig. 5.16, does not look like that of a parallel RLC resonator. On the other hand, microwave filter theory requires that several RLC resonators be coupled together. Hence, action must be taken to 'eliminate' the effect of the transmission line inductance L_0, at least in a narrow

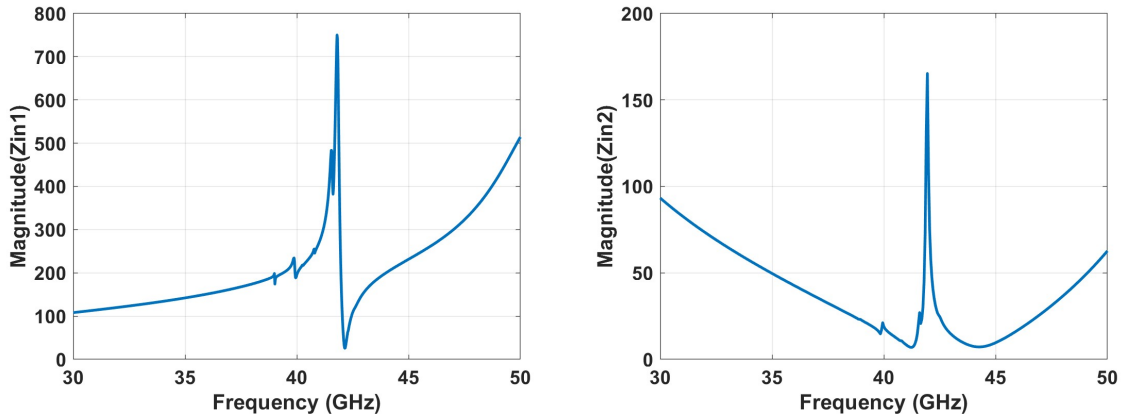

(a) (b)

Figure 5.18: Magnitude of the input impedance of (a) effective resonator (b) after adding a transmission line or capacitor.

frequency band.

As shown in Fig. 5.16, an extra transmission line of length L_t and width w_t is added to the effective resonator with design parameters fixed from the previous step. The input impedance of the effective resonator is denoted as Z_{in1}, while the input impedance after adding this extra transmission line is denoted as Z_{in2}. Fig. 5.17 illustrates the effect of this additional transmission line on the circuit equivalence. When $L_t > \frac{\lambda}{4}$, where λ is the electromagnetic wavelength inside the substrate, the transmission line behaves as a capacitor, i.e., C_{tune}. One can also construct a real capacitor rather than using a transmission line. Either way, this addition C_{tune} is chosen to form a series resonance with L_0 at the FMR frequency, as shown in Fig. 5.17 (b). In this way, the effect of L_0 is eliminated near the resonance.

Fig. 5.18 compares the magnitude of input impedance, i.e., $mag(Z_{in1})$ and $mag(Z_{in2})$. We can identify that $mag(Z_{in2})$ resembles that of a PRLC resonator near its center frequency of 42 GHz. Another intuitive understanding of such impedance conversion is that the extra line length L_t is chosen such that $L_t + L_{res} = \frac{\lambda}{2}$. This way, the input impedance of the

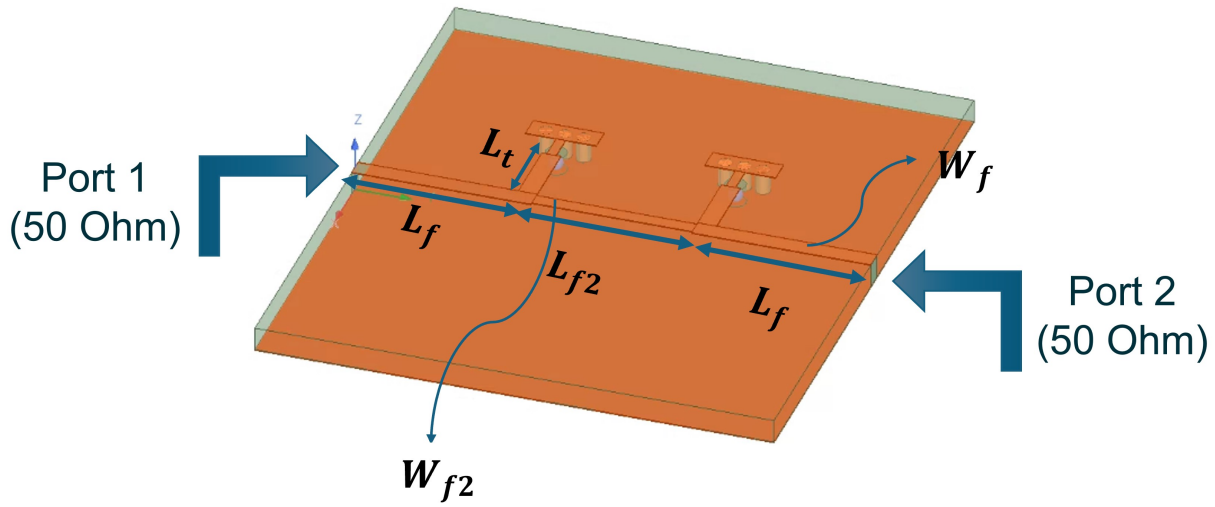

Figure 5.19: HFSS schematic of a two-pole bandpass filter.

$L_t + L_{res}$ transmission line is near zero at center frequency. When the ferrite is present, it adds to the zero impedance to behave as a parallel RLC circuit. In simulation, L_t and w_t are tuned to be $L_t = 1.4mm$ and $w_t = 0.4mm$.

5.3.3 Couple Resonators with Quarter-Wavelength Transmission Lines

After tuning L_t and w_t, the resonator branch is fixed. Then, two resonators can be coupled together through an admittance inverter to form a two-pole bandpass filter. Here, a quarter-wavelength transmission line acts as the admittance inverter, i.e., L_{f2} in Fig. 5.19. In fact, due to layout limits, the electrical length of L_{f2} is $\frac{3}{4}\lambda$ rather than $\frac{1}{4}\lambda$, while the effect remains the same. The feed-in line from the two ports has length L_f and width W_f, affecting the filter response. In practice, an initial value for L_f and W_f can be obtained from a circuit simulator like ADS. Then, these parameters are optimized in full-wave simulation HFSS to yield a good bandpass filter response. A sample bandpass filter response from the simulation is shown in Fig. 5.20. A narrow passband at 41.5GHz is obtained with the following device parameters: $L_f = 2.6mm$, $W_f = 0.2mm$, $L_{f2} = 3mm$, and $W_{f2} = 0.1mm$. We obtain a passband insertion loss (IL) of 5 dB, a 3-dB bandwidth of 260 MHz, and an out-of-band

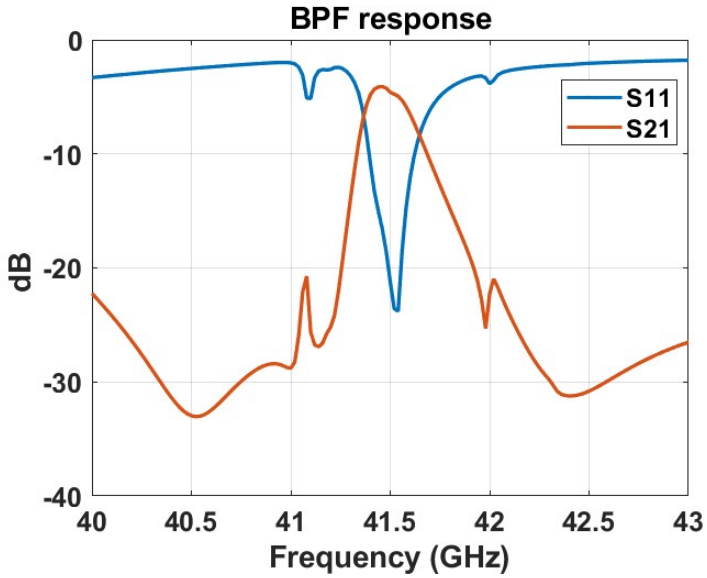

Figure 5.20: Simulated bandpass filter response S_{11} and S_{21}.

rejection of 35 dB.

5.3.4 Finialize Design Layout

Fig. 5.21 shows the finalized device layout. Compared with Fig. 5.19, it adds some extra feed-in line to allow for the device measurements with end-launch connectors. The feed-in line is designed to have a 50 Ohm characteristic impedance and corresponding tapers are also included. The through vias on the side of the board serve two functions. Firstly, they allow for the assembly of end-launch connectors at the edge. Secondly, they serve as alignment to integrate a fixture containing permanent bias magnets. The BaM spheres are contained in the blind via, marked in yellow. Similar to the resonator case, the feed-in can be de-embedded from the TRL calibration kits shown in Fig. 5.22.

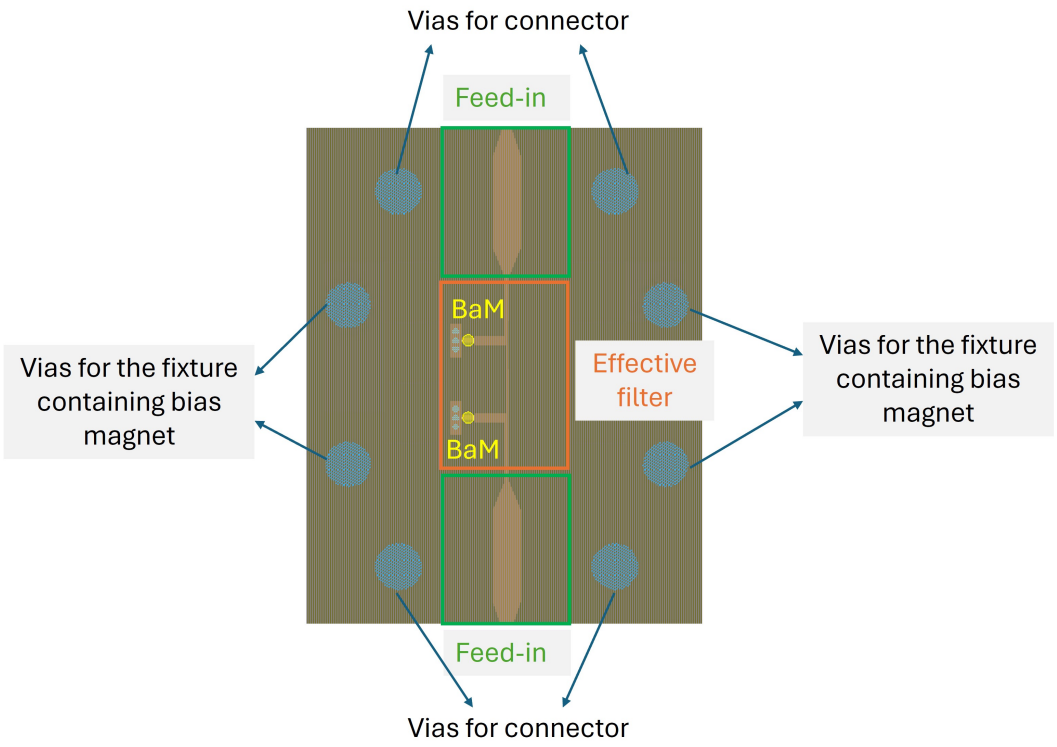

Figure 5.21: Finalized device layout for the filter.

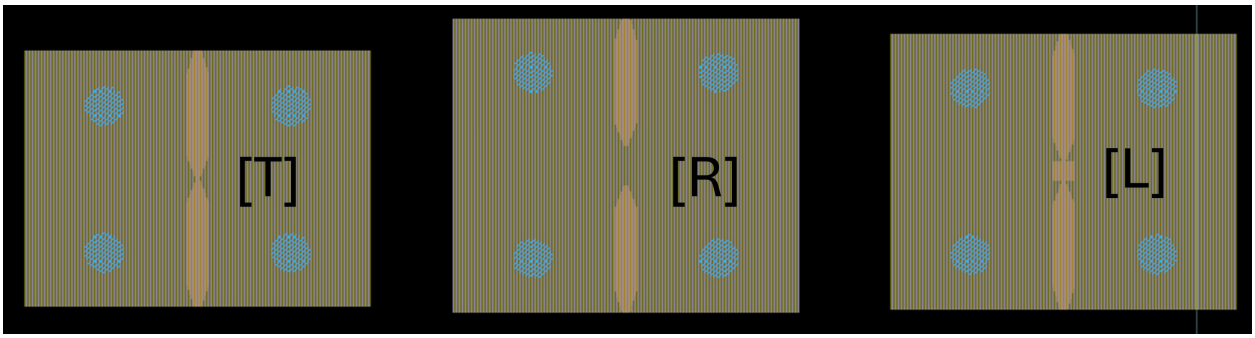

Figure 5.22: Layouts for the TRL calibration kits to obtain the feed-in S-parameter.

5.4 Measurement Results

5.4.1 Resonator

The proposed design of the BaM resonator is sent to an outside PCB manufacturer [105] for fabrication, and the front side and back side of the PCB after fabrication are shown in

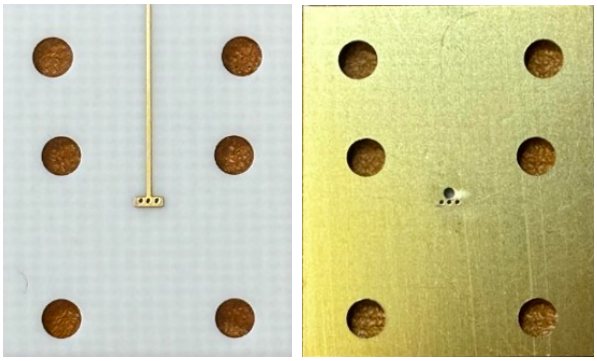

(a) (b)

Figure 5.23: (a) Front side of the fabricated PCB resonator. (b) Back side of the fabricated PCB resonator.

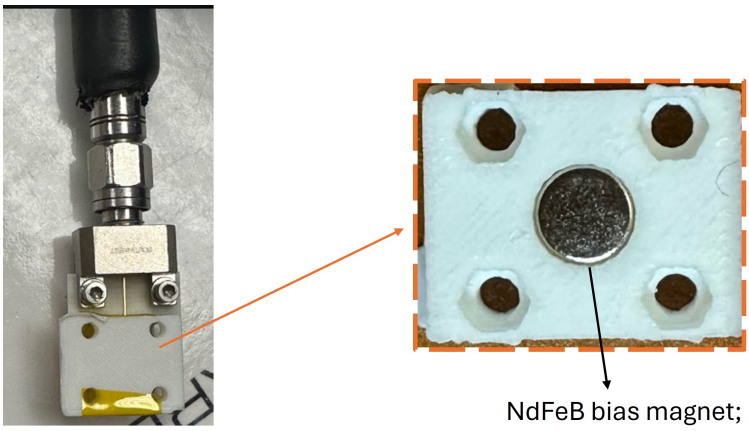

Figure 5.24: Assembly of the resonator with the bias magnet NdFeB, embedded inside a 3D-printed fixture.

Fig. 5.23. The BaM sphere is inserted inside the blind via, shown in Fig. 5.23(b). Fig. 5.24 shows the testing fixture with the end-launch connector and a 3D-printed part with an NdFeB bias magnet embedded inside.

The complete measurement setup is shown in Fig. 5.25. The resonator is a one-port device, while two-port measurements have been performed to calibrate the feeding line through the TRL technique, where two 1.85mm end-launch connectors are connected to the fabri-

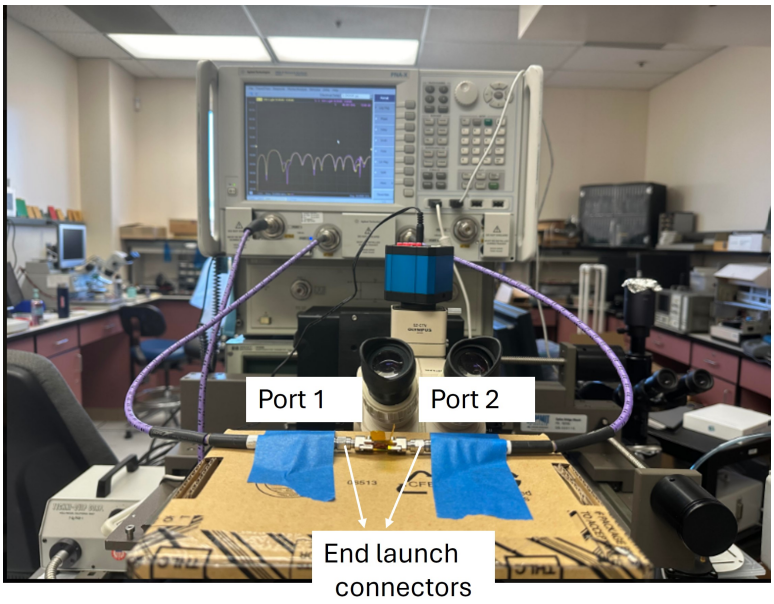

Figure 5.25: Measurement setup.

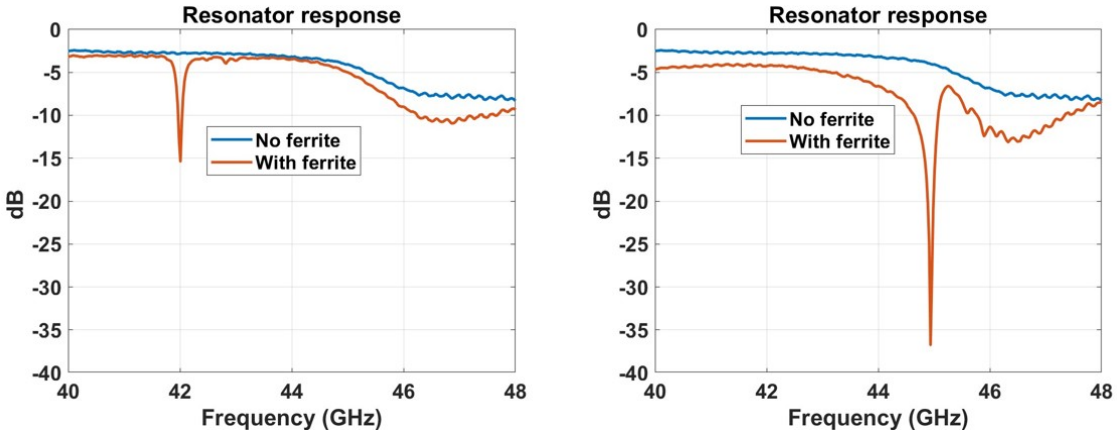

(a) (b)

Figure 5.26: $dB(S_{11})$ of the structure with and without the BaM sphere, showing an FMR frequency at (a) 42GHz and (b) 45GHz.

cated TRL kit. An N5247A PNA-X Microwave Network Analyzer is used to characterize the device's performance.

The measured resonator responses in terms of $dB(S_{11})$ are shown in Fig. 5.26. The

blue curves are the response when no BaM sphere is inserted inside the blind via, while the orange curves are the response when the BaM sphere is inside the blind via. By changing the separation between the external bias magnet and the PCB board, a resonant frequency tunability can be achieved, where Fig. 5.26(a) exhibits an FMR frequency of 42 GHz and Fig. 5.26(b) exhibits an FMR frequency at 45 GHz.

5.4.2 Filter

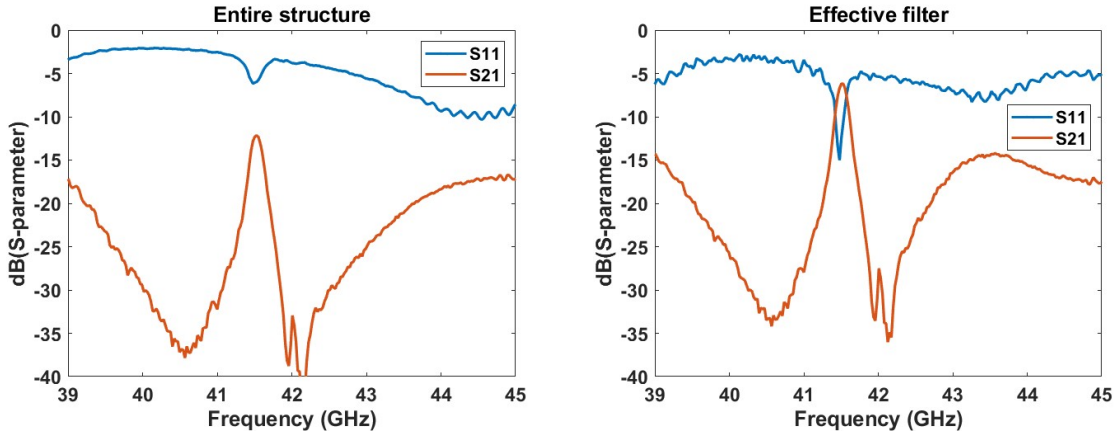

(a) (b)

Figure 5.27: $dB(S_{11})$ and $dB(S_{21})$of the bandpass filter of (a) the entire structure and (b) the de-embedded structure (effective filter).

Fig. 5.27 (a) shows a measured bandpass filter response. The de-embedded response after TRL measurements is shown in Fig. 5.27 (b) with a center frequency of 41.5 GHz. The passband insertion loss is 12 dB before de-embedding and 6 dB after de-embedding. The 3 dB bandwidth is around 240 MHz.

A comparison between simulation results and measurement results is shown in Fig. 5.28. Apart from the main resonance mode at 41.5 GHz, high-order magnetostatic modes, emphasized by the smaller dips in S_{11} plot, can also be seen, and a close match between simulation and measurements is observed. The radiation and conduction losses cause the S_{11} discrep-

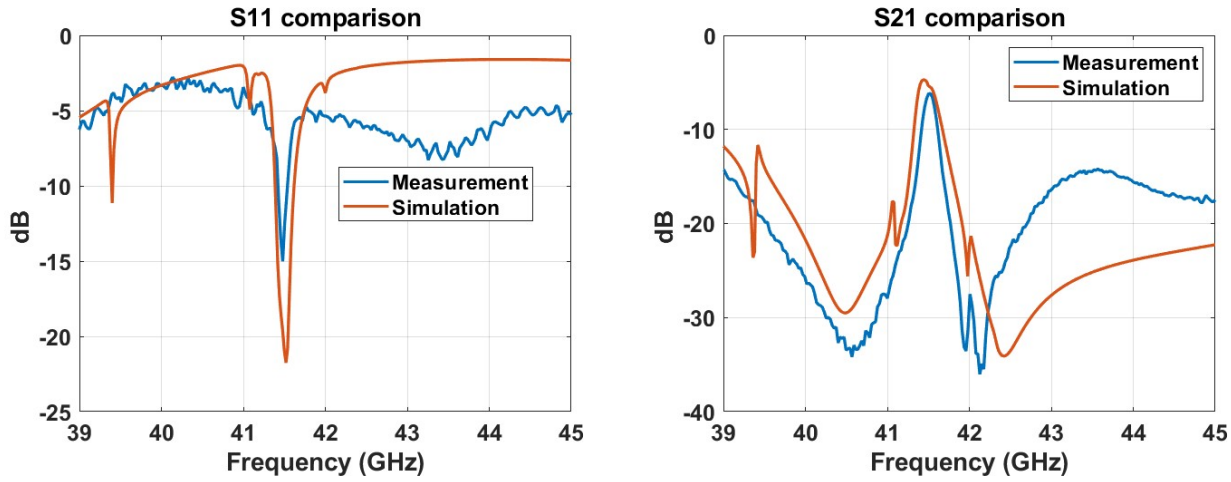

(a) (b)

Figure 5.28: (a) Comparison of $dB(S_{11})$ between simulation from HFSS and measurements. (b) Comparison of $dB(S_{21})$ between simulation from HFSS and measurements.

ancy during measurement.

5.5 Conclusion

This chapter has comprehensively explored the modeling and design of millimeter-wave resonators and filters based on hexagonal ferrite materials. The key motivations for this research stem from the need to extend the capabilities of current microwave magnetic devices into the millimeter-wave range, which holds promise for a wide array of high-frequency applications.

The chapter began by discussing the background and the critical need for advancements in magnetic resonators and filters. It was highlighted that traditional methods using YIG spheres have limitations in the frequency range and performance, thus driving the exploration of alternative materials like hexagonal ferrites. These materials offer higher anisotropy fields and lower losses, making them suitable for millimeter-wave applications.

A systematic design approach was introduced, optimizing resonators for better energy coupling coefficients. The equivalent circuit model for BaM sphere resonators was detailed,

providing a theoretical foundation for the design process. This model allows for accurate resonator performance predictions by incorporating hexagonal ferrites' unique properties.

The design and modeling of bandpass filters were also covered, demonstrating how multiple resonators can be coupled to achieve the desired filtering characteristics. The chapter included practical aspects of the design, such as layout considerations and the use of TRL calibration for accurate measurement and de-embedding of feeding line effects.

Experimental results validated the proposed designs, showing good agreement with simulation results and highlighting the effectiveness of the design methodology. The fabricated devices exhibited desirable characteristics such as high coupling factors, small form factors, and tunable frequency responses, confirming the potential of hexagonal ferrite-based resonators and filters in millimeter-wave applications.

In conclusion, this chapter lays the groundwork for future innovations in millimeter-wave magnetic devices. The proposed models and design techniques provide a robust framework for further research and development, aiming to push the boundaries of what is achievable with magnetic resonators and filters in high-frequency regimes.

CHAPTER 6

Conclusion

In this dissertation, we have explored the modeling and design of RF magnetic devices utilizing an equivalent circuit representation of spin dynamics. The comprehensive studies and innovations presented have significantly enhanced the understanding and capabilities in this field, leading to new methodologies for applying RF magnetic devices in various technologies.

6.1 Summary of Contributions

The thesis commenced with an investigation into the quantum mechanical foundations of magnetism, particularly focusing on electron spins within ferrimagnetic materials. From these foundational theories, we developed several robust equivalent circuit models that effectively translate micromagnetic behaviors into an intuitive circuit framework. These models encompass both linear and nonlinear cases, thereby broadening their applicability to various RF magnetic devices.

Subsequent chapters demonstrated the practical implementation of these models in the design and simulation of frequency-selective limiters (FSLs) and millimeter wave resonators and filters. The physics-based equivalent circuits integrated dynamic spin precession with spin wave propagation theories, enhancing the understanding of interactions between electromagnetic and spin waves within these devices. Furthermore, the design of millimeter wave resonators using hexagonal ferrite spheres marked a significant advancement, showcasing the

models' effectiveness through experimental validations, which confirmed their accuracy and utility.

6.2 Future Research Directions

While this research has taken substantial strides in the modeling and design of RF magnetic devices, the evolving nature of technology and materials science presents continuous opportunities for further exploration. Future work could focus on:

- Scalability and fabrication: Addressing challenges related to the scalability of the proposed models and their adaptation to industrial manufacturing processes.
- Enhancing model accuracy: Further refinement of the equivalent circuit models to include two-dimensional propagation of magnetostatic waves, i.e., forward / backward volume waves.
- Exploring new materials: Investigating the use of emerging magnetic materials that may offer better performance or unique properties for specific applications.

6.3 Concluding Remarks

The research conducted in this dissertation has laid a strong foundation for the enhanced understanding and application of RF magnetic devices. The developed equivalent circuit models serve as a tool for better design and bridge a significant gap in the intuitive understanding of complex magnetic behaviors at the microscale. It is hoped that the insights and methodologies developed herein will inspire further research and innovation in the field of RF magnetic devices.

Appendix A

Simplify Periodic Circuit for Broadband Simulation of CPW-FSL

As pointed out in Table 4.3, the damping constants and effective bias fields used for broadband simulations are made different. The derivations are included in this section.

The modeling of exchange coupling spin waves requires another division along the thickness direction in addition to the original thickness division for field nonuniformity. As a result, broadband simulation with periodic circuits will be much more time-consuming compared with the model without considering field nonuniformity.

To reduce computation time, we can simplify the periodic circuit with L_c added between adjacent spin units (RLC resonators in the linear case), as shown in Fig. A.1 (a). Several observations are made while the signal propagates along this periodic circuit. First, when the signal frequency is the same as the resonant frequency of parallel resonators, voltage polarities across L_c are the same. Hence, L_c is effectively open-circuited, having no impact on the circuit. As a result, N_d resonators can be combined into a single resonator at this particular frequency. On the other hand, at the cutoff frequency, which is the highest signal frequency that can propagate through this periodic circuit, voltage polarities across L_c are opposite. Therefore, the middle of L_c is effectively grounded. As shown in Fig. A.1 (b), an effective $L_c/4$ is in shunt with the original resonator due to the grounding and the parallel connection of two $L_c/2$. Consequently, the circuit can also be simplified to form a single RLC resonator in Fig. A.1 (c). For these two frequencies, no thickness division is needed, and the computation time can thus be significantly reduced. The modified RLC values at

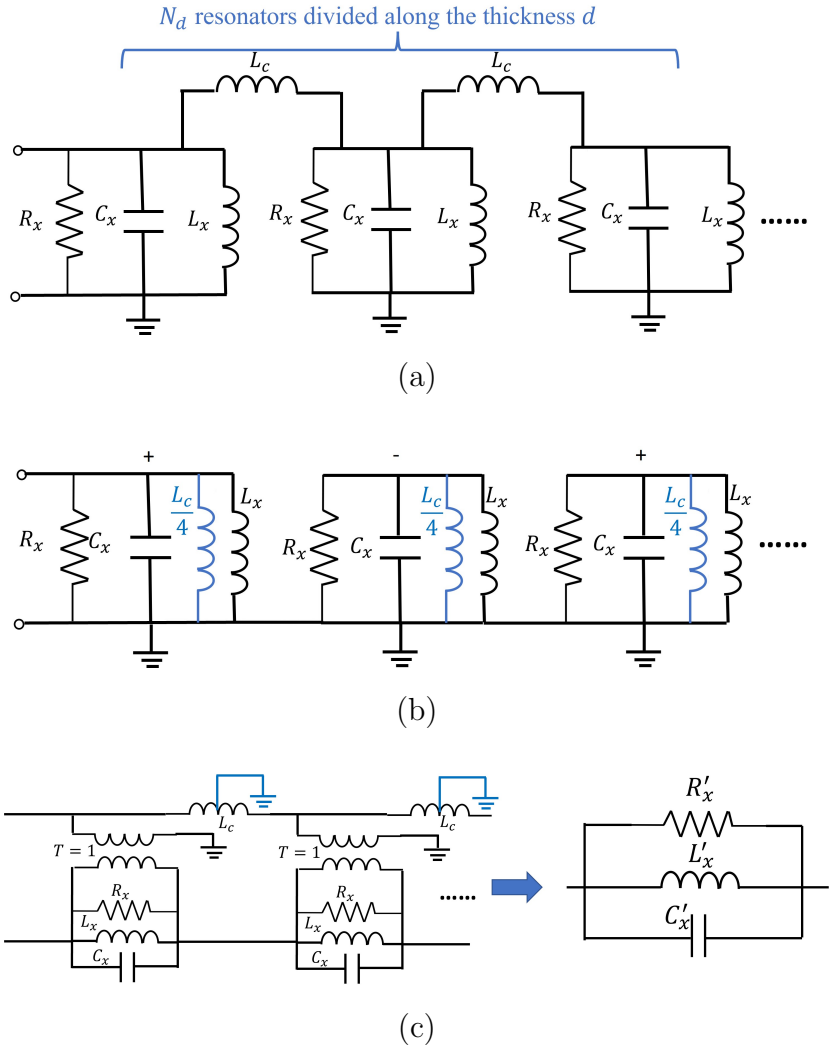

Figure A.1: (a) Equivalent circuit for exchange spin wave propagation perpendicular to the bias direction with exchange inductor L_c. (b) The equivalent circuit at the cutoff frequency, where $L_c/4$ is effectively in shunt with the original RLC resonator. (c) Equivalent circuit at cutoff frequency where N_d resonators are merged into one resonator.

the cutoff frequency are listed below:

$$\begin{cases} R'_x = N_d \times R_x = \mu_0 \dfrac{\omega_m\left(\omega_m+\omega_0\right)}{\alpha\left(2\omega_0+\omega_m\right)} \dfrac{\left(N_d \times y_c\right) z_c}{x_c} \\ L'_x = N_d \times \left(L_x \| \dfrac{L_c}{4}\right) \\ C'_x = \dfrac{C_x}{N_d} = \dfrac{1}{\mu_0\left(\omega_m+\omega_0\right)\omega_m} \dfrac{x_c}{\left(N_d \times y_c\right) z_c}. \end{cases} \tag{A.1}$$

Note that due to the addition of the $L_c/4$, the resonant frequency of the RLC resonator increases, which is the cutoff frequency. Moreover, the quality factor also changes to be

$$Q = \omega_r R'_x C'_x = \frac{\sqrt{(\omega_m + \omega_0)\,\omega_m}}{\alpha\,(2\omega_0 + \omega_m)\,.} \tag{A.2}$$

As a result, broadband simulation can be performed by adjusting the resonance frequency and quality factor of the RLC resonators through changing effective bias fields and damping constants. For each frequency higher than 4 GHz ($2f_r$), L_c is chosen to provide a cutoff at that particular frequency. The resulting H_0 and α are summarized in Table 4.3.

Appendix B

BaM Resonators With Self-Biased Films

B.1 Device Structure

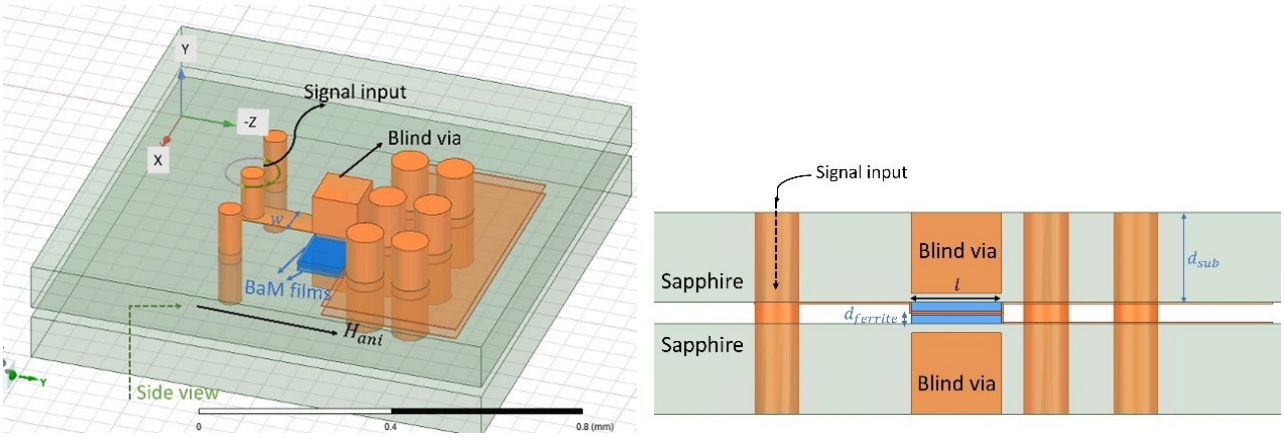

(a) (b)

Figure B.1: (a) Schematic of the ridge stripline ferrite resonator. The signal inputs from the top pad and its magnetic field will affect the top and bottom BaM films (in blue). The anisotropy field H_{ani} lies in the z direction. (b) Side view of the resonator structure. The substrate thickness is d_{sub}, and the ferrite thickness is $d_{ferrite}$.

The physical construction of the ferrite resonator based on thin-film BaM is shown in Fig. B.1. It consists of three parts: the actual resonator underneath the blind via, the feeding via plus the transmission line, and the grounding vias.

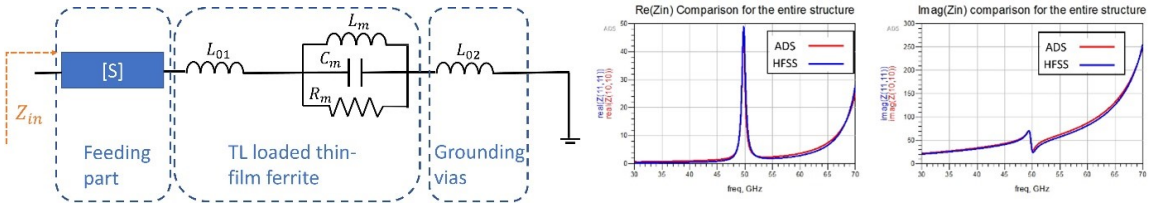

(a) (b)

Figure B.2: (a) Equivalent circuit model for the entire structure consisting of the feeding part, the TL-loaded thin-film ferrite, and the ground vias. (b) Comparison of the real part of input impedance and imaginary part of input impedance between HFSS simulation results (blue curves) and ADS circuit simulation results (red curves).

B.2 Equivalent Circuit Model

The complete circuit model for the entire resonator structure can thus be constructed as in Fig. B.2(a), where the L_{o2} represents the inductance brought by the grounding vias, while L_{o1} represents the transmission line inductance within the resonator itself. In other words, L_{o1} can be engineered by designing a transmission line structure. For example, the ridge-strip line structure produces smaller L_{o1} compared with a conventional strip line of the same length and width because the effective thickness of the substrate becomes smaller. On the other hand, L_{o2} can be reduced by introducing more grounding vias with greater diameter. The detailed values of L_{o1} and L_{o2} are listed in the next Section.

B.3 Effect of Design Parameters

The ridge strip line structure in Fig. B.1(a) is implemented and simulated in HFSS, where BaM thin films of thickness $d_{ferrite}$ are placed on top of 100 um thick sapphire wafers. The BaM film has a magnetization saturation $M_s = 3700Gauss$ $\Delta H = 300Oe$ measured at 60 GHz. A static magnetic bias field models its anisotropy magnetic fields inside with $H_0 = 1286000A/m$ to set the FMR frequency at 50 GHz. Through vias are created to feed

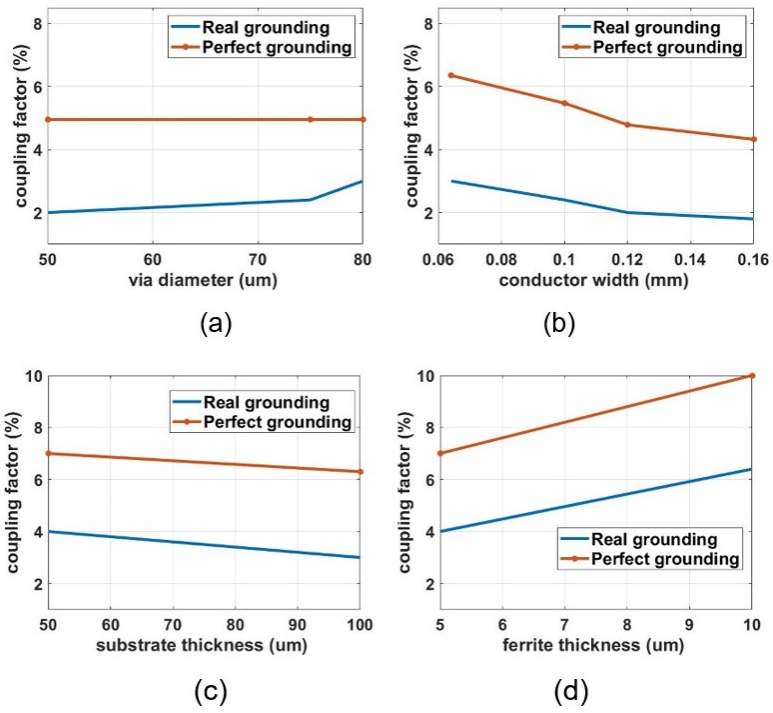

Figure B.3: Plots of coupling factors versus (a) grounding via diameter, (b) conductor width, (c) substrate thickness, and (d) ferrite thickness. The blue curves are coupling factors with grounding parasitic, while the red dotted curves assume perfect groundings.

the signal from the top of the device and ground the trace after ferrites. Fig. B.1(b) is the side view of the structure, where the blind vias effectively move the ground planes closer to the ferrite film to increase energy coupling factor compared with conventional strip line structure.

The equivalent circuit model was extracted following the procedure described in the previous section. The influencing factors on the coupling factor c are described in this section.

B.3.1 Effect of Grounding Vias' Diameter

Fig. B.3(a) shows the influence of via diameters on the coupling factors. With the via diameter increasing, the coupling factor also increases by virtue of a smaller L_{o2}. The dotted line is the coupling factor with perfect grounding, i.e., assuming $L_{o2} = 0$. Though it's not achievable with the current limit on the device form factor, it emphasizes the effect of the grounding parasitic on the design process. The data in Fig. B.3(a) is generated with ferrite thickness $d_{ferrite}$=5um, conductor width w_{cond}=0.12mm and substrate thickness $d_{sub} = 100um$.

B.3.2 Effect of Conductor Width

Both L_m and L_{o1} decrease with the width increasing, while L_{o2} stays relatively constant since it is mainly contributed by the grounding vias, whose diameter is fixed to be 50um for all these cases. Fig. B.3(b) calculates and plots the resulting coupling factors. Like Fig. B.3(a), the curve with perfect grounding ($L_{o2} = 0$) is also plotted for comparison. The data is generated with ferrite thickness $d_{ferrite} = 5um$ and substrate thickness $d_{sub} = 100\mu m$.

B.3.3 Effect of Substrate Thickness

Besides grounding vias' diameter, substrate thickness also affects the coupling factor by changing L_{o2}. Of course, the thinner substrate has less parasitic, i.e., smaller L_{o2}. Specifically, the coupling factors are simulated for $d_{sub} = 100\mu m$ and $d_{sub} = 50\mu m$ cases and plotted in Fig. B.3(c). The other parameters are fixed to be ferrite thickness $d_{ferrite} = 5\mu m$, $w_{cond} = 0.064mm$, and $D_{via} = 50\mu m$.

B.3.4 Effect of Ferrite Thickness

ferrite thickness $d_{ferrite}$ affects ferrite inductance L_m. In addition, when $d_{ferrite}$ changes, L_{o1} also changes because L_{o1} is the transmission line inductance corresponding to the $d_{ferrite}$ region. In general, though, coupling factor c increases as $d_{ferrite}$ increases, as depicted in Fig. B.3(d). Notably, the coupling factor with perfect grounding reaches as large as 10% when $d_{ferrite} = 10\mu m$. The other simulation parameters are $d_{sub} = 50\mu m$, $w_{cond} = 0.064mm$, and $D_{via} = 50\mu m$.

B.4 Fabrication Procedure

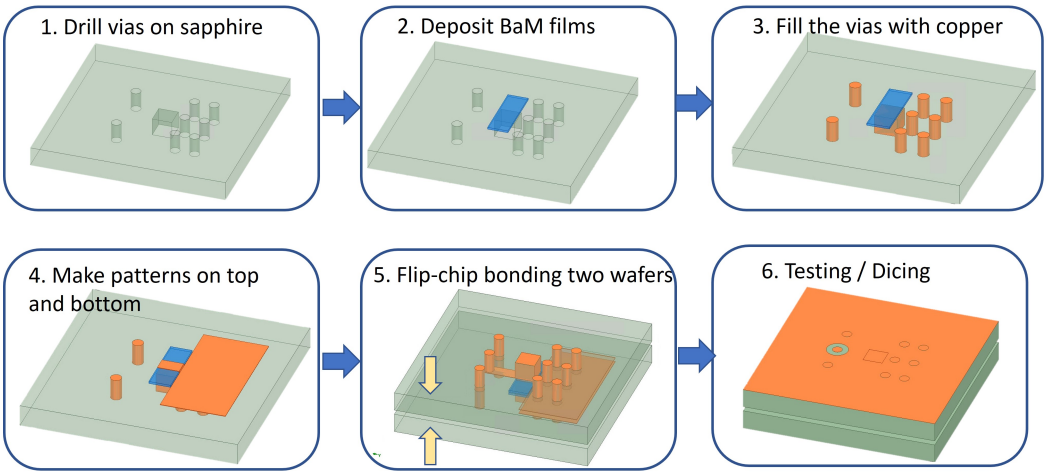

Figure B.4: Proposed fabrication procedure of BaM resonators built with self-biased thin film.

Fig. B.4 illustrates the proposed fabrication of BaM resonators with thin films. The substrate material is sapphire for the BaM film to be deposited. Firstly, blind vias and through vias are drilled on the bare substrate. Conventionally, etching machines have to be used for such via formation. However, because the ratio between the via opening versus the substrate thickness is small (50um/100um), such etching is challenging, provided that sapphire is a 'hard' material. Hence, we devised a novel way of etching vias utilizing laser

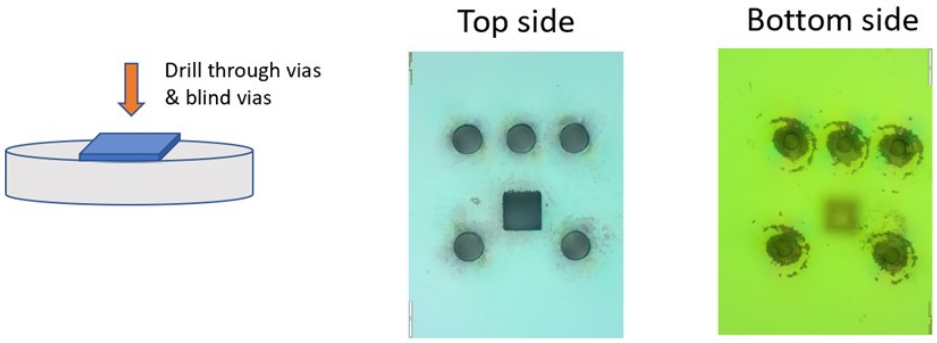

Figure B.5: Vias after laser drilling.

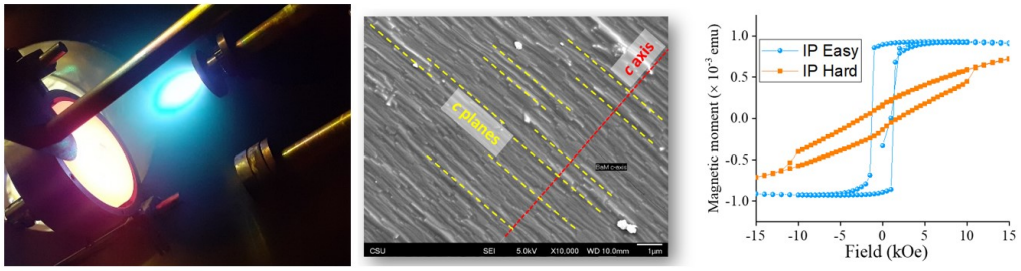

Figure B.6: BaM films through PLD growth. (a) PLD machine. (b) BaM film of thickness 250 nm with c axis as shown. (c) Measured hysteresis loop of the BaM film. Courtesy of Prof. Mingzhong Wu's group.

machines. The laser parameters are fine-tuned to create blind vias and through vias with well-defined shapes.

Fig. B.5 shows some figures of the substrate's top and bottom sides after laser drilling. Blind vias are formed because they can only be seen from the top side of the substrate.

After laser drilling, BaM films have to be grown on the substrate and confined to the blind via region. To do this, our collaborator from Prof. Mingzhong Wu's group needs to deposit films over the entire substrate and then use photolithography to lift off the area that is not of interest. Fig. B.6 shows a sample BaM film through PLD (Pulsed Laser Deposition) and the corresponding hysteresis loop. The film exhibits a strong hard axis (along the c-

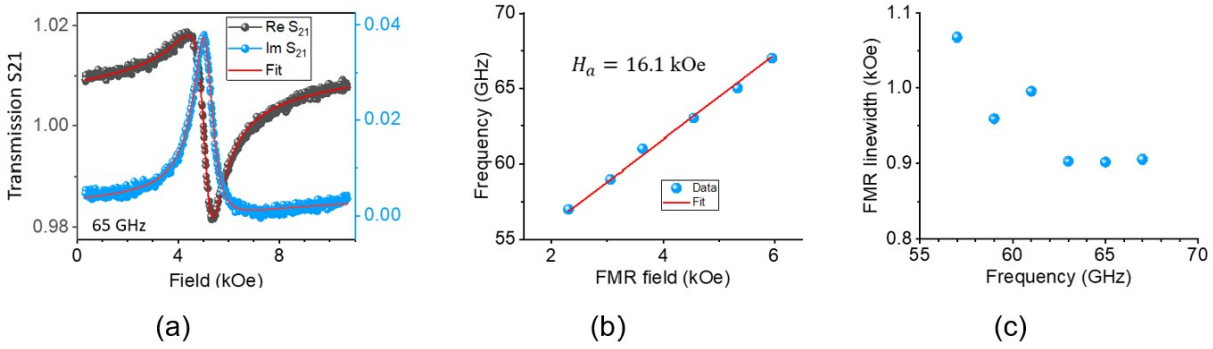

Figure B.7: BaM films electric measurements from Prof. Mingzhong Wu's group. (a) Transmission S21. (b) Resonant frequency versus applied field. (c) Extracted linewidth.

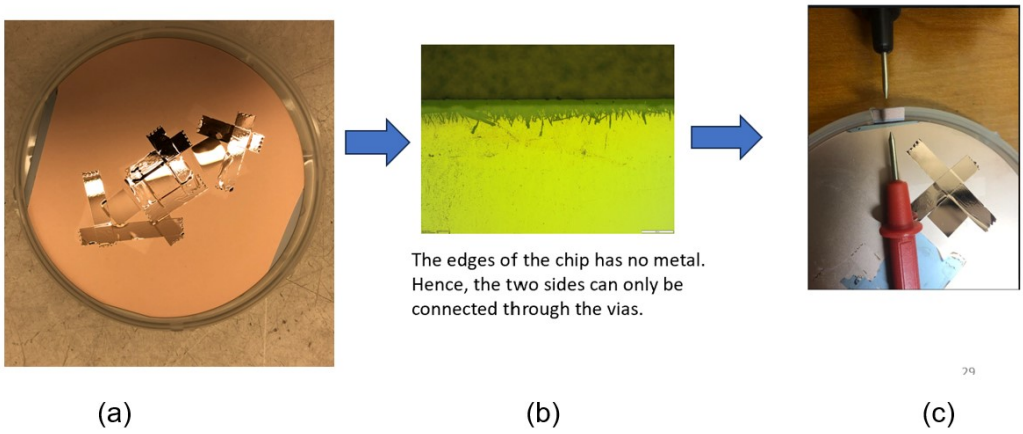

Figure B.8: Copper sputtering to fill the vias. (a) Samples during sputtering with sapphires attached on a carrier silicon wafer. (b) Figures under a microscope after sputtering. (c) Measure the electric resistivity after sputtering.

axis). Fig. 14 shows more measurements in terms of S21. Based on the measured resonant frequency and applied field, the anisotropy field is extracted to be 16.1 Koe. The linewidth is around 1 kOe.

After BaM film growth, copper sputtering is performed to connect both sides electrically. Fig. B.8(a) shows some sample sapphire substrates after sputtering. They are attached to a carrier silicon wafer and have been sputtered twice (on top side and bottom side). Fig. B.8

Step	Name	Recipe		
1	Sputter (Denton Discovery 550	C2_Ti (adhesion)+C4_Cu_AT Have 1um Cu on both sides		Test resistivity & Figures
2	Spin coating (with AZ 4620) *Just do once for one side; Use tape to protect the other side	Step 1: 4300 RPM (speed) 1000 RPM/s (ramp rate) 30 sec (time)	Step 2: 0 RPM (speed) 1000 RPM/s (ramp rate) 0 sec (time)	
3	Soft bake	110 C, 2~3min		Figures
4	Align, expose, and develop	Contact type: hard contact Expose time: 50 sec Gap size: 30 um Developer: AZ developer		
5	Hard bake	120 C, 3min		Figures
6	Wet etching	APS-100 etchant Time: 1~2 min		
7	Cleaning	Acetone + IPA+ water		Figures

Figure B.9: Lithography recipe.

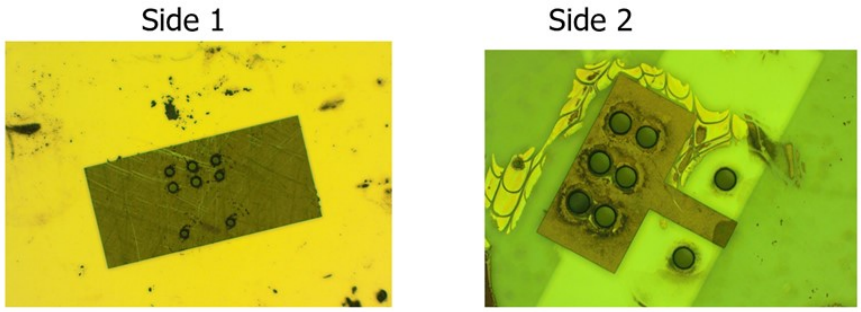

Figure B.10: Figures of patterns on both sides of the substrates after lithography.

(b) is a figure of the sapphire under the microscope after sputtering. Fig. B.8 (c) shows the process of testing the resistivity of the via by connecting the chip to a multimeter. If the copper successfully goes inside the drilled vias, the measured resistivity would be very low (less than one Ohm). In practice, we got a DC resistance of 0.6 Ohm, demonstrating our approach's feasibility.

After copper sputtering to fill the vias, photolithography forms patterns on both sides of the chip. A detailed recipe for such a process is again fine-tuned and experimented with more than five times to ensure a good pattern. Fig. B.9 summarizes the optimal recipe, and Fig. B.10 shows the patterns on both sides of the chip. One can identify that such patterns

are similar to the ones shown in the schematic plots (Fig. B.4, step 4).

REFERENCES

[1] Harris, Vincent G., et al. "Recent advances in processing and applications of microwave ferrites." Journal of Magnetism and Magnetic Materials, vol. 321, no. 14, 2009, pp. 2035-2047.

[2] Ü. Özgür, Y. Alivov and H. Morkoc, "Microwave ferrites, part 2: passive components and electrical tuning", J Mater Sci: Mater Electron (2009) 20:911–952 DOI 10.1007/s10854-009-9924-1.

[3] T. Kuribara, M. Yamaguchi and K. -. Arai, "Equivalent circuit analysis of an RF integrated ferromagnetic inductor," IEEE Transactions on Magnetics, vol. 38, no. 5, pp. 3159-3161, Sept. 2002, doi:10.1109/TMAG.2002.802400.

[4] E. N. Skomal, "Theory of Operation of a 3-Port Y-Junction Ferrite Circulator," IEEE Transactions on Microwave Theory and Techniques, vol. 11, no. 2, pp. 117-122, March 1963, doi: 10.1109/TMTT.1963.1125612.

[5] C. E. Fay and R. L. Comstock, "Operation of the Ferrite Junction Circulator," IEEE Transactions on Microwave Theory and Techniques, vol. 13, no. 1, pp. 15-27, January 1965, doi: 10.1109/TMTT.1965.1125923.

[6] E. K., N. Yung, R. S. Chen, K. Wu, and D. X. Wang, "Analysis and development of millimeter-wave waveguide-junction circulator with a ferrite sphere," IEEE Transactions on Microwave Theory and Techniques, vol. 46, no. 11, pp. 1721-1734, Nov. 1998, doi: 10.1109/22.734570.

[7] P. Shi, H. How, X. Zuo, S. D. Yoon, S. A. Oliver and C. Vittoria, "MMIC circulators using hexaferrites," IEEE Transactions on Magnetics, vol. 37, no. 4, pp. 2389-2391, July 2001, doi: 10.1109/20.951181.

[8] B. N. Enander, "A new ferrite isolator," Proceedings of the IRE, vol. 44, no. 10, pp. 1421-1430, Oct. 1956, doi: 10.1109/JRPROC.1956.274986.

[9] J. Uher and W. J. R. Hoefer, "Tunable microwave and millimeter-wave band-pass filters," IEEE Trans. Microw. Theory Techn., vol. 39, no. 4, pp. 643-653, April 1991.

[10] J. Helszajn, YIG Resonators and Filters (Wiley, New York, 1985)

[11] H. Tanbakuchi, D. Nicholson, B. Kunz and W. Ishak, "Magnetically tunable oscillators and filters," in IEEE Transactions on Magnetics, vol. 25, no. 5, pp. 3248-3253, Sept. 1989, doi: 10.1109/20.42268.

[12] Y-Y Song et al. and M. Wu, "Self-biased planar millimeter wave notch filters based on magnetostatic wave excitation in barium hexagonal ferrite thin films," Applied Physics Letters 97, 173502 (2010).

[13] S. Dai et al., "Octave tunable magnetostatic YIG resonators on a chip," IEEE Trans. Ultras, Ferro. and Freq. Control, 67(11) 2454-2460 (2020).

[14] D. Brown, J. L. Volakis, L. C. Kempel and Y. Botros, "Patch antennas on ferromagnetic substrates," IEEE Transactions on Antennas and Propagation, vol. 47, no. 1, pp. 26-32, Jan. 1999, doi: 10.1109/8.752980.

[15] G . Yang et al., "Tunable miniaturized patch antennas with self-biased multilayer magnetic films," IEEE Transactions on Antennas and Propagation, vol. 57, no. 7, pp. 2190-2193, July 2009, doi: 10.1109/TAP.2009.2021972.

[16] M. Sigalov, R. Shavit, R. Joffe, and E. O. Kamenetskii, "Manipulation of the radiation characteristics of a patch antenna by small ferrite disks inserted in its cavity domain," IEEE Transactions on Antennas and Propagation, vol. 61, no. 5, pp. 2371-2379, May 2013, doi: 10.1109/TAP.2013.2242830.

[17] V. G. Kononov, C. A. Balanis and C. R. Birtcher, "The impact of non-uniform bias field on the radiation patterns of ferrite-loaded CBS antennas," IEEE Transactions on Antennas and Propagation, vol. 61, no. 8, pp. 4367-4371, Aug. 2013, doi: 10.1109/TAP.2013.2259452

[18] K. L. Kotzebue, "Frequency-Selective Limiting in YIG Filters," Journal of Applied Physics 33, 747 (1962); https://doi.org/10.1063/1.1702502

[19] S. S. Elliott, "A Broadband Ferrite Limiter", AIP Conference Proceedings 18, 1273 (1974); https:// doi.org/10.1063/1.2947257.

[20] J. Brown, "Ferromagnetic limiters," Microw. J., vol. 4, pp. 74-79, Nov. 1961.

[21] P. R. Emtage and S. N. Stitzer, "Interaction of signals in ferromagnetic microwave limiters," IEEE Trans. Microw. Theory Techn., vol. 25, no. 3, pp. 210-213, Mar. 1977.

[22] J. Adam, "A broadband microwave signal to noise enhancer," IEEE Trans. Magn., vol. 16, no. 5, pp. 1168-1170, Sep. 1980.

[23] S. Stitzer, "Frequency selective microwave power limiting in thin YIG films," IEEE Trans. Magn., vol. 19, no. 5, pp. 1874-1876, Sep.1983.

[24] J. D. Adam and S. N. Stitzer, "Frequency selective limiters for high dynamic range microwave receivers," IEEE Trans. Microw. Theory Techn., vol. 41, no. 12, pp. 2227-2231, Dec. 1993.

[25] T. Nomoto and Y. Matsushita, "A signal-to-noise enhancer using two MSSW filters and its application to noise reduction in DBS reception," IEEE Trans. Microw. Theory Techn., vol. 41, no. 8, pp. 1316-1322, Aug. 1993.

[26] S. M. Gillette, M. Geiler, J. D. Adam, and A. L. Geiler, "Ferrite-based reflective-type frequency selective limiters," in Proc. IEEE MTT-S Int. Microw. Workshop Ser. Adv. Mater. Process. RF THz Appl. (IMWS-AMP), Ann Arbor, MI, 2018, pp. 1-3.

[27] Y. Cui et al., "Monolithic Integration of Self-Biased C-Band Circulator on SiC Substrate for GaN MMIC Applications," IEEE Electron Dev. LETTERS, Vol. 40, No. 8, Aug. 2019.

[28] V. H. Rumsey and W. L. Weeks, "Electrically small, ferrite loaded loop antennas," IRE Int. Conv. Rec., vol. 4, no. 1, pp. 165-170, Mar. 1966.

[29] R. DeVore and P. Bohley, "The electrically small magnetically loaded multiturn loop antenna," IEEE Trans. Antennas Propag., vol. 25, pp. 496-505, July 1977.

[30] J. McLean and R. Sutton, An efficient low profile antenna employing lossy magneto-dielectric materials. Presented at the 2012 IEEE International Workshop on Antenna Technology (iWAT). Available: DOI: 10.1109/IWAT.2012.6178662.

[31] T. Yousefi, T. Sebastian, and R. E. Diaz, "Why the magnetic loss tangent is not a relevant constraint for permeable conformal antennas," IEEE Trans. Antennas Propag., vol. 64, no. 7, pp. 2784–2796, July 2016. M. Wu and A. Hoffmann, "Ferrites for RF passive devices," in Solid State Physics, vol. 64, Oxford, U.K.: Academic, 2013, pp. 237–326.

[32] J. Lee, Y. K. Hong, S. Bae, G. S. Abo, W. Seong, and G. Kim, "Miniature Long-Term Evolution (LTE) MIMO Ferrite Antenna," IEEE Antennas Wireless Prop. Lett., vol. 10, pp. 603-606, June 2011.

[33] W. Lee, Y. K. Hong, J. Park, M. Choi, J. Lee, I. Baek, N. Hur and W. Seong, "Low-Profile Multiband Ferrite Antenna for Telematics Applications," IEEE Trans. Mag., vol. 52, no. 7, July 2016.

[34] H. Moon, G. Lee, C. Chen and John L. Volakis, "An Extremely Low-Profile Ferrite-Loaded Wideband VHF Antenna Design," IEEE Antennas Wireless Prop. Lett., vol. 11, pp. 322-325, Mar. 2012.

[35] L. Tan, R. Wu, C. Wang, and Y. Poo, "Ferrite-Loaded SIW Bowtie Slot Antenna with Broadband Frequency Tunability," IEEE Antennas Wireless Prop. Lett., vol. 13, pp. 325-328, Feb. 2014.

[36] G. M. Yang, A. Daigle, M. Liu, O. Obi, S. Stoute, K. Naishadham, and N. X. Sun, "Planar circular loop antennas with self-biased magnetic film loading," Electron. Lett., vol. 44, pp. 332–333, Feb. 2008.

[37] G.M. Yang, X. Xing, A. Daigle, M. Liu, O. Obi, S. Stoute, K. Naishadham, and N.X. Sun, "Tunable Miniaturized Patch Antennas with Self-Biased Multilayer Magnetic Films," IEEE Trans. Antennas Propag., vol. 57, no. 7, pp. 2190–2193, July 2009.

[38] J. D. Adam, L. E. Davis, G. F. Dionne, E. F. Schloemann, and S. N. Stitzer, "Ferrite devices and materials," in IEEE Transactions on Microwave Theory and Techniques, vol. 50, no. 3, pp. 721-737, March 2002, doi: 10.1109/22.989957.

[39] G. L. Matthei, "Magnetically tunable band-stop filters," IEEE Trans. Microwave Theory Tech., vol. MTT-13, pp. 203– 212, 1965.

[40] N. Cramer, D. Lucic, R. E. Camley, and Z. Celinski, J. Appl. Phys. 87, 6911 (2000).

[41] B. K. Kuanr, D. L. Marvin, T. M. Christensen, R. E. Camley, and Z. Celinski, Appl. Phys. Lett. 87, 222506 (2005).

[42] T. J. Fal and R. E. Camley, J. Appl. Phys. 104, 023910 (2008).

[43] Young-Yeal Song, César L. Ordóñez-Romero, Mingzhong Wu, Appl. Phys. Lett. 95, 142506 (2009).

[44] Sterns, Michael, et al. "Novel tunable hexaferrite bandpass filter based on open-ended finlines." 2009 IEEE MTT-S International Microwave Symposium Digest. IEEE, 2009.

[45] A. L. Nikytenko, L. V. Chevnyuk, V. I. Grygoruk, V. I. Kostenko and V. F. Romaniuk, "Tunable bandpass filter based on single-crystal platelet of BaFe12O19 in multidomain area," 2016 9th International Kharkiv Symposium on Physics and Engineering of Microwaves, Millimeter and Submillimeter Waves (MSMW), Kharkiv, Ukraine, 2016, pp. 1-3, doi: 10.1109/MSMW.2016.7538106.

[46] M. Sterns, D. Schneiderbanger, R. Rehner, S. Martius and L. -P. Schmidt, "Novel tunable hexaferrite bandpass filter based on rectangular waveguide coupled shielded coplanar transmission lines," 2008 IEEE MTT-S International Microwave Symposium Digest, Atlanta, GA, USA, 2008, pp. 1039-1042, doi: 10.1109/MWSYM.2008.4633013.

[47] J. D. Adam, S. N. Stitzer, and R. M. Young, "UHF frequency selective limiters," in IEEE MTT-S Int. Microwave Symp. Dig., vol. 01, 2001, pp. 1174–1175.

[48] S. N. Stitzer, H. Goldie, J. D. Adam, and P. R. Emtage, "Magnetostatic surface wave signal-to-noise enhancer," in IEEE MTT-S Int. Microwave Symp. Dig., 1980, pp. 238–240.

[49] T. Kuki and T. Nomoto, "A reflection type of MSW signal-to-noise enhancer in the 400 MHz band," in IEEE MTT-S Int. Microwave Symp. Dig., vol. 95, 1995, pp. 111–114.

[50] Ansys Corporation, "Electronics Desktop," 2017, Suite v18, Pittsburgh (PA), USA.

[51] Object Oriented Micromagnetic Framework (OOMMF). [online]. Available: https://math.nist.gov/oommf/

[52] M. J. Donahue and D. G. Porter, OOMMF User's guide. US Department of Commerce, Technology Administration, National Institute of Standards and Technology, 1999.

[53] R. Chang, S. Li, M. V. Lubarda, B. Livshitz, and V. Lomakina, " FastMag: Fast micromagnetic simulator for complex magnetic structures," Journal of Applied Physics, 109, 07D358 (2011)

[54] S. Fu, W. Cui, M. Hu, R. Chang, M. J. Donahue and V. Lomakin, "Finite-Difference micromagnetic solvers with the Object-Oriented Micromagnetic Framework on graphics processing units", IEEE Trans. on Magnetics, vol. 52, no. 4, pp. 1-9, April 2016, Art no. 7100109, doi: 10.1109/TMAG.2015.2503262.

[55] A. Vansteenkiste and Ben Van de Wiele. "MuMax: a new high-performance micromagnetic simulation tool." Journal of Magnetism and Magnetic Materials 323.21 (2011): 2585-2591.

[56] T. L. Gilbert, "The Phenomenological Theory of Damping in Ferromagnetic Materials," *IEEE Trans. MAG*, vol. 40, no, 6, pp. 3443-3449, Nov. 2004.

[57] Tokuda, Kathleen L., J. Stevenson Kenney, Michael Geiler, and Joseph H. Kim. "Characterization and Behavioral Modeling of a Frequency-Selective Limiter." 2019 IEEE Radio and Wireless Symposium (RWS) (2019): 1-4.

[58] S. N. Stitzer, "Spike leakage and suppression in frequency selective limiters," in IEEE MTT-S Int. Microw. Symp. Dig., vol. 2, Jun. 2000, pp. 901–904.

[59] A. J. Giarola, "A review of the theory characteristics and operation of frequency selective limiters," Proc. IEEE, vol. 67, no. 10, pp. 1380–1396, Oct. 1979.

[60] D. R. Jackson and R. W. Orth, "A frequency-selective limiter using nuclear magnetic resonance," Proc. IEEE, vol. 55, no. 1, pp. 36–45, Jan. 1967.

[61] Qin Yu, T. W. Holmes, and K. Naishadham, "RF equivalent circuit modeling of ferrite-core inductors and characterization of core materials," in IEEE Transactions on Electromagnetic Compatibility, vol. 44, no. 1, pp. 258-262, Feb. 2002.

[62] Mikhail Kozlov, Robert Turner, "Fast MRI coil analysis based on 3-D electromagnetic and RF circuit co-simulation," Journal of Magnetic Resonance, Volume 200, Issue 1, September 2009, Pages 147-152.

[63] P. J. Burke, "An RF circuit model for carbon nanotubes," in IEEE Transactions on Nanotechnology, vol. 2, no. 1, pp. 55-58, March 2003, doi: 10.1109/TNANO.2003.808503.

[64] Wheeler, Harold Alden. "The Spherical Coil as an Inductor, Shield, or Antenna." Proceedings of the IRE 46 (1958): 1595-1602.

[65] G. F. Engen and C. A. Hoer, "Thru-Reflect-Line: An Improved Technique for Calibrating the Dual Six-Port Automatic Network Analyzer," IEEE Trans. Microw. Theory Techn., vol. MTT-27, pp. 987–998, December 1979.

[66] B. Lax and K. J. Button, Microwave Ferrites and Ferrimagnetics. New York, NY, USA: McGraw-Hill, 1962.

[67] Ü. Özgür, Y. Alivov, and H. Morkoç, "Microwave ferrites, part 1: fundamental properties," *J Mater Sci: Mater Electron* 20, 789–834, 2009.

[68] D. Wei, Micromagnetics and Recording Materials, 2012 Springer Briefs in 21 Applied Sciences and Technology, DOI: 10.1007/978-3-642-28577-6_2.

[69] D. M. Pozar, *Microwave Engineering*, 3rd ed, Chapter 9, Hoboken, NJ, USA:Wiley, 2005.

[70] P. R. Emtage and S. N. Stitzer, "Interaction of signals in ferromagnetic microwave limiters," *IEEE Trans. Microw. Theory Techn.*, vol. MTT-25, no. 3, pp. 210–213, Mar. 1977.

[71] S. M. Gillette, M. Geiler, J. D. Adam, and A. L. Geiler, "Ferrite-based reflective-type frequency selective limiters," *Proc. IEEE MTT-S Int. Microw. Workshop Ser. Adv. Mater. Processes RF THz Appl. (IMWSAMP)*, Ann, Arbor, MI, USA, Jul. 2018, pp. 1–3.

[72] P. S. Carter, "Magnetically-Tunable Microwave Filters Using Single-Crystal Yttrium-Iron-Garnet Resonators," IRE Trans. Microw. Theory Techn. vol. 9, no. 3, pp. 252-260, May 1961.

[73] W. Gu, K. Luong, Z. Yao, H. Cui and Y. E. Wang, "Ferromagnetic resonance enhanced electrically small antennas," IEEE Trans. Antenn. Propagat. vol. 69, no. 12, pp. 8304-8314, Dec. 2021, doi: 10.1109/TAP.2021.3090032.

[74] D. D. Stancil, A. Prabhakar, *Spin Waves: Theory and Applications*. New York, NY, USA: Springer, 2009.

[75] L. J. Chu, "Physical limitations of omni-directional antennas," J. Appl. Phys., vol. 35, pp. 1479-1484, 1948.

[76] H. Cui, Z. Yao and Y. E. Wang, "Coupling Electromagnetic Waves to Spin Waves: A Physics-Based Nonlinear Circuit Model for Frequency-Selective Limiters," in IEEE Transactions on Microwave Theory and Techniques, vol. 67, no. 8, pp. 3221-3229, Aug. 2019, doi: 10.1109/TMTT.2019.2918517.

[77] W. H. Louisell, Coupled Mode and Parametric Electronics, Wiley, 1960.

[78] A. Scott, Active and Nonlinear Wave Propagation in Electronics, Wiley-Interscience, 1970.

[79] J. Brown, "Ferromagnetic limiters," *Microw. J.*, vol. 4, pp. 74–79, Nov. 1961.

[80] S. Stitzer, "Frequency selective microwave power limiting in thin YIG films," *IEEE Trans. Magn.*, vol. MAG-19, no. 5, pp. 1874–1876, Sep. 1983.

[81] J. D. Adam and S. N. Stitzer, "Frequency selective limiters for high dynamic range microwave receivers," *IEEE Trans. Microw. Theory Techn.*, vol. 41, no. 12, pp. 2227–2231, Dec. 1993.

[82] S. -S. Yang, T. -Y. Kim, D. -K. Kong, S. -S. Kim and K. -W. Yeom, "A Novel Analysis of a *Ku*-Band Planar p-i-n Diode Limiter," *IEEE Trans. Microw. Theory Techn.*, vol. 57, no. 6, pp. 1447-1460, Jun. 2009.

[83] F. R. Morgenthaler, "Survey of ferromagnetic resonance in small ferrimagnetic ellipsoids," *J. Appl. Phys.*, vol. 31, no. 5, p. S95, 1960.

[84] R. W. Orth, "Frequency-selective limiters and their application," *IEEE Trans. Electromagn. Compat.*, vol. EMC-10, no. 2, pp. 273–283, Jun. 1968.

[85] M. Cheng and C. E. Patton, "Spin wave instability processes in ferrites," in *Nonlinear Phenomena and Chaos in Magnetic Materials*, P. E.Wigen, Ed. Singapore: World Scientific, 1992.

[86] H. Suhl, "The nonlinear behavior of ferrites at high microwave signal levels," *Proc. IRE*, vol. 44, no. 10, pp. 1270–1284, Oct. 1956.

[87] E. Schl Mann, J. J. Green, and U. Milano, "Recent developments in ferromagnetic resonance at high power levels," *J. Appl. Phys.*, vol. 31, no. 5, p. S386, 1960.

[88] Simons, Rainee N, *Coplanar Waveguide Circuits, Components, and Systems*, John Wiley & Sons, 2004.

[89] Lei Lu, Young-Yeal Song, Joshua Bevivino, and Mingzhong Wu, "Planar millimeter wave band-stop filters based on the excitation of confined magnetostatic waves in barium hexagonal ferrite thin film strips," *Appl. Phys. Lett.* 98, 212502, 2011.

[90] Object Oriented Micromagnetic Framework (OOMMF). Accessed: May 5, 2019. [Online]. Available: https://math.nist.gov/oommf/

[91] R. Chang, S. Li, M. V. Lubarda, B. Livshitz, and V. Lomakina, " FastMag: Fast micromagnetic simulator for complex magnetic structures", Journal of Applied Physics, 109, 07D358 (2011)

[92] Tokuda, Kathleen L., J. Stevenson Kenney, Michael Geiler and Joseph H. Kim. "Characterization and Behavioral Modeling of a Frequency-Selective Limiter." 2019 IEEE Radio and Wireless Symposium (RWS) (2019): 1-4.

[93] Q. Gao, M. E. Fordham, H. Cui, and Y. E. Wang, "A Compact Circuit Model for Frequency-Selective Limiters With Strong Field Nonuniformity," in IEEE Transactions on Microwave Theory and Techniques, vol. 71, no. 12, pp. 5124-5134, Dec. 2023.

[94] S. N. Stitzer, "Injection Locked Oscillator Theory for Frequency Selective Limiters," 2019 *IEEE MTT-S Int. Microw. Symp. (IMS)*, Boston, MA, USA, 2019, pp. 665-668.

[95] D. J. Seymour, D. D. Heston, and R. E. Lehmann, "X-band and Ka-band monolithic GaAs PIN diode variable attenuation limiters," in IEEE Microw. Millim.-Wave Monolithic Circuits Symp. Dig. Papers, May 1988, pp. 147–150.

[96] D. G. Smith, D. D. Heston, and D. L. Allen, "Designing high-power limiter circuits with GaAs PIN diodes," in IEEE MTT-S Int. Microw. Symp. Dig., vol. 1, Jun. 1999, pp. 329–332.

[97] P. Phudpong and I. C. Hunter, "Nonlinear bandstop filters: A new method of frequency selective limiting," in Proc. Eur. Microw. Conf., Sep. 2006, pp. 204–207.

[98] D. Shojaei-Asanjan, S. Attar, and R. R. Mansour, "Tunable RF MEMS-based frequency-dependent power limiter," in Proc. IEEE MTT-S Int. Microw. Symp. (IMS), San Francisco, CA, USA, May 2016, pp. 1–3.

[99] L. Zheng, M. Lops and X. Wang, "Adaptive Interference Removal for Uncoordinated Radar/Communication Coexistence," in IEEE Journal of Selected Topics in Signal Processing, vol. 12, no. 1, pp. 45-60, Feb. 2018.

[100] D. Shojaei-Asanjan, M. Bakri-Kassem and R. R. Mansour, "Analysis of Thermally Actuated RF-MEMS Switches for Power Limiter Applications," in Journal of Microelectromechanical Systems, vol. 28, no. 1, pp. 107-113, Feb. 2019.

[101] P. S. Carter, "Magnetically-Tunable Microwave Filters Using Single-Crystal Yttrium-Iron-Garnet Resonators," IRE Trans. Microw. Theory Techn. vol. 9, no. 3, pp. 252-260, May 1961.

[102] J. Uher and W. J. R. Hoefer, "Tunable microwave and millimeter-wave band-pass filters," IEEE Trans. Microw. Theory Techn., vol. 39, no. 4, pp. 643-653, April 1991.

[103] Ken-Ya Hashimoto, RF Bulk Acoustic Wave Filters for Communications, Artech, 2009.

[104] R. M. Hays and C. S. Hartmann, "Surface-acoustic-wave devices for communications," in Proceedings of the IEEE, vol. 64, no. 5, pp. 652-671, May 1976.

[105] https://aciatlanta.com/

[106] Qian Gao, Lap Yeung, Yuanxun Ethan Wang, "Miniaturized Millimeter Wave Resonators with Self-Biased BaM Films," IEEE International Symposium on Antennas and Propagation and USNC-URSI Radio Science Meeting (AP-S/URSI), July 23–28, 2023, Portland, Oregon, USA.